INSTITUTE
FOR
AEROSPACE STUDIES

UNIVERSITY OF TORONTO

LATERAL DISPERSION OF A HIGH-ENERGY ION BEAM IN A SCATTERING MEDIUM

by

T. W. Crouch and J. J. Gottlieb

17 JUNI 1984

TECHNISCHE HOGESCHOOL DELFT
LUCHTVAART- EN RUIMTEVAARTTECHNIEK
BIBLIOTHEEK
Kluyverweg 1 - DELFT

April 1984

UTIAS Report No. 278
CN ISSN 0082-5255

LATERAL DISPERSION OF A HIGH-ENERGY ION BEAM IN A SCATTERING MEDIUM

by

T. W. Crouch and J. J. Gottlieb

Submitted October 1983

April 1984

UTIAS Report No. 278
CN ISSN 0082-5255

Acknowledgements

We would like to express our utmost thanks to Dr. P. C. Stangeby, Dr. A. A. Haasz and Dr. J. H. de Leeuw for first introducing us to the interesting world of gas target neutron generators. The basic concept for the present study evolved from an earlier Monte Carlo investigation by the second author of the ion-beam spreading in the free jet of a gas target neutron generator. Their interest in the present study is much appreciated.

The stimulation and encouragement received from Professor I. I. Glass are acknowledged with special thanks.

The first author is deeply indebted to the Natural Sciences and Engineering Research Council of Canada for the NSERC Graduate Scholarship, given for the duration of his M.A.Sc. program at UTIAS, without which this study could not have been completed.

Financial support in the form of an operating grant for the second author from the Natural Sciences and Engineering Research Council of Canada for the extensive computer calculations is gratefully acknowledged.

Abstract

The problem of the lateral dispersion of a beam of high-energy ions by molecular collisions as it passes through a variable density medium is solved by using both a Monte Carlo simulation and a new approximate analytical method. Numerous Monte Carlo computer runs are completed for high-energy ions (protons) moving in a varying density gas (molecular hydrogen). These runs include aphysical cases for which the energy of the ion is unattenuated with distance and physical cases for which the ion energy is decreased in accordance with experimental measurements of its range. Such numerical results show clearly that the beam-dispersion profiles at increasing ion-beam penetration depths are essentially self similar and that the profiles from different cases were also essentially similar. Based on the idea of similarity, an approximate analytical method is developed for quick and easy scaling of the beam-dispersion profiles within each case and from one case to another, in order to dispense with the time consuming and costly Monte Carlo simulations. This method for predicting the change in the probability distribution (root-mean-square value) of the dispersed-beam profile is successful, and the Monte Carlo results are reproduced well. It should be noted that this work is done mainly for a unidirectional point source of monoenergetic ions in the absence of any external magnetic and electric fields. However, the analysis to extend the results from a point source to a finite-sized beam of variable intensity, cross-sectional area, and ion energy is presented and some results are given.

Table of Contents

Table of Contents (continued)

Notation

a_0	first Bohr radius of an electron ($a_0 = \hbar^2/m_0e^2 = 5.29177\times10^{-11}$ m)
a_i	i^{th} coefficient of the curve fit to the measured stopping power data
$A_0(x,z)$	initial ion-beam cross-sectional area
D	diameter of a free-jet orifice
e	elementary unit of charge (4.8029×10^{-10} e.s.u.)
E	collision energy in the center-of-mass reference frame
E{ }	expected value of the variable in the brackets
E_0	reference energy equal to the ionization potential of hydrogen ($E_0 = e^2/2a_0 = m_0e^4/2\hbar^2 = 2.1785\times10^{-11}$ erg = 13.58 eV)
$E_0(x,z)$	initial ion-energy distribution across the beam
E_{in}	abbreviation for the symbol $E_{p_{in}}$
E_p	energy of a proton in the laboratory frame of reference
$E_{p_{in}}$	initial energy of a proton in the laboratory frame of reference
E_x	mass-weighted dimensionless ion energy in the center-of-mass frame of reference (mE/m_0E_0)
ΔE_p	difference in proton energy between two collisions ($E_{p_i} - E_{p_{i+1}}$)
f(y)	dimensionless number density profile of scattering medium [$N = N_0f(y)$]
F(z)	function in P(R) in appendix B
$\hbar$	rationalized Planck's constant ($\hbar = h/2\pi = 1.05459\times10^{-27}$ erg-s)
$H(\chi)$	function in the free-jet profile given by Eq. 2.39
I(R)	ion current due to a point source
I(x,y,z)	ion-beam intensity
$I(\theta,\phi)$	differential scattering cross section
I_0	initial constant ion-beam intensity
$I_0(x,y)$	initial ion-beam intensity distribution across the beam
ITOTP	total number of ion paths followed by the Monte Carlo simulation
k	constant factor for the energy loss used in Eq. 2.6

Notation (continued)

k	magnitude of the incident wave vector ($mv/\hbar$)
k_i	magnitude of the incident wave vector ($mv/\hbar$)
k_d	magnitude of the scattered wave vector
K	magnitude of the scattering wave vector [$2(mv/\hbar)\sin(\theta/2)$]
m	reduced mass of two particles in a collision [$m_1 m_2/(m_1+m_2)$]
m_0	rest mass of an electron (9.106×10^{-27} g)
m_1	mass of the incident particle in a collison
m_2	mass of the targer particle in a collision
m_p	mass of a proton (1.762×10^{-24} g)
M	number of ions per unit time passing within a radius R of the beam axis
$\bar{M}$	total number of ions per unit time emitted by a point source
min(i,j)	symbolic notation for using the minimum value of the pair (i,j)
n	ion-beam number density
n	number of collisions, n^{th} collision
$\bar{n}$	unit direction vector
n_0	initial ion-beam number density
N	number density of the scattering medium
N_0	initial number density of the scattering medium
N_{inf}	scattering medium number density at infinity for the free jet
N_{orf}	scattering medium number density at the orifice of a free jet
$p(y)$	probability density distribution
$P(y)$	cumulative probability distribution
$P(R,y,E)$	cumulative probability distribution
Q	total collision cross section
r	radial separation distance between two colliding particles
r	a random number in the range of 0 to 1 (uniform)

r_i	i^{th} random number in the range of 0 to 1 (uniform distribution)
R	radial distance measured perpendicular to the ion-beam axis
R_0	initial radius of a cylindrical ion beam
R*	R value for which P(R) = 0.5
R'	lateral separation distance measured from the point-source axis to a certain position of interest for calculating the current
R_{max}	maximum value of R
R_{min}	minimum value of R
s	path length along a particle trajectory
u	direction cosine in the x Cartesian direction
v	direction cosine in the y Cartesian direction
v	speed of an ion in the center-of-mass reference frame
V(r)	interaction potential between two colliding particles
w	direction cosine in the z Cartesian direction
w	multiple scattering deflection angle
$\bar{w}$	root-mean-square multiple-scattering deflection angle
x	Cartesian direction
x	reduced variable equal to $E_x \sin^2(\theta/2)$
x_i	x position of the ion after its i^{th} collision
X	x Cartesian coordinate in the target plane
y	Cartesian direction
y	dummy integration variable
y_1	y position at which the ion is presently located in the scattering medium
y_i	y position of the ion after its i^{th} collision
y_{max}	maximum range of an ion or proton in a scattering medium
Y	y Cartesian coordinate in the target plane

1.0 INTRODUCTION

1.1 Motivation for the Present Study

In todays growing need for energy, society is beginning to depend more and more on atomic energy. Fission energy has fallen into disfavour with most of the population, because of the possibility (although remote) of the release of radioactive by-products in the event of an accident and the hazards associated with moving and storing radioactive waste. The alternative - fusion energy - has not yet reached the engineering stage where it is feasible and marketable. However, research and engineering are progressing rapidly, and the promise of success seems certain in the next few decades.

In the ongoing research into fusion reactors the search for a suitable reactor wall material is an important part of making fusion power economically feasible. If the wall material will not withstand the continued impact of a tremendous number of high-energy neutrons, alpha and other particles created within the reactor it will not be feasible to employ it as a wall material, because it would have to be replaced often. This would thus increase greatly both the down time and operational cost of the reactor.

Various devices have been proposed and even developed to test suitable wall materials to sustain high-energy particle impact, in order to obtain information regarding their flux and fluence endurance to such particles. A number of studies of proposed devices for 14-MeV-neutron testing of materials that prompted the present study involve subsonic, transonic and hypersonic gas target neutron generators [1-6]. For example, consider the subsonic gas target neutron generator sketched in Fig. 1. A triton beam is directed through the free-jet expansion into the nozzle flow of molecular deuterium from the large reservoir. The triton beam loses most of its energy in the dense, subsonic, nozzle flow and stops therein. A small percentage of the collisions between the tritons and deuterium molecules results in fusion, with the release of 14-MeV neutrons. Some of these neutrons then collide with the material to be tested, which lines the inside periphery of the nozzle.

Not illustrated in Fig. 1 is that the triton beam does not remain fixed in diameter but in fact spreads laterally from numerous small angle collisions with deuterium molecules as it traverses the deuterium free jet and enters the nozzle flow [3]. The nozzle diameter must be large enough to accommodate the entire triton beam, otherwise high-energy tritons will strike both the nozzle walls and materials sample, thereby causing undesirable damage. A knowledge of the extent of the beam spreading is important to the design of such a device, therefore, because the nozzle diameter must be sufficiently large to surround the entire beam, and yet it must be as small as possible mainly to reduce the deuterium circulation pumping requirements and partly to maximize the flux of neutrons striking the materials sample.

Although the present study stems from the need to predict the lateral spreading of a triton beam in a molecular deuterium flow occurring in a gas target neutron generator, it is presented in this report for the more general case of the lateral spreading of a beam of high-energy ions as a function of the initial ion beam energy, the density variation of the scattering medium, and the distance travelled by the beam through the scattering medium. A more detailed description of the problem is given in the next section. In this

manner the present investigation has a wider application to other and more general problems of ion beams passing through gases [7] and solids [8].

1.2 Description of the Problem

Consider an ion beam of initial cross section $A_0(x,z)$, intensity $I_0(x,z)$, and ion energy $E_0(x,z)$ travelling through a stationary or flowing gas with a density field $\rho(y)$ (see Fig. 2), in which it spreads laterally due to molecular collisions with the scattering medium. The beam dispersion studied in this work will be due to the Coulomb interactions between the high-energy ions of the beam and the atoms or molecules of the intervening gas. A solution will be presented for the ion beam intensity $I(x,y,z)$, that is, as a function of the coordinates x, y and z. For this study it will be assumed that there are no externally applied magnetic or electric fields. Furthermore, the effects of beam heating on generating a gas flow in an initially stagnant scattering medium or altering the already existing flow field of the scattering medium are ignored.

1.3 Previous Work

The random walk of a high-energy particle within a scattering medium can be simulated fairly easily through the use of a Monte Carlo computer program, provided that the collision probability statistics are known and readily available. An excellent review of the subject of Monte Carlo calculations of this kind can be found in a paper by Berger [9]. However, the present problem has not been studied before. Similar problems have been considered that make use of the same collision theory presented in this study; however, they are concerned principally with the calculation of reflection and transmission coefficients, the angular distribution of particles emerging from thick foils, absorption of particles by foils, path length straggling, mean ionization potentials, and the backscattering of ions from solids (e.g., see Refs. 8 and 9). None have dealt directly with the prediction of the lateral spreading of an ion beam within a varying density scattering medium. However, it should be noted that most of the problems mentioned above could also be solved by using the type of analysis presented in this report.

1.4 Present Study

In the present study the dispersion of an ion beam is simulated by means of a Monte Carlo computer code that includes all of the necessary collision theory statistics. In this simulation the range-energy equation is used in conjunction with the continuous-slow-down approximation to include the energy attenuation of the ions. The spatial variations of gas density under consideration here include linear and exponential distributions, as well as free-jet expansion profiles. From the individual ion paths generated numerically by the Monte Carlo method, the intensity distributions can be obtained at different distances from the beam origin, which illustrates the degree of beam spreading with distance. All of this work and the graphical results are presented in Chapter 2.

It is anticipated that the Monte Carlo solution will be a time consuming and expensive process, because thousands of ion paths have to be followed through thousands of collisions to obtain statistically meaningful results. In

order to reduce the costs, an analytical approximation for scaling the lateral spreading of the ion beam within each case and from one case to another is developed, which is quick and easy to implement. This new technique and the evaluation of its success in reproducing and replacing Monte Carlo results are given in chapter 3. The beam configuration considered in chapters 2 and 3 is a unidirectional point source of initially monoenergetic ions. All problems can be solved initially for such a point source, because the results for this case can be easily extended analytically to that of a finite beam of initial cross section $A_0(x,z)$, intensity $I_0(x,z)$, and ion energy distribution $E_0(x,z)$. The analysis for this extension is presented in chapter 4. The concluding remarks follow in chapter 5.

2.0 MONTE CARLO SIMULATION OF ION BEAM SPREADING IN A SCATTERING MEDIUM

2.1 Introduction

Monte Carlo techniques comprise that extension of experimental mathematics that is concerned with experiments on random numbers. Previous applications of Monte Carlo simulations have been mainly in the fields of nuclear physics and operational research, although problems in other fields of science including biology, chemistry, and medicine have been solved successfully by this method. Typically, Monte Carlo methods are used in solving problems where the available theoretical mathematics is insufficient to yield an analytical solution. For a thorough discussion of the principles involved in the Monte Carlo method the reader is referred to the books by Hammersley & Handscomb [10] and Cashwell & Everett [11].

The fundamental principle involved in Monte Carlo simulations can be stated in the following way [10]. If $p(y)dy$ is the probability of y lying between y and $y + dy$ in the interval $a \leq y < b$, where a and b are constants, and

$$\int_a^b p(y)\, dy = 1 , \tag{2.1}$$

then

$$r = P(y) = \int_a^x p(y)\, dy \tag{2.2}$$

determines y uniquely as a function of r or P(y). Moreover, if r is uniformly distributed on the interval $0 \leq r < 1$, then y falls with frequency $p(y)dy$ in the interval $(y, y + dy)$. Hence, in Monte Carlo simulations the probability density function p(y) must be known a priori. Then, by picking a random number r from a uniform distribution in the range of 0 to 1, a value of y can be determined from Eq. 2.2 for the process involved. The correct randomness of the physical process can therefore be obtained. Note that the integral of the probability density function, denoted as P(r), is called the cumulative probability function.

If Eq. 2.2 can be inverted to obtain an explicit expression for y as a function of r, a notable benefit in simplicity is achieved. Otherwise, the integral equation has to be solved numerically for the value of y, or by other more appropriate means (see Refs. 10 and 11).

The random walk of an ion through a scattering medium includes thousands of individual collisions for which the deflection angles and the free path length between collisions must be obtained. The deflection angle and free path length conventions used in this study are illustrated in Fig. 3. Thus, in order to apply the Monte Carlo method to solve for the paths of ions moving through a scattering medium, the probability density functions should be known a priori for

a) the free path length λ of the ion between collisions,

b) the scattering angle Θ in the laboratory frame of reference,

c) the azimuthal angle ϕ in the laboratory frame of reference, and

d) the energy change of the ion due to the collision.

For each known p(y), a value of r can be chosen at random from a uniform distribution of random numbers in the range of 0 to 1, and the value of the free path length, scattering angle, and so on can be obtained, such that the correct randomness of the physical process is simulated.

2.2 Free Path Length

For a beam of particles of number density n scattering in a medium of number density N, whose individual scatterers have a cross-sectional area Q, the attenuation law for unscattered particles is [appendix A and Ref. 11]

$$-dn/n = QN\, dy. \tag{2.3}$$

The derivation of the probability density function p(y) for the free path length from this attenuation law, and the subsequent inversion of the cumulative probability function P(y) given by Eq. 2.2 to yield the free path length as a function of the random number r, are developed and discussed in appendix A. The result for a density variation in the general form

$$N = N_0 f(y) \tag{2.4}$$

is (Eq. 8 of appendix A)

$$\int_{y_1}^{y_1 + \lambda} f(y)\, dy = -\frac{1}{N_0 Q}\, \ln(r_1), \tag{2.5}$$

where r_1 is a random number in the range of 0 to 1, y_1 is the position of the particle within the scattering medium (the origin being at the source), and λ is the free path length. When $N = N_0 f(y)$ is specified, that is, once the gas density profile f(y) is known, then Eq. 2.5 can be inverted to yield λ as an explicit function of r_1. A few particular examples of different density distributions and the resulting free path lengths (after inversion) are given in appendix A.

For interest it is worth mentioning that the path length can be specified by alternate methods. Although these methods are not employed in this report because they are not as appropriate, some of the more common ones are noted briefly here. For a more thorough examination of these alternate methods the

reader is referred to a paper by Berger [9].

a) Logarithmic spacing. In this method the path length is chosen such that, on the average, the energy of the particle is decreased by a constant factor k per step. That is, the energy of the particle after the collision is obtained from the energy of the particle before the collision by multiplying by a constant factor k and subtracting. This is written as

$$1 - \frac{1}{E_{p_i}} \int_{s_i}^{s_{i+1}} \left| \frac{dE_p}{ds} \right| ds = k , \qquad (2.6)$$

where dE_p/ds must be obtained from either theory or experiment. Then, from Eq. 2.6 the path length $s_{i+1} - s_i$ can be determined. This has the advantage that, if $k = 1/2^m$, the particle has then lost one half of its energy after m steps. This also has the advantage that the distribution of angular deflections changes very slowly from step to step [9]. This method is generally used when condensed case histories are being employed, and it can be used in two different ways. The variable that is used as the time clock for "taking the picture" can be either the energy of the particle or the path length.

b) Mixed logarithmic spacing. This procedure employs the same method as that used in a, except that, if the particle is about to cross a boundary of interest, the step is broken into even smaller steps so that the uncertainty of both the crossing point and the energy of the particle is reduced.

c) Uniform spacing. In this method the step size $s_{i+1} - s_i$ is constant.

d) Consideration of path length fluctuations. As pointed out and discussed by Berger, the path length fluctuations are specified by a Gaussian distribution.

Methods a to c introduce a predictable step size into the so-called random walk of the particle. If the walk is to be truly random, then the step size must vary statistically about an average value that is predictable from the physics of the collision. However, the Gaussian distributed fluctuations of method d do not correctly represent the physical process, as one can see from Eq. 2.5. Further, all of these methods are used when condensed case histories are involved, that is, each step includes many collisions and thus are of no use in this study.

2.3 Angular Deflection

The interaction potential V(r) between an ion and a molecule or atom is needed in order to calculate the probability density functions for both the azimuthal and scattering angles. For the specific case of a proton colliding with a hydrogen atom [12]

$$V(r) = e^2 \left[\frac{1}{a_0} + \frac{1}{r} \right] \exp(-2r/a_0) , \qquad (2.7)$$

where e is the fundamental unit of charge, a_0 is the first Bohr radius, and r is the distance separating the two charges.

For a central potential the azimuthal angle ϕ will be uniformly distri-

buted between $-\pi$ and $+\pi$, that is, the scattering is isotropic with respect to the azimuthal angle and p(y) is the constant $1/2\pi$. Therefore, in order to obtain an azimuthal angle for each collision, the equation

$$\phi = \pi(1 - 2r_2) \tag{2.8}$$

can be used, where r_2 is a random number between 0 and 1.

To find an expression for the scattering angle Θ in the laboratory reference frame, one must first consider the differential scattering cross section $I(\theta)$, where θ is the scattering angle in the center-of-mass reference frame. The differential scattering cross section is defined as the number of particles scattered into the solid angle $d\omega = \sin(\theta)d\theta d\phi$ divided by the total number of particles of the incident beam. This is the unnormalized probability density function for the angle θ. The Born approximation of $I(\theta)$ for the potential given by Eq. 2.7 is determined in appendix B. $I(\theta)$ is then used to yield θ as a function of the random number r_3. The final result is quoted here; however, the reader is referred to appendix B for more details. The scattering angle in the center-of-mass frame is

$$\theta = 2\,\text{Arcsin}\left[\frac{1}{E_x C}\left(\frac{1 - C^2/4}{\sqrt{1 - r_3(1 - C^4/16)} - C^2/4} - 1\right)\right]^{\frac{1}{2}}, \tag{2.9}$$

where

$$C = (7 - \sqrt{13})/3 \tag{2.10}$$

and

$$E_x = mE/m_0 E_0 . \tag{2.11}$$

Here, m is the reduced mass of the ion and the scattering particle, m_0 is the mass of an electron, E_0 is a reference energy equal to $e^2/2a_0 = m_0 e^4/2\hbar^2$ or the ionization potential of hydrogen (13.58 eV), and E is the collion energy in the center-of-mass coordingate frame.

If the collision is assumed to be elastic, the scattering angle Θ in the laboratory frame is given by

$$\tan(\Theta) = \frac{\sin(\theta)}{\cos(\theta) + m_1/m_2}, \tag{2.12}$$

where m_1 is the mass of the incident particle and m_2 is the mass of the target. This, of course, is not true in general, but for collisions considered in this study the premise of elastic collisions is valid (see appendix B).

The angles Θ and ϕ determine the deflection of the ion from its precollision line-of-flight direction. This deflection must be added to the line-of-flight direction to obtain the resultant post collision direction in the Cartesian coordinate system (see Fig. 3). Let $\bar{n}_{i-1} = [u_{i-1}, v_{i-1}, w_{i-1}]$ be the direction cosines of the line-of-flight direction of the particle after it has experienced i-1 collisions. If Θ_i and ϕ_i are the deflection angles experienced by the particle during the ith collision, then the resultant direction cosines are given at the top of the next page as [11]

$$u_i = (\sin(\Theta_i)\cos(\phi_i)u_{i-1}w_{i-1} - \sin(\Theta_i)\sin(\phi_i)v_{i-1})/\sqrt{1-w_{i-1}^2} + \cos(\Theta_i)u_{i-1},$$

$$v_i = (\sin(\Theta_i)\cos(\phi_i)v_{i-1}w_{i-1} + \sin(\Theta_i)\sin(\phi_i)u_{i-1})/\sqrt{1-w_{i-1}^2} + \cos(\Theta_i)v_{i-1},$$

$$w_i = -\sin(\Theta_i)\cos(\phi_i)\sqrt{1-w_{i-1}^2} + \cos(\Theta_i)w_{i-1}. \qquad (2.13)$$

Therefore, once the random angles ϕ_i and Θ_i are obtained from Eqs. 2.8 and 2.9, respectively, Eqs. 2.13 then yield the direction cosines of the scattered ion. Note that Eqs. 2.13 become unstable when $|w|$ is close to unity; therefore, it will be assumed that the ions will emerge from the source and travel in the y or $\bar{n}_0 = [0, 1, 0]$ direction. This will avoid encountering the instability in these equations because the scattering angle Θ is so small that $|w| << 1$ at all times.

It is worth mentioning for interest that the deflection angles can be specified by alternate methods. Although these methods are not used in this report because condensed case histories are not employed, some of the most common ones are noted briefly here. For a more thorough discussion of these techniques the reader is referred to a paper by Berger [9].

a) Gaussian distribution. If the net angular multiple-scattering deflection is the result of many small angle scattering events, each of the same order of magnitude, then purely statistical considerations lead to a Gaussian distribution given by

$$p(w)\ w\ dw = 2(w/\bar{w})^2 \exp(-w^2/\bar{w}^2)\ dw, \qquad (2.14)$$

where w is the multiple scattering deflection angle. The root-mean-square deflection angle $\bar{w}$ is calculated from the appropriate single scattering cross section. This approximation does not include the large individual deflections that statistically occur; therefore, it does not represent the actual fluctuation in the individual scattering events in this study. Large angles, although infrequent, contribute markedly to the lateral dispersion of the beam. This method can only be used when condensed case histories are employed, and it is not very accurate. The following two theories would be normally used instead because they are more accurate.

b) Distribution of Moliere [13]. Moliere's theory takes into account the effect of occasional large angle scattering events, which are neglected in the Gaussian approximation. From this theory the multiple scattering cross section is known as an infinite series involving a reduced angle variable. Because this theory involves an infinite series with a tabulation of statistical functions, it is not in a convenient analytical package for use by a computer. Large tables would have to be stored in the program or in a readable data file and, although this can be done, it is a cumbersome and an expensive process.

c) Theory of Goudsmit and Saunderson [14, 15]. These authors derived the angular distribution of multiple scattering deflections as a Legendre series, by assuming a continuous-slowing-down approximation that will be discussed in section 2.4. This theory includes all possible angular deflections, and it can be used with any single scattering cross section. Therefore, this theory is superior to that of Moliere, but it still involves an infinite series and is thus cumbersome to incorporate in a computer program.

All of the theories in a, b, and c are for condensed case histories, un-

fortunately, and they, therefore, cannot be used in this study. However, they can be used to test some of the results of the present Monte Carlo simulation. This test will be done for the Gaussian approximation only, because it permits an easy check.

2.4 Energy Loss

The energy loss of the ion as it travels through the scattering medium is determined by [9]

$$\Delta E_{p_i} = E_{p_i} - E_{p_{i+1}} = \int_{s_i}^{s_{i+1}} \left| \frac{dE_p}{ds} \right| ds , \qquad (2.15)$$

where s is the actual path length travelled by the ion. Because the ion does not deviate substantially from its incident direction along the y-axis, the path length s can be approximated by its projection onto the y-axis. Therefore, Eq. 2.15 becomes

$$\Delta E_{pi} = E_{pi} - E_{pi+1} = \int_{y_i}^{y_{i+1}} \left| \frac{dE_p}{dy} \right| dy . \qquad (2.16)$$

It now remains to find an expression for the ion energy as a function of the distance y. The stopping power of a material with respect to an incident particle is defined as

$$\varepsilon = -\frac{1}{N} \frac{dE_p}{dy} \qquad (2.17)$$

and has been experimentally measured for many materials [16].

The stopping power of a hydrogen gas for protons has been measured by Whaling [16], and his results are shown in figure 4. A curve of the form

$$\frac{1}{\varepsilon} = \frac{a_0}{\sqrt{E_p}} + a_1 + a_2\sqrt{E_p} + a_3 E_p \qquad (2.18)$$

was fitted to that data. It was found for the two regions 0.0 to 0.04 MeV and 0.04 to 10.0 MeV that the curve fit is within 3 percent of Whaling's data. Values of the coefficients for Eq. 2.17 are given in the following table for the respective regions.

Coefficients	$0.0 \leq E < 0.04$ MeV	$0.04 \leq E \leq 10.0$ MeV
a_0	0.00294787	0.0512652
a_1	0.359963	-0.246743
a_2	-1.84853	0.690572
a_3	3.93144	0.389733

Note that in Eq. 2.18 the energy of the proton must be in units of MeV.

As a further check on the accuracy of this curve fit, Eq. 2.18 can be integrated to obtain an expression for the range of a proton in molecular hydrogen, that is,

$$N\,dy = -\frac{1}{\varepsilon}\,dE_p . \tag{2.19}$$

Recall that $N = N_0 f(y)$ in general; therefore,

$$N_0 \int_0^{y_{max}} f(y)\,dy = -\int_{E_{pin}}^{0} \frac{1}{\varepsilon}\,dE_p , \tag{2.20}$$

where $E_{p_{in}}$ is the initial energy of the proton and y_{max} is the range of the proton. For a constant density Eq. 2.20 becomes

$$y_{max} = \frac{1}{N_0}\left[2a_0\sqrt{E_{pin}} + a_1 E_{pin} + \frac{2}{3}a_2 E_{pin}^{1.5} + \frac{1}{2}a_3 E_{pin}^2 - 0.058 \right] , \tag{2.21}$$

where the appropriate coefficients must be used. This equation was compared to the experimental equation for the range of protons in molecular hydrogen found by Whaling. The predicted values of the present curve fit and the curve fit presented by Whaling are shown in table 1, and the agreement is very good.

To obtain the energy loss for a particular collision for the Monte Carlo simulation, Eq. 2.17 is inverted to yield

$$dE = -N\varepsilon\,dy . \tag{2.22}$$

In using this formula the energy of the proton in MeV before the collision is used in Eq. 2.18 to calculate ε. This value is then used in Eq. 2.22 to obtain the desired energy loss during that collision. Note that the energy loss for a particular collision includes, in an average way, that from bremsstrahlung, ionization, electrical excitation losses, and so on. Therefore, the assumption made in section 2.3 that the collisions are elastic, affects only the calculation of the scattering angle and not the energy loss or the path length. This means that any discrepency between the Monte Carlo results and any experimental results that may be obtained would be, in part, due to the assumption in this study that the collisions are elastic in the calculation of the scattering angle.

It should be pointed out that insufficient data on energy-loss cross sections does not permit the determination of the probability density distribution for the energy loss of the ion to be used in this study. Instead the continuous-slowing-down approximation is used, even though a complete solution of the problem would require a random fluctuation of the energy.

For interest it is worth mentioning that the energy loss can be specified by alternate methods. Although these methods are not used in this report because they are not as appropriate, some of the most common ones are noted briefly here. For a more thorough dicussion of these methods the reader is referred to a paper by Berger [9].

a) Fluctuations of ionization and bremsstrahlung loss. To take into account these losses, the ionization and bremsstralung collisional cross sections must be known. The analysis for these cross sections is complicated and some have been derived for a wide variety of approximations. The use of complicated and approximate cross sections has been avoided in this study by using the range-energy relationship presented earlier in this section, which takes these fluctuations into account on an average basis through the use of experimental data.

b) Logarithmic spacing. For this case E_{i+1} equals kE_i as described previously for the case of the free path length.

c) Uniform spacing. In this method $E_i - E_{i+1}$ equals a constant.

Berger also describes a scheme that mixes these procedures, that is, the collisions are grouped together but are separated by a single "catastrophic" collision in which the particle loses a large fraction of its energy. By this means the particle's history is divided into sections, in which the continuous-slowing-down approximation is used, and each section then terminates in a catastrophic collision.

2.5 Monte Carlo Computer Program

All of the analysis required for the simulation of the spreading of an ion beam in a varying density scattering medium by a Monte Carlo technique has now been presented. This analysis was incorporated into a FORTRAN computer program that considers a unidirectional point source of protons travelling through a varying density molecular hydrogen gas. The computer-program listing for this Monte Carlo simulation is given in appendix C. In this computer program the point-source configuration is always used. This is all that is required for the simulation of any finite beam configuration, because by varying the point-source intensity, position, and ion energy the results for a finite beam can be obtained through an integration of the numerical results generated by the Monte Carlo simulation (see chapter 4). Hence, all Monte Carlo results will be presented initially in chapters 2 and 3 for a point source.

In the Monte Carlo simulation, numerous ions (ITOTP) are followed out to a distance somewhat shorter than the total range of the ion. As the ion path crosses several planes perpendicular to its initial direction (i.e., target planes) at specified distances from the source, the coordinate position [x,z] of the crossing point can be recorded. When the Monte Carlo simulation is complete, these crossing point values could then be used to calculate the intensity I(x,z) of the beam at each particular plane. This could be accomplished by dividing the plane into small squares and counting the number of particles that cross each square. The resulting spatial distribution of the intensity would be a surface as depicted in Fig. 5. It would be peaked at the center ($x = 0$, $y = 0$), where most of the ions would cross, and drop off symmetrically from the center. Further, the distribution would remain symmetric as the penetration depth increases, experiencing only a flattening out as depicted in Fig. 6. The intensity remains axially symmetric because of the isotropic nature of the azimuthal angle and the uniformity in the scattering medium in the lateral directions. Note that the construction of such an intensity distribution from Monte Carlo generated data would require a tremendous number of ion paths to ensure smoothness.

By considering the intensity distribution as a function of R (instead of x and y), the distrbution can be constructed with markedly fewer ion paths. This is possible, of course, because the intensity is axially symmetric. The intensity distribution I(R) is shown in Fig. 7a. Note that this distribution could be constructed from the Monte Carlo data by counting paths crossing each target plane between concentric circles surrounding the beam axis and dividing by their mean radius.

The probability density function p(R) can be obtained directly from the intensity I(R), by multiplying the path count in concentric circles by the mean radius. The resulting curve for the probability density is shown in Fig. 7b. Furthermore, the cumulative probability distribution P(R) follows directly from p(R), and it is shown in Fig. 7c. Note that the interrelationships among I(R), p(R), and P(R) are given in equation form as insets in Figs. 7a to 7c.

The procedure to obtain p(R) from Monte Carlo generated data still involves a counting of the path crossings. It would be most beneficial to be able to construct a distribution directly from the R values of the crossing points from the Monte Carlo data, without counting them. This is possible, in fact, if one constructs the cumulative probability distribution first. All that is required is that one orders according to increasing magnitude the R values of the crossing points and plots the results. When this is done the smoothest distribution is obtained with a given number of ion paths. For this reason in the present study the cumulative probability distribution will always be constructed. Then p(R) and I(R) can be obtained when necessary from P(R).

The construction of the cumulative probability curve is now explained in greater detail. Consider the curve obtained from the Monte Carlo data by having the Monte Carlo simulation record only the value of the radius R from the beam axis of the crossing point of the ion path at each target plane. These values are then sorted in increasing magnitude for each particular plane. The sorted values are then plotted in the following manner. The distance R is recorded along the x-axis and the percentage point through the data file of the sorted R value is recorded on the y-axis. The first value of R (the smallest) is plotted at (R_1, 1/ITOTP) and the next smallest is plotted at (R_2, 2/ITOTP), and so on. The curve that would be produced by this process in shown in Fig. 7c and is, by nature of construction, the cumulative probability distribution of the lateral displacement of the ion beam. This curve represents the fact that the probability of the ion path crossing the target plane at a distance of R or less is P(R). In this manner the Monte Carlo simulation data is employed directly to produce a curve from which the intensity distribution can then be obtained. Note that ITOTP is the total number of ion paths for the simulation.

For the Monte Carlo simulations, certain initial conditions are required. These are given below. The constant N_0 is set to be the value of the number density of molecular hydrogen at a pressure of one atmosphere and a temperature of 288 K, and it is the same value for all of the density distributions in this study with the exception of the free-jet density profile. Therefore,

$$N_0 = 5.0946 \times 10^{19} \text{ atoms/cm}^3. \tag{2.23}$$

To evaluate the mean free path the total collisional cross section Q must be known. From appendix B the equation for Q is

$$Q = \pi a_0^2 \left(\frac{m}{m_0}\right)^2 \frac{4 + 6E_X + 7E_X^2/3}{(1 + E_X)^3}, \tag{2.24}$$

where E_x is a convenient nondimensional mass-weighted energy to be mentioned. The known quantity in an experiment of this type is generally the energy of the ion as it leaves the source and not the energy of the collision; therefore, E_x will be written in terms of the energy and mass of the proton. Now

$$E_x = mE/m_0E_0, \tag{2.25}$$

but from Eq. 6 of appendix B,

$$E = \hbar^2k^2/2m; \tag{2.26}$$

therefore,

$$E = \hbar^2k^2/2m = (m_p/m)\,\hbar^2k^2/2m_p = m_pE_p/m, \tag{2.27}$$

where m_p is the mass of a proton and E_p is the energy of the proton. As a consequence,

$$E_x = m_pE_p/m_0E_0. \tag{2.28}$$

The reduced mass m for protons colliding with hydrogen molecules is

$$m = m_p(2m_p)/(m_p + 2m_p) = 2m_p/3. \tag{2.29}$$

This completes the data specification for the Monte Carlo computer code.

2.6 Numerical Results and Discussion

The numerical results from the Monte Carlo simulation for a number of interesting examples of the spreading of ions from a point source as they pass through a scattering medium are now presented and discussed. For exemplary reasons the ion used in the simulations will be the proton and the scattering medium will be gaseous molecular hydrogen.

Example 1: Constant scattering density and constant proton energy

This Monte Carlo simulation is aphysical in that the proton energy remains constant or is unattenuated with distance. In an actual case the proton would, of course, lose energy as it experienced collisions during its random walk, and this is ignored for this case only. For this simulation the hydrogen density is constant; therefore,

$$\lambda = -\bar{\lambda}_c \ln(r) = \frac{-1}{N_0Q}\ln(r) \tag{2.30}$$

from Eq. 2.5 for the free path length. The angles ϕ and θ are calculated from Eqs. 2.8 and 2.9 respectively.

The first set of Monte Carlo simulation results are presented graphically in the form of the cumulative probability distributions P(R) in Fig. 8. These distributions, labelled 1 to 8, were constructed for different target planes at increasing distances from the point source, as tabulated on the next page.

Target Plane Number	Penetration Depth (mean free paths)	(cm)	R for P(R) = 0.5 R* (cm)
1	100	8.629	2.46184×10^{-3}
2	200	17.258	7.54377×10^{-3}
3	500	43.145	3.22668×10^{-2}
4	1000	86.290	9.15732×10^{-2}
5	2000	172.580	0.2802619
6	3000	258.870	0.4969370
7	4000	345.160	0.7652349
8	5000	431.450	1.100479

All of these results were generated by following 500 paths of protons with an energy of 10 MeV from the point source to a distance of 5000 mean free paths ($\bar{\lambda}_c$ = 0.08629 cm), through molecular hydrogen with a density of 5.0946×10^{19} atoms/cm^3. The lateral dispersion behaviour of the proton beam as a function of penetration depth can be seen clearly. Note that the jaggedness in the distributions increases at larger distances, simply because the same number of points constitute each curve but are spread further apart in each consecutive curve. This jaggedness could be diminished, of course, if more proton paths were followed.

The successive cumulative probability distributions, although spread out, look similar in shape. In order to investigate the degree of similarity of the curves, the R values for each distribution are divided by the corresponding R value for which P(R) = 0.5, which is denoted by R* for brevity. The resulting scaled curves are shown in Fig. 9. The self similarity of the scaled curves is readily apparent. Self similarity is excellent for P(R) values less than 0.8 and is fair for larger values.

The spreading of the curves for P(R) values greater than 0.8 is expected and is the result of not incorporating a sufficient number of statistics in this example. That is, not enough collisions are being considered or not enough proton paths are being followed to generate each distribution. A sufficient number of statistics are incorporated in both the azimuthal angle and the free path length; however, the number of scattering angles sampled was simply not sufficient to adequately represent the scattering angle distribution due to the sharpness of this distribution (see Fig. 4 of appendix B). The rapid change in this distribution and its long tail from θ in the range of 10^{-4} to π radians requires that the number of collisions be extremely large in order to properly account for the tail of the distribution. For a proton energy of 10 MeV, one scattering angle of $\pi/6$ or greater would require more than 200 million collisions. If more proton paths were followed, smoother distributions would be obtained, and this would very likely make the self similarity more obvious.

Each distribution at a target plane was generated with a different number of statistics, that is, although the number of proton paths remained constant

the number of collisions required to reach each plane was different. It would be more reasonable if an equal number of statistics was employed to generate each distribution. This was done to check the self similarity of the distributions. The number of proton paths was altered for each plane in order to have each distribution constructed with the same number of collisions, rather than the same number of paths. The cumulative probability distributions for this case are shown in Fig. 10, for the same proton energy of 10 MeV and molecular hydrogen density of 5.0946×10^{19} atoms/cm^3. The distributions in this figure resemble closely the cumulative probability distributions obtained by using an equal number of proton paths. Note that target plane number 1 is not included here, owing to the large number of proton paths (25,000) that would be needed, which would be very costly to complete. The number of collisions employed to generate each distribution is constant at 2.5 million, and the number of paths to the target planes 200, 500, 1000, 2000, 3000, 4000 and 5000, are 12500, 5000, 2500, 1250, 833, 650 and 500, respectively. In order to examine any reduction in the variation of the cumulative probability distributions, the distributions in Fig. 10 are scaled in the same manner as before for Fig. 9. The result of this scaling is shown in Fig. 11. As can be seen, there is some improvement in that the curves lie closer together. Sufficient statistics, however, are still not incorporated to significantly reduce the variation in the distributions. Note that in this figure the two insets show both the gas density and proton energy variations as a function of the penetration depth. The abscissa indicates the relative separation between successive target planes (1 to 8).

The large number of proton paths considered to construct the target-plane distribution at a distance of 200 mean free paths from the point source provides a test of the effect of the randomness of the Monte Carlo simulation. The raw data from the Monte Carlo simulation was broken into 12 consecutive groups of 1000 proton paths. These 12 groups were then treated as individual Monte Carlo simulations and, therefore, 12 separate experiments. The scaled distributions obtained from this procedure are shown in Fig. 12. The resulting scatter in these scaled distributions is of the same order of magnitude as those in Figs. 9 and 11. Therefore, it can be concluded that a large proportion of the scatter obtained in the Monte Carlo generated cumulative probability distributions arises from the randomness introduced into the Monte Carlo simulation by not having a sufficient number of statistics for the scattering angle.

The Monte Carlo simulation induced variations in the distributions could be reduced by considering a larger number of proton paths; however, this would result in too great of an increase in computer costs to be considered here. In stating this, it is realized that the Monte Carlo simulated results will not be the exact solution to the problem being discussed here. However, the results obtained will be "first-order" accurate with most of the variations occurring in the resulting curves arising from the randomness of the Monte Carlo simulation. In spite of this variation the results obtained from the simulation are quite good. Although this study cannot prove more conclusively that self similarity exists between the individual cumulative probability distributions, it is fully expected that this does in fact occur.

The results presented so far were all obtained for a proton energy of 10 MeV and a gas density of 5.0946×10^{19} atoms/cm^3. It is important to investigate the effects of different proton energies and different gas densities on the shape of the cumulative probability distributions, in order to see if similarity carries over from case to case. Three seprate cases were considered as

follows:

a) $E_p =$ 10 Mev, $N_0 = 5.0946 \times 10^{19}$ cm^{-3}, $\bar{\lambda}_c = 8.629 \times 10^{-2}$ cm,

b) $E_p = 0.01$ Mev, $N_0 = 5.0946 \times 10^{19}$ cm^{-3}, $\bar{\lambda}_c = 8.629 \times 10^{-5}$ cm,

c) $E_p =$ 10 Mev, $N_0 = 5.0946 \times 10^{18}$ cm^{-3}, $\bar{\lambda}_c = 8.629 \times 10^{-1}$ cm.

The scaled results from these three simulations are all combined in Fig. 13. The scatter in the distributions at larger P(R) values still exists but is of the same degree experienced in each individual simulation. Therefore, it can be concluded that self similarity occurs for other cases of constant proton energies and gas densities, and that similarity also exists from one case to another. Additional Monte Carlo results for other constant proton energies and molecular hydrogen densities, which are not presented here for brevity, are very similar and reinforce the above conclusions.

Now that self similarity within each simulation and similarity from one simulation to the next has been established, a scaling law can be developed for the numerical results. In order to accomplish this a particular point on each distribution must be tagged and then that point followed from target plane to target plane. Because the distributions are self similar, any point on the distribution will therefore suffice. For simplicity, the R value corresponding to P(R) = 0.5 is tagged and followed. This R value will be denoted as R* for simplicity.

Assume a scaling law which has a functional dependence of the form

$$R^* = a\, n^b, \tag{2.31}$$

where a and b are constants and n is the number of mean free paths required to reach the target plane. In order to determine the constant b in the above relation, the ratio of the R* value of the farthest target plane (n = 5000) to the R* value of each of the other target planes is considered and the logarithm of that ratio taken. A linear regression fit to the straight line

$$\ln(R^*_{5000}/R^*_n) = b\, \ln(5000/n) + c, \tag{2.32}$$

where the constant c should be zero, was completed by using a TI-58C calculator and taking into consideration the Monte Carlo generated data for the three cases listed above. It was found that b = 1.5505 and c = 0.00188. The data, and the corresponding fitted curve, is shown in Fig. 14. The constant c is negligible compared to the first term; therefore, the functional dependence of R* on the penetration distance is simply

$$R^* = A\, y^{1.5505} \text{ cm}, \tag{2.33}$$

where A is a constant that will be both density and energy dependent and y is the distance measured in cm.

In order to determine the dependence on the energy of the proton and the density of the scattering medium in the scaling law, the ratios of the values of R* for a particular target plane were formed for the three cases listed above. It was found that, to a good approximation,

$$R^* = 1.8174 \times 10^{-13}\, N_0^{1/2}\, y^{1.5505}/E_{p_{in}} \text{ cm}, \tag{2.34}$$

where N_0 is in units of atoms/cm^3, $E_{p_{in}}$ is in MeV, and y is in cm.

This scaling law can now be used to obtain the R* value of the cumulative probability distribution at any penetration depth, proton energy, and hydrogen gas density, provided that the proton energy and gas density are constant. Once the R* value has been obtained the entire curve is known because of the self similarity of the distribution with distance and the similarity from problem to problem.

In order to obtain the cumulative probability distribution numerically or graphically to use in conjunction with the scaling law just developed, a smooth distribution should be obtained from the Monte Carlo simulation. This cumulative probability distribution could then be normalized with respect to its R* value to obtain a smooth reference curve. This curve, along with the scaling law prediction for the R* value of the distribution given by Eq. 2.34, represents all of the data obtainable from a Monte Carlo simulation for different proton energies, hydrogen gas densities, and any penetration depth.

A smooth reference distribution was constructed from the Monte Carlo simulation of 12,500 proton paths from a point source to a distance of 200 mean free paths. The proton energy for this simulation was 10 MeV and the gas density was 5.0946×10^{19} atoms/cm^3. This cumulative probability distribution is shown graphically in Fig. 15, and it is tabulated in table 2 as a function of $E_{p_{in}}/N_0^{1/2} y^{1.05505}$ (MeV-cm$^{0.9495}$). To use this curve the values tabulated in table 2 must be multiplied by

$$N_0^{0.5}\, y^{1.5505}/E_{p_{in}}\,, \tag{2.35}$$

where $E_{p_{in}}$ is the initial proton energy in MeV, N_0 is the initial number density of the hydrogen gas in atoms/cm^3, and y is the penetration depth in cm. The resulting radial distance R is then in cm.

In section 2.3 it was stated that a comparison of the results generated by the Monte Carlo simulation and the Gaussian approximation for multiple small angle scattering would be considered. This comparison would indicate whether or not the Monte Carlo simulation was producing results that are theoretically and experimentally correct. If the dispersion of the beam is due to many small angle collisions, all of the same order of magnitude, then a Gaussian distribution of ions would be expected [9]. However, when a single large angle scattering cross section is added to the analysis, the distribution obtained is that of a Gaussian with a stretched tail called the single large angle scattering tail [17]. This tail is the result of collisions for which the scattering angle is much larger than average. These scattering events, although infrequent, succeed in pushing the ion farther away from the beam axis, and this results in the larger or stretched tail.

If the reference cumulative probability curve generated by the Monte Carlo simulation is now compared to a Gaussian distribution, the tail of the reference curve should be longer than that of the Gaussian. This comparison is shown in Fig. 16, in which the Gaussian distribution and the Monte Carlo reference curve are matched at the point where P(R) = 0.5. As can be seen from the figure, the distribution obtained is a Gaussian distribution but with an extended tail. This extended tail has the trend both predicted by theory and measured by experiment [17]. Therefore, it can be concluded that the Monte Carlo simulation gives results that have the correct physical shape.

Figure 16 shows that the Gaussian distribution does not accurately represent the entire cumulative probability distribution obtained from the Monte Carlo simulation. In order to produce an analytical function that matches the Monte Carlo generated distribution, a suitable curve was fitted to the data in table 2. It is necessary to obtain a function that resembles the Gaussian distribution initially but has a longer tail. If the $\text{Arctan}(R^2/R^{*2})$ function is considered, it will have too long of a tail. Therefore, a linear combination of the two functions - the Gaussian and the arctangent - was fitted to the data in table 2. It is found that the Monte Carlo data is represented well by the function

$$P(R) = \frac{1}{2}\left[1 - \exp\left(-\ln(2)[R/R^*]^2\right)\right] + \frac{1}{\pi}\text{Arctan}([R/R^*]^2), \quad (2.36)$$

A graphical comparison between this curve fit and the Monte Carlo generated distribution is given in Fig. 17 for interest. The curve fit is a very good representation of the Monte Carlo data.

Example 2: Constant scattering density and varying proton energy

This Monte Carlo simulation is physical in that the energy of the proton in decreased in accordance with experimental data as described in section 2.4. Consider the case where the density of the hydrogen gas is constant at one atmosphere and 288 K, and the energy of the ion is initially 10 MeV. The positions of the target planes of interest are described as being so many mean free paths ($\bar{\lambda}_c$) of the ion when it is at the position y = 0. The angles ϕ and θ are obtained from Eqs. 2.8 and 2.9, and the free path length is obtained from Eq. 2.32.

The Monte Carlo generated cumulative probability distributions are given in Fig. 18. These distributions, labelled 1 to 8, were constructed for target planes at increasing distances from the point source, as tabulated below.

Target Plane Number	Penetration Depth (mean free paths)	(cm)	R for P(R) = 0.5 R* (cm)	Proton Energy (MeV)
1	100	8.629	2.4906×10^{-3}	9.9253
2	200	17.258	7.1912×10^{-3}	9.8495
3	500	43.145	3.1728×10^{-2}	9.6188
4	1000	86.290	9.3764×10^{-2}	9.2237
5	2000	172.580	0.27699	8.3864
6	3000	258.870	0.53633	7.4717
7	4000	345.160	0.90327	6.4512
8	5000	431.450	1.33641	5.2727

All of these results were generated by following 500 paths of protons with an initial energy of 10 MeV from the point source to a distance of 5000 initial mean free paths ($\bar{\lambda}_C$ = 0.08629 cm), through molecular hydrogen with a density of 5.0946×10^{19} atoms/cm^3. The lateral dispersion behaviour of the proton beam as a function of penetration depth can be seen clearly.

The scaled cumulative probability distributions for this example are shown in Fig. 19. Again the self similarity of the distributions is very good for values of P(R) less than about 0.8, but scatter exists for larger values of P(R). However, the scatter that is present is only slightly larger than that incurred by the randomness of the Monte Carlo simulation (see Fig. 12), and thus most of the scatter is attributed to the simulation (i.e., an insufficient number of statistics for the scattering angle).

Another very interesting aspect of Fig. 19 is the comparison of the smooth thick reference curve with the rest of the distributions. It lies in the center of the distributions. This curve is not the average of the other curves but rather it is the cumulative probability reference distribution constructed from example 1. This reference distribution was obtained from a completely aphysical simulation (constant proton energy) but it has the same shape as the distributions generated from this physically real example. This means that the reference distribution has the same shape as that of the distributions for this new example, and similarity is now extended to this case with a varying proton energy.

Now that it has been found that the shape of the cumulative probability distribution has not changed it is interesting to find out to what extent the scaling law given by Eq. 2.34 is applicable. Note that it should not be expected that the scaling law will be very accurate, because the varying energy of the proton is not accounted for in its development. The Monte Carlo generated data for the R* values of the various target planes is shown in Fig. 20 along with the straight line given by Eq. 2.34. In this figure it is seen that the scaling law prediction for the R* values of the farthest planes is too small. This behaviour is to be expected because of the decreasing energy of the proton. However, at the target planes where the energy of the proton is not significantly attenuated the scaling law prediction is within a few percent of the Monte Carlo generated values.

Example 3: Linearly increasing scattering density and varying proton energy

Consider a linearly varying density $N = N_0(1 + by)$ for which the density doubles after 500 initial mean free paths, that is, $b = 1/(500\bar{\lambda}_C)$. The angles ϕ and Θ are obtained from Eqs. 2.8 and 2.9 and the free path length is obtained from Eq. 2.5 as (Eq. 17 of appendix A)

$$\lambda = \frac{1}{b}(1+by_1)\left[\sqrt{1 - \frac{2b\bar{\lambda}_C \ell n(r)}{(1+by_1)^2}} - 1\right] . \qquad (2.37)$$

The Monte Carlo generated cumulative probability distributions are given in Fig. 21. These distributions, labelled 1 to 7, were constructed for target planes at increasing distances from the point source, as tabulated on the next page.

Target Plane Number	Penetration Depth (mean free paths)	(cm)	R for P(R) = 0.5 R* (cm)	Proton Energy (MeV)
1	100	8.629	2.51504×10^{-3}	9.917
2	200	17.258	7.58537×10^{-3}	9.819
3	400	34.516	2.59852×10^{-2}	9.572
4	600	51.774	5.31737×10^{-2}	9.255
5	800	69.032	8.76831×10^{-2}	8.863
6	1000	86.290	0.162617	8.385
7	1200	103.550	0.1796409	7.810

All of these results were generated by following 500 paths of protons with an initial energy of 10 MeV from the point source to a distance of 1200 initial mean free paths ($\bar{\lambda}_c = 0.08629$ cm), through molecular hydrogen with an initial density of 5.0946×10^{19} atoms/cm^3.

The scaled cumulative probability distributions for this example are shown in Fig. 22. The self similarity of the distributions is again very good for P(R) values below about 0.7, but scatter exists for higher values. However, the amount of scatter present is of the same magnitude as the Monte Carlo induced scatter (see Fig. 12), and thus it can be concluded that self similarity very likely exists for these distributions.

In Fig. 22, the thick smooth curve is again the reference curve generated for example 1. It again has the same shape as the distributions generated in this example, showing that similarity is also extended to this example of an increasing scattering density. Because the scaling law developed in example 1 might be of use for the current example, the Monte Carlo generated data for the R* values at the various target planes are given in Fig. 23, along with the line generated by the scaling law equation (Eq. 2.34). It can be seen from this figure that the first two target planes have had their R* value predicted well, but the scaling law gives results that are much too small for the remaining target planes. This behaviour can be explained by the rising scattering density and the falling proton energy. The decreasing proton energy causes the prediction to drop as experienced in example 2 and the density now increases the deviation for the same reason. It must be concluded that the empirical scaling law developed for example 1 is not very useful for this current example.

Example 4: Linearly decreasing scattering density and varying proton energy

Consider a linearly varying density $N = N_0(1 - by)$ for which the density of the scattering medium is zero after 5000 initial mean free paths, that is, $b = 1/(5000\bar{\lambda}_c)$. The same equations apply for this example as apply for example 3, because the only change is that the density now decreases with distance instead of increases.

The Monte Carlo generated cumulative probability distributions are given in Fig. 24. These distributions, labelled 1 to 8, were constructed for different target planes at increasing distances from the point source, as tabulated below.

Target Plane Number	Penetration Depth (mean free paths)	(cm)	R for P(R) = 0.5 R* (cm)	Proton Energy (MeV)
1	100	8.629	2.19372×10^{-3}	9.926
2	200	17.258	6.75508×10^{-3}	9.852
3	500	43.145	2.95470×10^{-2}	9.638
4	1000	86.290	9.11058×10^{-2}	9.304
5	2000	172.258	0.264821	8.730
6	3000	258.887	0.491845	8.300
7	4000	345.160	0.735808	8.032
8	4500	388.310	0.864582	7.965

All of these results were generated by following 500 paths of protons with an initial energy of 10 MeV from the point source to a distance of 4500 initial mean free paths ($\bar{\lambda}_C = 0.08629$ cm), through molecular hydrogen with an initial density of 5.0946×10^{19} atoms/cm^3.

The scaled cumulative probability distributions for this example are shown in Fig. 25. Again the self similarity of the distributions is extremely good although some scatter still occurs for P(R) values greater than 0.7. However, the scatter that is present is still of the same magnitude as the scatter that is induced by the Monte Carlo simulation itself (see Fig. 12), and thus it can be concluded that the cumulative distributions obtained are again very likely self similar.

In Fig. 25 the thick smooth curve is again the reference curve generated for example 1, and it again has the same shape as the distributions generated in this example. Therefore, the scaling law developed in example 1 is checked to see if it applies for the current example. The Monte Carlo generated data for the R* values of the various target planes is given in Fig. 26, along with the line generated by the scaling law equation (Eq. 2.34). As can be seen from this figure, the empirical prediction is initially a little too large, owing to the decreasing density not accounted for in the empirical equation. However, the Monte Carlo data points begin to approach the empirical curve and then deviate again. This is due to the compensating effects of the decreasing density and the decreasing energy. Therefore, the accuracy of empirical prediction is due only to the fortuitous chance of these counterbalancing effects.

Example 5: Exponentially increasing gas density and varying proton energy

Consider an exponentially increasing density $N = N_0 \exp[b(y-a)]$, for which $b = 1/(1000\bar{\lambda}_c)$ and $a = 3000\bar{\lambda}_c$. The angles ϕ and θ are determined from Eqs. 2.8 and 2.9 and the free path length is determined from Eq. 2.5 as (Eq. 18 of appendix A)

$$\lambda = \frac{1}{b} \ell n \left[1 - b\bar{\lambda}_c \ell n(r) \exp[b(a - y_1)] \right], \qquad (2.38)$$

where $\bar{\lambda}_c = 1/N_0 Q$. In this example the target planes are specified in terms of the number of $\bar{\lambda}_c$s. The Monte Carlo generated cumulative probability distributions are given in Fig. 27. These distributions, labelled 1 to 9, were constructed for different target planes at increasing distances from the point source, as tabulated below.

Target Plane Number	Penetration Depth (mean free paths)	(cm)	R for P(R) = 0.5 R* (cm)	Proton Energy (MeV)
1	1000	86.29	1.95222×10^{-3}	9.936
2	2000	172.58	7.35981×10^{-2}	9.758
3	2500	217.73	0.166190	9.573
4	3000	258.87	0.180296	9.261
5	3200	276.13	0.209753	9.082
6	3500	302.02	0.263745	8.728
7	3800	327.90	0.328804	8.229
8	4000	345.16	0.373129	7.781
9	4200	362.42	0.428605	7.204

All of these results were generated by following 500 paths of protons with an initial energy of 10 MeV from the point source to a distance of 4200 initial mean free paths ($\bar{\lambda}_c$ = 0.08629 cm), through molecular hydrogen with the constant $N_0 = 5.0949 \times 10^{19}$ atoms/cm^3.

The scaled cumulative probability distributions for this example are shown in Fig. 28. Again the self similarity of the distributions is very good, but scatter again exists for P(R) values greater than 0.7. However, the scatter is of the same magnitude as that introduced by the randomness of the Monte Carlo simulation, and thus it can be concluded that the curves are self similar.

In Fig. 28 the thick smooth curve is again the reference curve generated for example 1. It also has the same basic shape as the distributions generated in this example, and it illustrates that similarity is also extended to this

problem. In order to check the scaling law developed in example 1, the Monte Carlo generated data for the R* values of the various target planes is given in Fig. 29, along with the line generated by the scaling law equation (Eq. 2.34). It can be seen from this figure that the empirical scaling law is accurate only for the first target plane. The prediction is accurate for this plane simply because the gas density and proton energy variations are very small up to this plane. The extreme change in gas density not accounted for in the scaling law accounts for the large discrepancy in the other results. It must be concluded that the scaling law is not very useful for this example.

Example 6: Exponentially decreasing gas density and varying proton energy

Consider an exponentially decreasing density $N = N_0 \exp[-b(y-a)]$, for which $b = 1/(1000\bar{\lambda}_c)$ and $a = 1200\bar{\lambda}_c$. The equations for calculating λ, ϕ, and Θ are the same as the equations used in example 5. In this example the target planes are specified in terms of the number of mean free paths of the ion when it is at the position $y = a$. The Monte Carlo generated cumulative probability distributions are given in Fig. 30. These distributions, labelled 1 to 10, were constructed for different target planes at increasing distances from the point source, as tabulated below.

Target Plane Number	Penetration Depth (mean free paths)	(cm)	R for P(R) = 0.5 R* (cm)	Proton Energy (MeV)
1	100	8.629	4.58055×10^{-3}	9.761
2	200	17.258	1.37220×10^{-2}	9.539
3	400	34.516	4.82780×10^{-2}	9.147
4	800	69.032	0.122729	8.536
5	1000	86.290	0.172592	8.301
6	1500	129.440	0.308921	7.869
7	2000	172.580	0.468089	7.597
8	3000	258.870	0.826468	7.324
9	4000	345.160	1.18736	7.222
10	5000	431.450	1.55396	7.184

All of these results were generated by following 500 paths of protons with an initial energy of 10 MeV from the point source to a distance of 5000 $\bar{\lambda}_c$s ($\bar{\lambda}_c = 0.08629$ cm), through molecular hydrogen with $N_0 = 5.0949 \times 10^{19}$ atoms/cm^3.

The scaled cumulative probability distributions for this example are shown in Fig. 31. Again the self similarity of the distributions is very good, and scatter also exists for P(R) values greater than 0.7. However, the scatter

that is present is only slightly larger than that incurred in the randomness of the Monte Carlo simulation (see Fig. 12) and thus most of the scatter can be attributed to the simulation. The remainder of the scatter could very well be attributed to an insufficient number of statistics being considered, as discussed earlier.

In Fig. 31 the thick smooth curve is again the reference curve generated for example 1, and it again has the same shape as the distributions generated in this example. To check on the scaling law developed in example 1, the Monte Carlo generated data for the R* values of the various target planes is given in Fig. 32, along with the line generated by the scaling law equation (Eq. 2.34). In this example the scaling law prediction is good for most of the target planes, with the third plane probably being a spurious point. This accuracy was not expected but results from the fortuitous counterbalancing of the two effects of the proton energy loss and the scattering density decrease. This balancing will not occur in general, and thus the scaling law should not be used for such problems.

Example 7: Free-jet expansion scattering density and varying proton energy

Consider a free-jet flow field typical of that occurring in gas-target neutron generators [3-6]. As sketched in Fig. 1, the ion beam is directed along the free jet and orifice axis and comes to a stop inside of the orifice flow where the gas is most dense. The density of such a flow field is well represented empirically by

$$N = N_{orf}[\, 1 + H(\chi_{orf} - \chi)\{\chi_{orf} - \chi\}^2]^{-1}, \tag{2.39}$$

where

$$\chi = y/D \tag{2.40}$$

and

$$H(\chi) = 4\,\frac{1 + C\chi/10}{1 + 4\chi/10}\,. \tag{2.41}$$

In these expressions N_{orf} is the number density in atoms/cm^3 of the free jet at the orifice, D is the diameter of the orifice, χ is the dimensionless distance from the source, χ_{orf} is the dimensionless position of the orifice, and

$$C = \left[\frac{\gamma-1}{\gamma+1}B^2\right]^{\frac{1}{\gamma-1}}, \tag{2.42}$$

where γ is the ratio of the specific heats of the gas and B equals 3.65 is a constant chosen to fit the available theoretical and experimental data. This equation is the result of a curve fit to such data given in Ref. 18.

In the Monte Carlo computer code this density field was specified according to Eq. 2.39. In order to calculate the free path length, the gas density variation was taken to be a linear variation locally, and then the local slope was obtained from the derivative of Eq. 2.39 and used in Eq. 2.37 to calculate λ. The Mach disk was taken into account, at which the density increases by a factor of six in the flow direction owing to the strong shock wave. Behind the

Mach disk the density is assumed to be constant [18-20] and is denoted as N_{inf}.

A Monte Carlo simulation was done for the following free-jet parameters:

$$D = 2 \text{ cm},$$

$$\chi_{orf} = 50,$$

$$\gamma = 1.4 \text{ (diatomic gas)},$$

$$N_{orf} = 5 \times 10^{19} \text{ atoms/cm}^3,$$

$$N_{inf} = 1.8 \times 10^{17} \text{ atoms/cm}^3,$$

and the location of the Mach disk was y = 70 cm. The initial energy of the proton was 0.4 Mev.

The Monte Carlo generated cumulative probability distribution for this example is given in Fig. 33. This distribution was constructed at a target plane located at the the flow exit of the orifice for the free-jet expansion. The data generated by the Monte Carlo simulation for this example is shown in the table below.

Target Plane Number	Penetration Depth (cm)	R for P(R) = 0.5 (cm)	Proton Energy (MeV)
1	100	0.146635	0.131

For this set of results, 1000 proton paths were followed from the point source to the orifice. For this case the energy of the proton falls from 0.4 MeV at the source to 0.13 MeV at the orifice.

The scaled cumulative probability distribution for this example is shown in Fig. 34. The thick smooth curve is again the reference curve generated for example 1, and it again has the same shape as the distribution generated in this example. To check on the scaling law developed in example 1, the Monte Carlo generated data for the R* value of the target plane is given in Fig. 35, along with the line generated by the scaling law equation (Eq. 2.34). In this example the scaling law prediction is reasonably accurate because the range over which the proton energy and scattering density varies is small compared to the distance that the proton travels.

2.7 Conclusions

The Monte Carlo method is good for handling a wide variety of density distributions in this type of problem. The method is easily set up and the computer programming is not very involved. It is, however, a very expensive procedure to use. The average Monte Carlo CPU time was approximately 2 hours on a Perkin Elmer 3250 computer. The results obtained resemble the experimental oberservations in that the cumulative probability distribution obtained is the multiple small angle scattering Gaussian distribution with an added

large angle scattering tail.

The Monte Carlo simulation results for each of the various examples considered showed that the cumulative probability distribution for the lateral spreading of an ion beam is a self similar function of penetration depth within each example. Further, the Monte Carlo simulation showed that the cumulative probability distribution has the same shape for all of the examples considered. As a result of this similarity a simple scaling law was developed for predicting the R value for which $P(R) = 0.5$ for the aphysical case of constant proton energy and constant scattering density. In order to make use of this scaling law, a smooth distribution was obtained from a Monte Carlo simulation of 12,500 proton paths and the curve was normalized and tabulated for later use.

The simple scaling law was found to be of only limited use for most of the examples considered in this study. This might have been expected, owing to the simple analysis used in its development, which did not include the effects of variations in the proton energy and scattering density. If the scattering density variation is not too extreme and the energy of the proton is not allowed to be attenuated by more than about 20 percent, then the scaling law is useful for giving a quick indication of the extent of the lateral spreading. However, if a more appropriate scaling law could be developed to account for variations of both the proton energy and the scattering density, then the accuracy of the predicted distribution should be improved significantly. This is considered in the next chapter.

The possibility of analytically predicting the lateral spreading of the cumulative probability distribution for each problem and from one problem to another would have a number of benefits. This would include a tremendous saving in computing costs; the Monte Carlo simulation would only need to be run once for a large number of proton paths and for a relatively short distance to generate a reference distribution for use with the analytical scaling law, thus saving many hours of CPU time. Also, it was found that the Monte Carlo simulation does not produce smooth cumulative probability distributions, because of the limited number of statistics that could be used in the simulation. An analytical scaling law would have the benefit of considering average or expected values for all of the variables concerned and thus effectively consider an infinite number of proton paths, which obviously the Monte Carlo simulation cannot do.

3.0 ANALYTICAL APPROXIMATION OF ION BEAM SPREADING IN A SCATTERING MEDIUM

3.1 Introduction

The simplistic scaling law developed in the previous chapter was seen to be not very accurate whenever an extreme density change and/or extreme energy variation was experienced. This breakdown can be attributed to the inadequate development of the scaling law, which did not take into account any changes in the ion energy or scattering medium density. For this reason it is beneficial to develop a scaling law that includes both the ion energy variation and the scattering density variation. Another more important reason for developing an analytical scaling law is that the expensive Monte Carlo simulation can then be dispensed with and replaced by a quick and easy numerical integration, thus saving computing costs by a factor of at least two orders of magnitude. The purpose of this chapter is the development of such an analytical scaling law and an evaluation of its usefulness.

3.2 Analytical Development of the Scaling Law

The lateral displacement of the ion as it traverses the scattering medium is conveniently recorded by its Cartesian coordinates after each collision. From Fig. 36 it is seen that the Cartesian coordinates of the ion after it has experienced n collisions are

$$x_n = \sum_{i=1}^{n} \lambda_i u_i, \qquad y_n = \sum_{i=1}^{n} \lambda_i v_i, \qquad z_n = \sum_{i=1}^{n} \lambda_i w_i, \quad (3.1)$$

where $\bar{n}_i = [u_i, v_i, w_i]$ are the direction cosines of the ion path during the ith step and λ_i is the path length during the ith step. If the vector components $\bar{n}_{i-1} = [u_{i-1}, v_{i-1}, w_{i-1}]$ are the direction cosines of the ion during the (i-1)st step, and Θ_i and ϕ_i are the deflection angles from the line-of-flight direction for this ith collision, then $\bar{n}_i$ can be determined from these variables by

$$\begin{aligned}
u_i &= [\sin(\Theta_i)\cos(\phi_i)u_{i-1}w_{i-1} - \sin(\Theta_i)\sin(\phi_i)v_{i-1}]/\sqrt{1-w_{i-1}^2} + \cos(\Theta_i)u_{i-1}, \\
v_i &= [\sin(\Theta_i)\cos(\phi_i)v_{i-1}w_{i-1} + \sin(\Theta_i)\sin(\phi_i)u_{i-1}]/\sqrt{1-w_{i-1}^2} + \cos(\Theta_i)v_{i-1}, \\
w_i &= -\sin(\Theta_i)\cos(\phi_i)\sqrt{1-w_{i-1}^2} + \cos(\Theta_i)w_{i-1},
\end{aligned} \quad (3.2)$$

which are the same as Eqs. 2.13. The angle Θ_i is always small in this work; therefore, the small-angle approximation leads to

$$\cos(\Theta_i) = 1 \qquad \text{and} \qquad \sin(\Theta_i) = \Theta_i. \quad (3.3)$$

Equations 3.2 are unstable if $|w|$ is too close to unity [11]. Hence, the initial direction $\bar{n}_0 = [0, 1, 0]$ was chosen in chapter 2, and it is also used here. Therefore, u_i and w_i are always small and v_i is almost unity. The substitution of this information in Eqs. 3.2 yields

$$\begin{aligned}
u_i &= -\Theta_i \sin(\phi_i) + u_{i-1}, \\
v_i &= v_{i-1}, \\
w_i &= -\Theta_i \cos(\phi_i) + w_{i-1},
\end{aligned} \quad (3.4)$$

after terms of second order in smallness are discarded. Equations 3.4 can be rewritten as

$$\begin{aligned}
u_i &= -\sum_{j=1}^{i} \Theta_j \sin(\phi_j), \\
v_i &= 1, \\
w_i &= -\sum_{j=1}^{i} \Theta_j \cos(\phi_j).
\end{aligned} \quad (3.5)$$

The lateral displacement R of the ion from its initial direction after n collisions is

$$R_n^2 = x_n^2 + z_n^2, \quad (3.6)$$

which becomes

$$R_n^2 = \sum_{i=1}^{n} \sum_{j=1}^{n} (\lambda_i \lambda_j u_i u_j + \lambda_i \lambda_j w_i w_j) \qquad (3.7)$$

when Eqs. 3.1 are used. Equation 3.7 can be rewritten in a more convenient form, with the use of Eqs. 3.5 as

$$R_n^2 = \sum_{i=1}^{n} \sum_{j=1}^{n} \lambda_i \lambda_j \left[\sum_{k=1}^{i} \sum_{\ell=1}^{j} \Theta_k \Theta_\ell \cos(\Theta_k - \Theta_\ell) \right] . \qquad (3.8)$$

If the number of collisions considered is small, this formula can be used directly to calculate the R_n^2 value of the distribution. However, if the number of collisions is large, the direct use of this equation becomes unreasonable. One method of handling this difficulty is to calculate the expected value of the sum and thus the expected value of R_n^2. After all, only one value of the cumulative probability curve is required to predict the entire distribution, because the distribution profiles are self similar for each example and similar from one example to the next. Thus, if the square root of the expected value of R_n^2 (the RMS value) can be determined, then, because of the similarity of the cumulative probability distribution, the whole curve can be obtained.

To calculate the expected value of R_n^2 in Eq. 3.8 the following properties of the expected value are used,

$$E\{\lambda_i \lambda_j\} = \begin{cases} E\{\lambda_i\} E\{\lambda_j\} & \text{if } i \neq j, \qquad (3.9) \\ E\{\lambda_i^2\} & \text{if } i = j, \qquad (3.10) \end{cases}$$

$$E\{\Theta_i \Theta_j\} = \begin{cases} E\{\Theta_i\} E\{\Theta_j\} & \text{if } i \neq j, \qquad (3.11) \\ E\{\Theta_i^2\} & \text{if } i = j, \qquad (3.12) \end{cases}$$

and

$$E\{\cos(\phi_i - \phi_j)\} = \delta_{ij}, \qquad (3.13)$$

where δ_{ij} is the Kronecker delta function. Therefore, Eq. 3.8 becomes

$$E\{R_n^2\} = \sum_{i=1}^{n} \sum_{j=1}^{n} E\{\lambda_i \lambda_j\} \sum_{k=1}^{\min(i,j)} E\{\Theta_k^2\} , \qquad (3.14)$$

where min(i,j) means that the minimum of the pair (i,j) is to be used to terminate the series.

In order to write $E\{\lambda_i\lambda_j\}$ as $E\{\lambda_i\}E\{\lambda_j\}$, this sum must be broken into two sums in which the first one does not allow i = j and the second contains all of the other terms. If i and j are reversed in Eq. 3.14 the resultant sum is then

identical to the initial sum; therefore, Eq. 3.14 can be rewritten as

$$E\{R_n^2\} = 2 \sum_{i=2}^{n} \sum_{j=1}^{i-1} E\{\lambda_i \lambda_j\} \sum_{k=1}^{j} E\{\Theta_k^2\} + \sum_{i=1}^{n} E\{\lambda_i^2\} \sum_{k=1}^{i} E\{\Theta_k^2\} , \quad (3.15)$$

which, because $i \neq j$ in the first sum, can be rewritten as

$$E\{R_n^2\} = 2 \sum_{i=2}^{n} \sum_{j=1}^{i-1} \bar{\lambda}_i \bar{\lambda}_j \sum_{k=1}^{j} \bar{\Theta}_k^2 + \sum_{i=1}^{n} \bar{\lambda}_i^2 \sum_{k=1}^{i} \bar{\Theta}_k^2 , \quad (3.16)$$

where the overbar designates the expected value of the variable for brevity.

The calculation of the expected value of the scattering angle in a laboratory frame of reference cannot be completed because the probability density function has not been determined for that variable. However, the probability density function of the scattering angle in the center-of-mass frame has been determined in appendix B. Hence, the variable of integration can be changed to the center-of-mass frame angle in order to complete the integration. From Eq. 2.12 of chapter 2 the scattering angle Θ in the laboratory frame can be written as

$$\Theta = 2\theta/3 \quad (3.17)$$

in the small-angle approximation, where θ is the angle of scattering in the center-of-mass frame.

A relationship between $E\{\lambda^2\}$ and $E\{\lambda\}$ would also simplify the summation in Eq. 3.16. In appendix D it was found that

$$E\{\lambda^2\} = 2\, E^2\{\lambda\} \quad (3.18)$$

is a very good approximation for almost all of the examples considered in this work. The substitution of equations 3.17 and 3.18 into equation 3.16 then yields

$$E\{R_n^2\} = \frac{8}{9}\left[\sum_{i=2}^{n} \bar{\lambda}_i \sum_{j=1}^{i-1} \bar{\lambda}_j \sum_{k=1}^{j} \bar{\theta}_k^2 + \sum_{i=1}^{n} \bar{\lambda}_i^2 \sum_{k=1}^{i} \bar{\theta}_k^2 \right] , \quad (3.19)$$

where $\bar{\lambda}$ and $\bar{\theta}^2$ must be determined from the physics of the collision process.

The expected value of the free path length calculated in appendix D is

$$E\{\lambda\} = \bar{\lambda} = 1/NQ, \quad (3.20)$$

where Q is a function of the ion energy and N is a function of penetration depth. In appendix E it is shown that the expected value of the square of the scattering angle θ is given approximately but accurately by

$$E\{\theta^2\} = \bar{\theta}^2 = \frac{12}{7E_x} \ln(2.01E_x), \quad (3.21)$$

where $E_x = m_p E_p / m_0 E_0$ for this study.

If the density of the scattering medium and the energy of the ion are now constant, then it is apparent from Eqs. 3.20 and 3.21 that $\bar{\lambda}$ and $\bar{\theta}^2$ are also constant. Therefore, Eq. 3.19 can be written as

$$E\{R_n^2\} = \frac{8}{9}\bar{\lambda}^2\bar{\theta}^2\left[\sum_{i=2}^{n}\sum_{j=1}^{i-1}\sum_{k=1}^{j} 1 + \sum_{i=1}^{n}\sum_{k=1}^{i} 1\right], \quad (3.22)$$

which reduces to

$$E\{R_n^2\} = (4/27)n(n+1)(n+2)\bar{\lambda}^2\bar{\theta}^2. \quad (3.23)$$

For large values of n, Eq. 3.23 can be approximated as

$$E\{R_n^2\} = (4/27)\bar{\lambda}^2\bar{\theta}^2 n^3, \quad (3.24)$$

which in terms of the distance y is

$$E\{R_n^2\} = (4/27)\frac{\bar{\theta}^2}{\bar{\lambda}}y^3, \quad (3.25)$$

because $n = y/\bar{\lambda}$. The substitution of Eqs. 3.20 and 3.21 yields

$$E\{R^2\} = \frac{64}{243}\pi a_0^2 E_0^2 \ln\left(2.01\frac{m_p E_p}{m_0 E_0}\right)\frac{N}{E_p^2}y^3, \quad (3.26)$$

where the definition of E_x has been used. In this equation E_p is in eV, N is in atoms/cm^3, and y is in cm. Note that the square root of Eq. 3.26,

$$\sqrt{E\{R^2\}_n} = \sqrt{\frac{64}{243}\pi a_0^2 E_0^2 \ln\left(2.01\frac{m_p E_p}{m_0 E_0}\right)}\sqrt{N}\; y^{1.5}/E_p, \quad (3.27)$$

has a functional form similar to the empirical formula developed in chapter 2 (see Eq. 2.34), if the logarithmic term which varies slowly with energy is considered to be constant. Thus, it is seen that the proton energy and scattering density dependence is the same as that for the empirical scaling law. However, the penetration depth dependence is now to the 1.5 power instead of 1.5504. The analytically predicted 1.5 is smaller than the empirically predicted value because of the small angle approximations introduced by Eq. 3.3. This approximation means that the ion is always travelling in the forward or y direction immediately prior to a collision which, of course, is not exactly true. However, this approximation neglects only the second and higher order corrections as indicated by the small discrepancy between the empirically determined power and the analytically predicted one (3.4 percent).

The evaluation of Eq. 3.19 for more complex examples in which the scattering density and ion energy both vary becomes more involved because $\bar{\lambda}$ and $\bar{\theta}^2$ are no longer constants. In order to accommodate variations in energy and density, consider Eq. 3.19. Multiply each sum by unity, or equivalently Δi, Δj, or Δk, that is,

$$E\{R_n^2\} = \frac{8}{9}\left[\sum_{i=2}^{n}\bar{\lambda}_i\Delta i\sum_{j=1}^{i-1}\bar{\lambda}_j\Delta j\sum_{k=1}^{j}\bar{\theta}_k^2\Delta k + \sum_{i=1}^{n}\bar{\lambda}_i^2\Delta i\sum_{k=1}^{i}\bar{\theta}_k^2\Delta k\right]. \quad (3.28)$$

Because $\bar{\lambda}$ is the average step size, $\bar{\lambda}_i \Delta i$ is just the average distance travelled between collisions or $\bar{\lambda}_i \Delta i = \Delta y_i$. Therefore, Eq. 3.28 can be written as

$$E\{R_n^2\} = \frac{8}{9}\left[\sum_{i=2}^{n} \Delta y_i \sum_{j=1}^{i-1} \Delta y_j \sum_{k=1}^{j} \frac{\bar{\theta}_k^2}{\bar{\lambda}_k} \Delta y_k + \sum_{i=1}^{n} \lambda_i \Delta y_i \sum_{k=1}^{i} \frac{\bar{\theta}_k^2}{\bar{\lambda}_k} \Delta y_k \right]. \quad (3.29)$$

In this equation the sums can be approximated by the integrals to obtain the following more convenient expression,

$$E\{R^2\} = \frac{8}{9}\left[\int_0^{y_n} dy_1 \int_0^{y_1} dy_2 \int_0^{y_2} \frac{\bar{\theta}_3^2}{\bar{\lambda}_3} dy_3 + \int_0^{y_n} \bar{\lambda}_1 dy_1 \int_0^{y_1} \frac{\bar{\theta}_2^2}{\bar{\lambda}_3} dy_2 \right], \quad (3.30)$$

where $\bar{\theta}^2$ and $\bar{\lambda}$ are functions of both the energy of the ion and its penetration depth. If for the moment the ion energy and the scattering density are kept constant, the integrals can then be evaluated with little effort. For large values of y

$$E\{R^2\} = \frac{4}{27} \frac{\bar{\theta}^2}{\bar{\lambda}} y^3 \quad (3.31)$$

which is of the same form as that obtained from the sum (see Eq. 3.25). This illustrates the validity of this procedure.

For the case of changing proton energy and scattering density, it is now necessary to obtain either of the variables y (penetration depth) or E_p (proton energy) as a function of the other variable, in order to complete the integration. Because of the particular choice of range-energy relationship used in this study (see section 2.4 of chapter 2), it is most convenient to change the variable of integration to E_p, instead of y. This is done through Eq. 2.17,

$$\varepsilon = -\frac{1}{N} \frac{dE}{dy}, \quad (3.32)$$

where ε is the stopping cross section and is given by

$$\frac{1}{\varepsilon} = \left(\frac{a_0}{\sqrt{E}} + a_1 + a_2\sqrt{E} + a_3 E \right) x10^{21} \ (cm^2\text{-MeV})^{-1}. \quad (3.33)$$

The coefficients of this equation are given in section 2.4 of chapter 2. This equation, when integrated, yields y as a function of E_p,

$$\int_0^y N \, dy = -\int_{E_{in}}^{E} \frac{1}{\varepsilon} dE, \quad (3.34)$$

where $E_{p_{in}}$ or simply E_{in} is the initial energy of the ion at y = 0 and E is the energy of the ion at the the distance y.

Equation 3.32 can be used to rewrite Eq. 3.30 as

$$E\{R^2\} = \frac{8}{9}\left[-\int_{E_{in}}^{E_n} \frac{dE_1}{N_1\varepsilon_1} \int_{E_{in}}^{E_1} \frac{dE_2}{N_2\varepsilon_2} \int_{E_{in}}^{E_2} \frac{\bar{\theta}_3^2}{\bar{\lambda}_3} \frac{dE_3}{N_3\varepsilon_3} + \int_{E_{in}}^{E_n} \bar{\lambda}_1 \frac{dE_1}{N_1\varepsilon_1} \int_{E_{in}}^{E_1} \frac{\bar{\theta}_2^2}{\bar{\lambda}_2} \frac{dE_2}{N_2\varepsilon_2} \right] . \quad (3.35)$$

If the expressions for N, ε, $\bar{\lambda}$, and $\bar{\theta}^2$ are used, this equation becomes

$$E\{R^2\} = -\frac{128}{81}\pi a_0^2 \left(\frac{E_0}{N_0}\right)^2 x10^{51} \int_{E_{in}}^{E_n} \left[\frac{a_0}{\sqrt{E_1}} + a_1 + a_2\sqrt{E_1} + a_3E_1 \right] \frac{dE_1}{f(y_1)} \int_{E_{in}}^{E_1} \left[\frac{a_0}{\sqrt{E_2}} + a_1 + a_2\sqrt{E_2} + a_3E_2 \right] \frac{dE_2}{f(y_2)} \int_{E_{in}}^{E_2} \ln\left(2.01x10^6 \frac{m_pE_3}{m_0E_0}\right) \left[\frac{a_0}{\sqrt{E_3}} + a_1 + a_2\sqrt{E_3} + a_3E_3 \right] \frac{dE_3}{E_3^2}$$

$$+ \frac{12}{7} \frac{m_0E_0}{m_pN_0^2} x10^{36} \int_{E_{in}}^{E_n} \left[\frac{a_0}{\sqrt{E_1}} + a_1 + a_2\sqrt{E_1} + a_3E_1 \right] \frac{E_1dE_1}{f^2(y_1)} \int_{E_{in}}^{E_1} \ln\left(2.01x10^6 \times \frac{m_pE_2}{m_0E_0}\right) \left[\frac{a_0}{\sqrt{E_2}} + a_1 + a_2\sqrt{E_2} + a_3E_2 \right] \frac{dE_2}{E_2^2} , \quad (3.36)$$

where

$$N = N_0 f(y) \quad (3.37)$$

and y is determined from Eq. 3.34. This is the general result for all examples in which the energy of the proton is attenuated in gaseous molecular hydrogen.

This completes the analysis for the scaling law and now examples of its use can be illustrated. The integral expression of Eq. 3.36 can be evaluated analytically for only a few particularly simple scattering density variations and, therefore, a computer program was developed for the numerical integration of Eq. 3.36 by means of a simple rectangular integration. The listing of this computer program is given in appendix F.

3.3 Analytical results and discussion

Results in this section will provide an evaluation of the usefulness of the analytical scaling law for a few specific examples. The predicted results will be compared to those generated by the Monte Carlo simulation for the same examples as presented in chapter 2. As done in chapter 2, all of the following examples will consider the ion to be a proton and the scattering medium to be gaseous molecular hydrogen.

Example 1: Constant scattering density and constant proton energy

For this example, the integral equation can be avoided and the sum can be evaluated directly as in Eq. 3.27. A comparison of the values obtained from Eq. 3.27 and the RMS values of the Monte Carlo distributions is given in the following table for the particular example of E_p = 10 Mev and $N_0 = 5.0946 \times 10^{19}$ atoms/cm^3 (1 atm, 288 K).

n	RMS Value of R		Ratio b/a
	a) Monte Carlo (cm)	b) Equation 3.27 (cm)	
100	4.0596×10^{-3}	5.5117×10^{-3}	1.358
200	1.1552×10^{-2}	1.5590×10^{-2}	1.350
500	4.5707×10^{-2}	6.1264×10^{-2}	1.348
1000	0.126708	0.174299	1.376
2000	0.392987	0.492993	1.254
3000	0.791042	0.905686	1.145
4000	1.23834	1.394395	1.126
5000	1.74799	1.948727	1.115

As can be seen from this table, the Monte Carlo predictions for the RMS values correspond well with the analytically predicted ones. The deviations that are present could be due to either the approximations that are used in the development of Eqs. 3.27 and 3.36 or the statistics employed in the Monte Carlo simulation. The approximations employed in the development of Eqs. 3.27 and 3.36 are believed to be very reasonable for the problems considered in this study. Therefore, it is assumed that the variations in the tabulated values arise from the use of an insufficient number of statistics in the Monte Carlo simulation. The evidence that supports this assumption is partly contained in the tabulated results. As the penetration depth increases the number of statistics involved in the Monte Carlo simulation increases, and thus the two predictions should come closer together, as in fact occurs in the tabulated values.

Note that the one-sided trend in the ratio b/a, that is, the trend of the Monte Carlo prediction to be always smaller than the analytical prediction, should not be expected. They could have been larger or intermixed. If a single large angle scattering event occurs in the Monte Carlo simulation in the first few collisions, then this ion path will drift substantially from the ion beam axis, and the subsequent Monte Carlo prediction for the RMS value of the cumulative probability distribution can be increased markedly if there are an insufficient number of statistics. In this case the Monte Carlo RMS value will

be larger than the analytical prediction. However, if a large angle collision occurs after the ion has travelled most of the distance to the target plane, then the ion will not have a chance to drift significantly from the beam axis, and the subsequent Monte Carlo prediction of the RMS value can be much smaller than the analytical result. Thus, the observed one-sidedness in the ratio b/a should not be expected. However, the tendency of the ratio to approach unity, as the distance and collision statistics increase, demonstrates that the analytical scaling law is both valid and very useful for prediction purposes.

A similar table was also completed for the Monte Carlo simulation in which each target plane distribution was generated by employing an equal number of statistics. These results are given below.

n	RMS Value of R		Ratio b/a
	a) Monte Carlo (cm)	b) Equation 3.27 (cm)	
100	-	-	-
200	1.2310×10^{-2}	1.5590×10^{-2}	1.267
500	4.7543×10^{-2}	6.1264×10^{-2}	1.289
1000	0.202046	0.174299	0.863
2000	0.576236	0.492993	0.856
3000	1.096830	0.905686	0.826
4000	1.39292	1.394395	1.001
5000	1.74799	1.948727	1.115

This data shows explicitly that any one-sidedness of the ratio b/a should not be expected. The ratio starts initially above unity, increases, abruptly drops below unity and finally increases again. This indicates that the random fluctuations above and below unity depend on the occurrence of large angle scattering events in the case of insufficient statistics.

In order to gain additional insight into the effect of the randomness of the Monte Carlo simulation on the ratio b/a, the analysis was completed for the 12 different Monte Carlo experiments obtained with equistatistics, as just considered. The raw data from the 200 mean free paths target plane was broken into 12 consecutive simulations, each of 1000 proton paths. The RMS values of these 12 separate simulations are compared to the RMS value predicted by Eq. 3.27 for that target plane in the table at the top of the next page.

Experiment Number	RMS Value of R		Ratio b/a
	a) Monte Carlo (cm)	b) Equation 3.27 (cm)	
1	1.1511×10^{-2}	1.5590×10^{-2}	1.354
2	1.0998×10^{-2}	1.5590×10^{-2}	1.418
3	1.0462×10^{-2}	1.5590×10^{-2}	1.490
4	1.1703×10^{-2}	1.5590×10^{-2}	1.332
5	1.1200×10^{-2}	1.5590×10^{-2}	1.392
6	1.3974×10^{-2}	1.5590×10^{-2}	1.116
7	1.2192×10^{-2}	1.5590×10^{-2}	1.279
8	1.8926×10^{-2}	1.5590×10^{-2}	0.824
9	1.0560×10^{-2}	1.5590×10^{-2}	1.476
10	1.0662×10^{-2}	1.5590×10^{-2}	1.462
11	1.2155×10^{-2}	1.5590×10^{-2}	1.283
12	1.1128×10^{-2}	1.5590×10^{-2}	1.401

As can be seen from these results, the randomness introduced into the ratio b/a by the Monte Carlo simulation can be fairly considerable (up to 50 percent). The effect of large angle scattering events is clearly visible in the data for the eighth simulation where the ratio is suddenly less than unity. Therefore, it will be assumed that a ratio within 30 to 40 percent of unity has to be acceptable for Monte Carlo simulations which use an insufficient number of collision statistics.

It should be noted that additional results were also obtained for the following two cases:

a) E_p = 10 MeV, $N_0 = 5.0946 \times 10^{18}$ atoms/cm^3,

b) E_p = 0.01 MeV, $N_0 = 5.0946 \times 10^{19}$ atoms/cm^3.

However, because these results are very similar to those already presented, they will not be given here.

It is worth mentioning here that the shape of the extended tail of the cumulative probability distribution can be established correctly by the Monte Carlo simulation only if a very large number of collision statistics are used. Because this is not possible in the present work, the shape of the extended tail is not well established. If a few large angle collisions occur in the Monte Carlo simulation, the tail can be greatly extended compared to the case when such collisions do not occur. Yet, the extended tail shape has a strong

effect on the RMS value of the Monte Carlo generated distributions. For example, a slightly longer or shorter extended tail can result in significantly different RMS values. This is believed to be the main reason for the large fluctuations in the b/a ratios from the value of unity.

Example 2: Constant scattering density and varying proton energy

Consider the case where the density of the hydrogen gas is constant at one atmosphere and 288 K [example 2 of chapter 2]. In this second example, because f(y) = 1, Eq. 3.36 can be integrated analytically, but because the result would contain more than 500 terms, Eq. 3.36 was integrated numerically instead. The results of the numerical integration and the corresponding ones from the Monte Carlo simulation are given for comparison in the following table.

	RMS Value of R		Ratio b/a
n	a) Monte Carlo	b) Equation 3.27	
100	4.24791×10^{-3}	5.480688×10^{-3}	1.290
200	1.18467×10^{-2}	1.561096×10^{-2}	1.318
500	4.47677×10^{-2}	6.223572×10^{-2}	1.390
1000	0.123349	0.1776375	1.440
2000	0.34947	0.5130061	1.468
3000	0.671193	0.9646772	1.437
4000	1.11802	1.523882	1.363
5000	1.7705	2.194779	1.240

The Monte Carlo generated RMS values agree fairly well with the analytically predicted values for this example. The ratio b/a again illustrates a one-sided behaviour but starts small and increases initially and then decreases. This is again believed to be due to the use of an insufficient number of statistics in the Monte Carlo simulation. However, in spite of this, the results again show that the scaling law is both valid and very useful for prediction purposes.

Example 3: Linearly increasing scattering density and varying proton energy

Consider a linearly varying density $N = N_0(1 + by)$, for which the density doubles after 500 initial mean free paths, that is, $b = 1/(500\bar{\lambda}_c)$ [example 3 of chapter 2]. The results of the numerical integration of Eq. 3.36 and the corresponding RMS values obtained from the Monte Carlo simulation are given for comparison in the table at the top of the next page.

n	RMS Value of R		Ratio b/a
	a) Monte Carlo (cm)	b) Equation 3.27 (cm)	
100	4.08585×10^{-3}	5.588494×10^{-3}	1.368
200	1.35302×10^{-2}	1.636196×10^{-2}	1.209
400	4.08866×10^{-2}	4.873529×10^{-2}	1.192
600	7.95496×10^{-2}	9.380299×10^{-2}	1.179
800	0.129323	0.1512783	1.170
1000	0.200466	0.2209936	1.102
1200	0.286931	0.3035977	1.058

These results are similar to those in examples 1 and 2, and the same conclusions can be made here.

Example 4: Linearly decreasing scattering density and varying proton energy

Consider a linearly varying density $N = N_0(1 - by)$, for which the density of the scattering medium is zero after 5000 initial mean free paths, that is, $b = 1/(5000\,\bar{\lambda}_c)$ [example 4 of chapter 2]. The results of both the numerical integration of Eq. 3.36 and the Monte Carlo simulation are given for comparison in the following table.

n	RMS Value of R		b/a
	a) Monte Carlo (cm)	b) Equation 3.27 (cm)	
100	3.69596×10^{-3}	5.354520×10^{-3}	1.449
200	1.11969×10^{-2}	1.540136×10^{-2}	1.376
500	4.45387×10^{-2}	6.104793×10^{-2}	1.370
1000	0.126246	0.172198	1.364
2000	0.362576	0.4830323	1.332
3000	0.673682	0.8740876	1.297
4000	1.03337	1.318215	1.276
4500	1.24277	1.550105	1.247

The agreement between the Monte Carlo simulation and analytical results for this example are not as good as the previous ones, simply because fewer collisions are being considered in this example. However, the agreement becomes better as the ion travels away from the source. If more ions had been considered the agreement would have been even better. These results still demonstrate that the analytical prediction is valid and very useful.

Example 5: Exponentially increasing gas density and varying proton energy

Consider an exponentially increasing density $N = N_0 \exp[a(y-b)]$, for which $a = 1/(1000\bar{\lambda}_c)$ and $b = 3000\bar{\lambda}_c$ [example 5 of chapter 2]. The results of both the numerical integration of Eq. 3.36 and the Monte Carlo simulation are given for comparison in the following table.

n	RMS Value of R		Ratio b/a
	a) Monte Carlo (cm)	b) Equation 3.27 (cm)	
1000	3.16963×10^{-2}	4.457416×10^{-2}	1.406
2000	0.106099	0.1486396	1.401
2500	0.164324	0.2271026	1.382
3000	0.241806	0.328882	1.360
3200	0.278902	0.377661	1.354
3500	0.357009	0.4613879	1.292
3800	0.457883	0.5597499	1.222
4000	0.535488	0.6350828	1.186
4200	0.620556	0.7199342	1.160

The agreement again becomes better as the penetration depth increases. This is due to the rapidly increasing number of collisions required to get from one target plane to the next. To get to the target plane for which n = 1000 only requires approximately 100 collisions, but to get to the target plane for which n = 4200 requires approximately 6000 collisions. This is due to the rapidly increasing density variation. Again, the results demonstrate the validity and usefulness of the analytical scaling law.

Example 6: Exponentially decreasing gas density and varying proton energy

Consider an exponentially decreasing density $N = N_0 \exp[-a(y-b)]$, for which $a = 1/(1000\bar{\lambda}_c)$ and $b = 1200\bar{\lambda}_c$ [example 6 of chapter 2]. The results of the numerical integration of Eq. 3.36 and the corresponding results from the Monte

Carlo simulation are given for comparison in the following table.

n	RMS Value of R		Ratio b/a
	a) Monte Carlo (cm)	b) Equation 3.27 (cm)	
100	9.52554×10^{-3}	9.869345×10^{-3}	1.036
200	3.92642×10^{-2}	2.793061×10^{-2}	0.711
400	0.106571	0.0780439	0.732
800	0.258179	0.214970	0.833
1000	0.340397	0.296263	0.870
1500	0.562593	0.525185	0.933
2000	0.803433	0.779900	0.971
3000	1.32076	1.328994	1.006
4000	1.8644	1.901423	1.020
5000	2.42034	2.427491	1.003

The agreement in this example is not good at the target planes closest to the point source, but is very good for those farther from the source. Note that the ratio b/a starts very close to unity and then drops. This effect is slowly washed out as the number of collisions increases from one target plane to the next. These results illustrate that the ratio can again fluctuate about unity, but they eventually approach unity as the number of statistics increase in the Monte Carlo simulation. In spite of this, these results are another good illustration of the validity and usefulness of the analytical scaling law.

Example 7: Free-jet expansion scattering density and varying proton energy

Consider the free-jet expansion scattering density profile simulated in example 7 of chapter 2. The results of the numerical integration of Eq. 3.36 and the corresponding results from the Monte Carlo simulation are given for comparison in the following table.

n	RMS Value of R		Ratio b/a
	a) Monte Carlo (cm)	b) Equation 3.27 (cm)	
100	0.236779	0.219731	0.928

The agreement for this example is good and is another good illustration of the validity and usefulness of the analytical scaling law.

3.4 Conclusions

The approximate analytical method presented in this chapter predicts very satisfactorily the RMS value of the cumulative probability distribution for the lateral dispersion of a point-source proton beam in molecular hydrogen. The agreement between the Monte Carlo generated data and the analytically predicted values is acceptable, considering that the discrepancy is due mainly to the limited number of ion paths that can be followed in the Monte Carlo simluation. The most practical reason for using the analytical method is the speed and reduced cost in which predicted values can be obtained. Typical Monte Carlo computer runs consume 2 hours of CPU time whereas the numerical integration of Eq. 3.36 is done in less than 1 minute of CPU time, resulting in a two-order-of-magnitude reduction in computational effort.

4.0 EXTENSION OF THE POINT-SOURCE RESULTS TO A FINITE BEAM

All of the previous work dealt strictly with a unidirectional point-source beam of monoenergetic ions travelling through a gaseous scattering medium. The results of chapters 2 and 3 for the point source can now be used with some additional analysis to yield results for a finite-sized ion beam. The analysis is first developed in general for a finite beam of nonuniform area $A_0(x,z)$ over which the ion intensity $I_0(x,z)$ and energy $E_0(x,z)$ can be initially nonuniform. Then, this general analysis is reduced to give results for the interesting specific case of a cylindrical unidirectional beam of monoenergetic ions having a uniform intensity. Some graphical results are also presented in this chapter to demonstrate application.

The Monte Carlo simulations of chapter 2 provided the reference cumulative probability distribution denoted as $P(R)$ for a unidirectional point source of monoenergetic ions at $y = 0$ and $R = 0$. The results in chapter 3 demonstrated that such a reference distribution can be suitably warped by using the scaling law to provide the cumulative probability distribution at $y = y_1$ for virtually any desired density variation with distance. This distribution can now be used in the following manner to calculate the intensity $I(R)$ in particles per unit area per unit time for an entire finite-sized beam.

For a unidirectional point source of monoenergetic ions, the lateral dispersion of the resulting ion beam as it passes through a scattering medium is axisymmetric. In this case the number of ions M per unit time passing a target plane at distance y from the point source and within a radius R of the beam axis is given by

$$M = \bar{M}\, P(R), \tag{4.1}$$

where $\bar{M}$ is the total number of ions per unit time emitted by the point source and $P(R)$ is the cumulative probability distribution. The resulting ion intensity $I(R)$ at the radius R in units of ions per unit area per unit time at the target plane is, therefore,

$$I(R)\, 2\pi R\, dR = dM. \tag{4.2}$$

The combination of Eqs. 4.1 and 4.2 then gives

$$I(R) = \frac{\bar{M}}{2\pi R} \frac{dP(R)}{dR} \tag{4.3}$$

for this case of a point source.

For the case of a finite-sized beam which can be considered to consist of an infinite number of point sources, Eq. 4.3 can now generalized to

$$dI(X,y,Z) = \frac{I_0(x,z)}{2\pi R'} \frac{dP[R',y,E_0(x,z)]}{dR'} dx\,dz\,. \tag{4.4}$$

In this expression $dI(X,y,Z)$ is the resulting differential ion intensity at the position (X, y, Z) in the target plane from a point source or sources in the elemental area dxdz located at position (x, 0, z) in the source plane (see Fig. 37). This point source has an initial intensity $I_0(x,z)$ and initial energy $E_0(x,z)$, which are not considered here as constant over the initial beam area $A(x,z)$. Also, $R' = [(X - x)^2 + (Z - z)^2]^{0.5}$ is the lateral separation distance in the (X,Z) plane (see Fig. 37).

In order to calculate the total beam intensity $I(X,y,Z)$ in ions per unit area per unit time at the point [X, y, Z] due to all of the point sources within a beam of initial cross sectional area $A_0(x,z)$, Eq. 4.4 must then be integrated over the entire initial area of the beam, giving

$$I(X,y,Z) = \iint_{(x,z)} \frac{I_0(x,z)}{2\pi R'} \frac{dP[R',y,E_0(x,z)]}{dR'} dx\,dz\,. \tag{4.5}$$

This is the general equation for the intensity distribution in the (X,Z) plane at a distance y for a finite-sized beam that has an area $A_0(x,z)$ in the (x,z) plane and passes through a scattering medium. This expression would in general have to be integrated numerically to yield $I(X,y,Z)$.

The reduced or special case of a constant intensity, cylindrical, unidirectional beam of monoenergetic ions will now be considered. Although this special case is rather simple, the results are still of practical importance. For this basic case, $I(X,y,Z)$ can be evaluated through the use of Eq. 4.5, by setting $I_0(x,z) = I_0$, $E_0(x,z) = E_0$, and $A_0(x,z)$ be the area of a circular beam of radius R_0. Equation 4.5 can now be written as

$$I(X,y,Z) = \iint_{(x,z)} \frac{I_0}{2\pi R'} \frac{dP(R',y,E_0)}{dR'} dx\,dz\,. \tag{4.6}$$

In this expression the cumulative probability distribution $P(R',y,E_0)$ can be obtained in digital form from table 2 or as a smooth analytical function from Eq. 2.36, which was fitted to the digital data. This analytical function is repeated here for convenience,

$$P(R',y,E_0) = \frac{1}{2}\left[1 - \exp\left(-\mathcal{L}n(2)\left[\frac{R'}{R^*(y,E_0)}\right]^2\right)\right] + \frac{1}{\pi}\mathrm{Arctan}\left[\frac{R'}{R^*(y,E_0)}\right]^2, \tag{4.7}$$

where $P[R^*(y,E_0),y,E_0] = 0.5$. Therefore, the derivative of $P(R',y,E_0)$ is

simply

$$\frac{dP(R')}{dR'} = \ln(2)\frac{R'}{R^*(y,E_0)} \exp\left[-\ln(2)\left[\frac{R'}{R^*(y,E_0)}\right]^2\right] + \frac{2}{\pi}\frac{R'}{R^*(y,E_0)} \frac{1}{1+\left[\frac{R'}{R^*(y,E_0)}\right]^4}. \tag{4.8}$$

Because of the cylindrical symmetry of this example it is best to change the variables of integration from x and z to R′ and η. Substitution of this information into Eq. 4.6 gives

$$I(R,y) = \int_{R'_{min}}^{R'_{max}} \int_{\eta_{min}}^{\eta_{max}} \frac{I_0}{2\pi}\frac{dP(R',y,E_0)}{dR'}\, d\eta\, dR' \tag{4.9}$$

for the intensity I(R,y) in ions per unit area per unit time at the radius R from the beam axis due to the entire beam.

In order to evaluate this integral, three geometries must now be considered, and they are shown in Fig. 38. The first geometry involves only the case when $R > R_0$, whereas the second and third cases consider $R < R_0$ but distinguish between $R > R_0 - R'$ and $R < R_0 - R'$. If R is greater than R_0 then

$$R_{min} = R - R_0, \tag{4.10}$$

$$R_{max} = R + R_0, \tag{4.11}$$

and

$$\eta_{max} = \text{Arccos}\left[\frac{R'^2 + R^2 - R_0^2}{2R'R}\right], \tag{4.12}$$

and, hence,

$$I(R,y) = \frac{I_0}{\pi}\int_{R-R_0}^{R+R_0} \text{Arccos}\left[\frac{R'^2 + R^2 - R_0^2}{2R'R}\right] \frac{dP(R',y,E_0)}{dR'}\, dR'. \tag{4.13}$$

If R is less than R_0 and $R + R'$ is greater than R_0, then

$$R_{min} = R_0 - R, \tag{4.14}$$

$$R_{max} = R_0 + R, \tag{4.15}$$

and

$$\eta_{max} = \text{Arccos}\left[\frac{R'^2 + R^2 - R_0^2}{2R'R}\right] \tag{4.16}$$

again. Therefore,

$$I(R,y) = \frac{I_0}{\pi} \int_{R_0 - R}^{R_0 + R} \text{Arccos}\left[\frac{R'^2 + R^2 - R_0^2}{2R'R} \right] \frac{dP(R',y,E_0)}{dR'} dR' , \quad (4.17)$$

which is the same as Eq. 4.13 but with a different lower limit of integration. If R is less than R_0 but $R + R'$ is less than R_0, then

$$R_{min} = 0, \quad (4.18)$$

$$R_{max} = R_0 - R, \quad (4.19)$$

and

$$\eta_{max} = \pi. \quad (4.20)$$

Consequently,

$$I(R,y) = I_0 P(R_0 - R, y, E_0) \quad (4.21)$$

for this simplest final case.

In summary, therefore, if $R > R_0$, then

$$I(R,y) = \frac{I_0}{\pi} \int_{R - R_0}^{R + R_0} \text{Arccos}\left[\frac{R'^2 + R^2 - R_0^2}{2R'R} \right] \frac{dP(R',y,E_0)}{dR'} dR' , \quad (4.22)$$

and if $R < R_0$, then

$$I(R,y) = I_0 P(R_0 - R, y, E_0) \quad (4.23)$$

$$+ \frac{I_0}{\pi} \int_{R_0 - R}^{R_0 + R} \text{Arccos}\left[\frac{R'^2 + R^2 - R_0^2}{2R'R} \right] \frac{dP(R',y,E_0)}{dR'} dR' ,$$

where $P(R_0 - R, y, E_0)$ is obtained from Eq. 4.7 and $dP(R',y,E_0)/dR$ is obtained from Eq. 4.8. Notice that, if $R = R_0$, Eqs. 4.22 and 4.23 are then equivalent.

The value of R* in this chapter is the 50 percent point of the cumulative probability distribution of the lateral dispersion of a point source of ions scattering in gaseous molecular hydrogen. Note that R* is dependent on the penetration depth, scattering density, and initial ion energy. In chapter 3 an analytical scaling law was developed for predicting the root-mean-square (RMS) value of the cumulative probability distribution (see Eq. 3.36). It is, therefore, necessary to convert the value of R* to the RMS value of the curve. It was found that the RMS value of the reference distribution given in table 2 of chapter 2 is 5/3 larger than the 50 percent R value (R*) of the distribution. Therefore, the analytical RMS value can be calculated by using Eq. 3.36 for the particular penetration depth and density distribution desired, and then this value can be multiplied by 3/5 and then used as the R* value for the cumulative

probability distribution given by Eqs. 4.22 and 4.23. In this manner the lateral dispersion of a finite-sized ion beam can be predicted.

To illustrate some of the results from these equations, consider an initially cylindrical beam of ions of uniform intensity I_0 and energy E_0. The initial intensity distribution as a function of R at the source plane (y = 0) for this beam is shown in Fig. 39a. The probability density function for this beam can be obtained from the intensity distribution by multiplying by R, that is, $p(R) = R\ I(R)$. This distribution for the ion beam is shown in Fig. 39b. Finally, the cumulative probability distribution for this ion beam can be obtained by integrating the probability density function. For this particular beam it is found that $P(R) = (R/R_0)$ for $R < R_0$ and $P(R) = 1$ for $R > R_0$. This distribution is shown in Fig. 39c.

In order to calculate the intensity, probability density, and cumulative probability distributions, increasing values of R* can be used in Eqs. 4.22 and 4.23 and these integrals evaluated. Intuitively it is expected that the three distributions would approach those of a point source (see Fig. 6) as the R* value or the penetration depth increases. This would occur because a finite-sized ion beam would appear more and more like a point source as the distance to the target plane increases. The results given in Figs. 40, 41, and 42 illustrate how the distributions obtained from Eqs. 4.24 and 4.25 change in shape for increasing values of R*, or increasing distance from to the target plane. These figures also show that the distributions do indeed approach the corresponding shape of the point-source distributions as the distance increases.

Before leaving this chapter, it is worth mentioning that $I(R,y)$ can be obtained from Eqs. 4.22 and 4.23 by integrating with respect to either R' or $P(R',y,E_0)$. In the former case used herein a smooth curve fit to $P(R',y,E_0)$ is needed such that $dP(R',y,E_0)/dR'$ can be obtained to do the integration. In the latter case, however, a curve fit is not required and the Monte Carlo generated numerical distribution for $P(R',y,E_0)$ can be used directly in the integration. This latter integration technique has been employed in work not presented here. Its use is not necessary, but in some instances it has inherent advantages.

5.0 CONCLUDING REMARKS

The lateral dispersion of a point-source or finite-sized ion beam in a variable density scattering medium due to multiple Coulomb scattering has now been solved successfully. A Monte Carlo simulation was used first to solve this problem. The results were very expensive to produce if the tail of the distributions were generated with any precision. However, they do have the behaviour expected of both the theoretical and experimental observations. The cumulative probability distribution P(R) for the lateral dispersion of a point source beam of ions was shown to be self similar with respect to ion penetration depth, ion energy, and number density variation of the scattering medium within each example, and it was also shown to be similar from one example to the next. This similarity was not expected, but has important implications regarding other numerical solutions of such ion-beam dispersion problems.

A successful approximate analytical scaling law was developed to predict the root-mean-square value of the cumulative probability distribution. This scaling law can be used to warp the Monte Carlo generated reference cumulative probability distribution to give the solution to almost any new corresponding

ion-beam dispersion problem.

The present method of solving the problem of the lateral dispersion of a point-source or finite-sized ion beam as it traverses a scattering medium is fundamental to understanding the transport of ion beams in scattering mediums. Although the present method was illustrated by making use of the collision theory of protons scattering in gaseous molecular hydrogen, the method could easily be applied to the case of other ions scattering in other gaseous, liquid, or solid mediums.

6.0 REFERENCES

1. L. M. Lidsky and D. G. Colombant, "High Intensity 14-MeV Neutron Source", IEEE Transactions of Nuclear Science, NS-14, No. 3, pp. 945-949, 1967.

2. D. D. Armstrong, C. R. Emigh, K. L. Meier, E. A. Meyer, and J. D. Schnieder, "A 14 MeV Intense Neutron Source Facility", Nuclear Instrumentation and Methods, Vol. 145, p. 127, 1977.

3. J. H. de Leeuw, V. Chatoorgoon, J. J. Gottlieb, A. A. Haasz, and P. C. Stangeby, "Subsonic and Hypersonic Gas Target Neutron Generator Studies", Proceedings of the Second Topical Meeting on the Technology of Controlled Nuclear Fusion, American Nuclear Society, Vol. IV, pp. 1473-84, Sept. 21-23, 1976, held in Richland, Washington, D. C.

4. P. C. Stangeby and V. Chatoorgoon, "Subsonic Gas Target", Journal of Energy, Vol. 1, No. 6, pp. 387-392, November-December 1977.

5. V. Chatoorgoon and P. C. Stangeby, "Subsonic Gas Target 14 MeV Neutron Generator", Journal of Energy, Vol. 2, No. 3, pp. 129-130, May-June 1978.

6. V. Chatoorgoon, "Subsonic Gas Target 14 MeV Neutron Generator", University of Toronto Institute for Aerospace Studies Report No. 251, October 1981.

7. J. B. French, "Molecular Beams for Rarefied Gasdynamics Research", AGARDograph, pp. 112-125, 1966.

8. J. E. Robinson, "Scattering and Radiation Damage for Light keV Ions on Solid Surfaces", Radiation Effects, Vol. 23, pp. 29-36, 1974.

9. M. J. Berger, "Monte Carlo Calculation of the Penetration and Diffusion of Fast Charged Particles", Methods in Computational Physics, Vol. 1, Academic Press, 1963.

10. J. M. Hammersley and D. C. Handscomb, "Monte Carlo Methods", Halsted Press, a division of John Wiley and Sons, New York, 1975.

11. E. D. Cashwell and C. J. Everett, "The Monte Carlo Method for Random Walk Problems", Pergamon Press, 1959.

12. N. F. Mott and H. S. W. Massey, "The Theory of Atomic Collisions", third edition, Oxford at the Clarendon Press, p. 455, 1965.

13. G. Moliere, "Die Vielfachstreuung der Elektronen zu Grossen Winkeln: I Losungen fur Unendlich Ausgedehnte Medium", Z. Physik, Vol. 156, pp. 318-347, 1959.

14. S. Goudsmit and J. L. Saunderson, "Multiple Scattering of Electrons", The Physical Review, Vol. 57, pp. 24-29, January-June 1940.

15. S. Goudsmit and J. L. Saunderson, "Multiple Scattering of Electrons II", The Physical Review, Vol. 58, pp. 36-42, July-December 1940.

16. W. Whaling, "The Energy Loss of Charged Particles in Matter", Encyclopedia of Physics, Corpuscles and Radiation in Matter II, pp. 193-217, Springer-Verlag, Berlin, 1958.

17. M. J. Berger, "Multiple Scattering of Fast Protons in Photographic Emulsions", The Physical Review, Vol. 88, second series, pp. 59-70, 1952.

18. H. Ashkenas and F. S. Sherman, "The Structure and Utilization of Supersonic Free Jets", Proceedings of the Fourth International Symposium on Rarefied Gas Dynamics, Academic Press (J. H. de Leeuw, Ed.), pp. 84-105, 1964.

19. M. J. Werle, D. G. Shaffer, and R. T. Driftmyer, "Freejet Terminal Shocks", AIAA Journal, Vol. 8, No. 12, pp. 2295-2297, December 1970.

20. W. S. Young, "Derivation of the Free-Jet Mach-Disk Location using the Entropy-Balance Principle", The Physics of Fluids, Vol. 18, No. 11, pp. 1421-1425, November 1975.

TABLE 1

RANGE OF A PROTON IN MOLECULAR HYDROGEN
(at a pressure of 1 atm and a temperature of 288 K)

Proton Energy (MeV)	Calculated Range (Eq. 2.21) (cm)	Range (Whaling [16]) (cm)
0.040	0.1740	0.174
0.045	0.1898	0.190
0.050	0.2052	0.205
0.055	0.2205	0.220
0.060	0.2358	0.236
0.065	0.2510	0.251
0.070	0.2663	0.266
0.075	0.2818	0.282
0.080	0.2975	0.297
0.085	0.3134	0.313
0.090	0.3296	0.329
0.095	0.3461	0.346
0.100	0.3629	0.362
0.150	0.5508	0.551
0.200	0.7794	0.780
0.250	1.0509	1.05
0.300	1.3653	1.37
0.350	1.7220	1.73
0.400	2.1204	2.13
0.450	2.5598	2.57
0.500	3.0394	3.05
0.550	3.5586	3.57
0.600	4.1166	4.12
0.650	4.7129	4.72
0.700	5.3470	5.35
0.750	6.0183	6.02
0.800	6.7264	6.72
0.850	7.4707	7.46
0.900	8.2510	8.24
0.950	9.0668	9.06
1.000	9.9177	9.91
1.500	20.2943	20.2
2.000	33.9058	33.8
2.500	50.5874	50.6
3.000	70.2233	70.3
3.500	92.7275	92.8
4.000	118.0316	118.
4.500	146.0803	146.
5.000	176.8277	177.
5.500	210.2345	210.
6.000	246.2668	246.
6.500	284.8950	285.
7.000	326.0930	326.
7.500	369.8374	370.
8.000	416.1069	417.
8.500	464.8826	466.
9.000	516.1470	518.
9.500	569.8835	572.
10.000	626.0789	628.

TABLE 2

MONTE CARLO GENERATED CUMULATIVE PROBABILITY DISTRIBUTION P(R)
FOR THE LATERAL DISPERSION OF A PROTON BEAM IN GASEOUS MOLECULAR HYDROGEN

The values in this table are normalized so that to calculate the value of R in cm the tabulated value must be multiplied by

$$N_0^{0.5} y^{1.5505} / E_{p_{in}}$$

where N_0 is the gas density in molecules/cm^3, $E_{p_{in}}$ is the proton energy in MeV and y is the penetration depth in cm. This distribution was generated for the aphysical case of a constant energy proton and a constant scattering density.

P(r)	r	P(r)	r	P(r)	r
0.000	0.00000E+00	0.070	0.56487E-13	0.140	0.81724E-13
0.002	0.81876E-14	0.072	0.57314E-13	0.142	0.82419E-13
0.004	0.13569E-13	0.074	0.58168E-13	0.144	0.83114E-13
0.006	0.15800E-13	0.076	0.59150E-13	0.146	0.83894E-13
0.008	0.18547E-13	0.078	0.60086E-13	0.148	0.84480E-13
0.010	0.20749E-13	0.080	0.60959E-13	0.150	0.85060E-13
0.012	0.21934E-13	0.082	0.62167E-13	0.152	0.85632E-13
0.014	0.24151E-13	0.084	0.62996E-13	0.154	0.86508E-13
0.016	0.25796E-13	0.086	0.63770E-13	0.156	0.87218E-13
0.018	0.28438E-13	0.088	0.64511E-13	0.158	0.87987E-13
0.020	0.29834E-13	0.090	0.65123E-13	0.160	0.88452E-13
0.022	0.31430E-13	0.092	0.65935E-13	0.162	0.89035E-13
0.024	0.32513E-13	0.094	0.66715E-13	0.164	0.89701E-13
0.026	0.34064E-13	0.096	0.67245E-13	0.166	0.90408E-13
0.028	0.35153E-13	0.098	0.68127E-13	0.168	0.90972E-13
0.030	0.37044E-13	0.100	0.68594E-13	0.170	0.91424E-13
0.032	0.38588E-13	0.102	0.69239E-13	0.172	0.91956E-13
0.034	0.40235E-13	0.104	0.69924E-13	0.174	0.92591E-13
0.036	0.41144E-13	0.106	0.70675E-13	0.176	0.93247E-13
0.038	0.42266E-13	0.108	0.71219E-13	0.178	0.93807E-13
0.040	0.43382E-13	0.110	0.71834E-13	0.180	0.94265E-13
0.042	0.44585E-13	0.112	0.72408E-13	0.182	0.94739E-13
0.044	0.45890E-13	0.114	0.73009E-13	0.184	0.95364E-13
0.046	0.46575E-13	0.116	0.73666E-13	0.186	0.95937E-13
0.048	0.47578E-13	0.118	0.74420E-13	0.188	0.96523E-13
0.050	0.48706E-13	0.120	0.75364E-13	0.190	0.97082E-13
0.052	0.49777E-13	0.122	0.75990E-13	0.192	0.97500E-13
0.054	0.50407E-13	0.124	0.76820E-13	0.194	0.98037E-13
0.056	0.51034E-13	0.126	0.77455E-13	0.196	0.98369E-13
0.058	0.51833E-13	0.128	0.77942E-13	0.198	0.98861E-13
0.060	0.52457E-13	0.130	0.78698E-13	0.200	0.99556E-13
0.062	0.53820E-13	0.132	0.79331E-13	0.202	0.10027E-12
0.064	0.54312E-13	0.134	0.79930E-13	0.204	0.10087E-12
0.066	0.55108E-13	0.136	0.80419E-13	0.206	0.10133E-12
0.068	0.55824E-13	0.138	0.81214E-13	0.208	0.10194E-12

TABLE 2 (continued)

MONTE CARLO GENERATED CUMULATIVE PROBABILITY DISTRIBUTION P(R)
FOR THE LATERAL DISPERSION OF A PROTON BEAM IN GASEOUS MOLECULAR HYDROGEN

P(r)	r	P(r)	r	P(r)	r
0.210	0.10243E-12	0.300	0.12618E-12	0.390	0.15083E-12
0.212	0.10278E-12	0.302	0.12671E-12	0.392	0.15151E-12
0.214	0.10329E-12	0.304	0.12722E-12	0.394	0.15214E-12
0.216	0.10380E-12	0.306	0.12768E-12	0.396	0.15278E-12
0.218	0.10441E-12	0.308	0.12825E-12	0.398	0.15337E-12
0.220	0.10492E-12	0.310	0.12888E-12	0.400	0.15379E-12
0.222	0.10574E-12	0.312	0.12939E-12	0.402	0.15424E-12
0.224	0.10620E-12	0.314	0.13000E-12	0.404	0.15481E-12
0.226	0.10679E-12	0.316	0.13042E-12	0.406	0.15515E-12
0.228	0.10723E-12	0.318	0.13100E-12	0.408	0.15573E-12
0.230	0.10766E-12	0.320	0.13176E-12	0.410	0.15616E-12
0.232	0.10832E-12	0.322	0.13237E-12	0.412	0.15678E-12
0.234	0.10880E-12	0.324	0.13294E-12	0.414	0.15739E-12
0.236	0.10932E-12	0.326	0.13369E-12	0.416	0.15782E-12
0.238	0.10987E-12	0.328	0.13414E-12	0.418	0.15838E-12
0.240	0.11054E-12	0.330	0.13479E-12	0.420	0.15903E-12
0.242	0.11114E-12	0.332	0.13523E-12	0.422	0.15963E-12
0.244	0.11159E-12	0.334	0.13597E-12	0.424	0.16011E-12
0.246	0.11216E-12	0.336	0.13640E-12	0.426	0.16062E-12
0.248	0.11270E-12	0.338	0.13689E-12	0.428	0.16148E-12
0.250	0.11313E-12	0.340	0.13734E-12	0.430	0.16216E-12
0.252	0.11385E-12	0.342	0.13794E-12	0.432	0.16265E-12
0.254	0.11426E-12	0.344	0.13838E-12	0.434	0.16351E-12
0.256	0.11463E-12	0.346	0.13893E-12	0.436	0.16393E-12
0.258	0.11505E-12	0.348	0.13949E-12	0.438	0.16469E-12
0.260	0.11549E-12	0.350	0.14015E-12	0.440	0.16518E-12
0.262	0.11589E-12	0.352	0.14050E-12	0.442	0.16564E-12
0.264	0.11637E-12	0.354	0.14092E-12	0.444	0.16628E-12
0.266	0.11679E-12	0.356	0.14128E-12	0.446	0.16712E-12
0.268	0.11742E-12	0.358	0.14190E-12	0.448	0.16761E-12
0.270	0.11809E-12	0.360	0.14265E-12	0.450	0.16805E-12
0.272	0.11857E-12	0.362	0.14323E-12	0.452	0.16860E-12
0.274	0.11915E-12	0.364	0.14377E-12	0.454	0.16910E-12
0.276	0.11977E-12	0.366	0.14422E-12	0.456	0.16966E-12
0.278	0.12028E-12	0.368	0.14499E-12	0.458	0.17022E-12
0.280	0.12095E-12	0.370	0.14557E-12	0.460	0.17061E-12
0.282	0.12138E-12	0.372	0.14615E-12	0.462	0.17095E-12
0.284	0.12179E-12	0.374	0.14681E-12	0.464	0.17161E-12
0.286	0.12225E-12	0.376	0.14738E-12	0.466	0.17212E-12
0.288	0.12269E-12	0.378	0.14783E-12	0.468	0.17283E-12
0.290	0.12332E-12	0.380	0.14835E-12	0.470	0.17348E-12
0.292	0.12397E-12	0.382	0.14866E-12	0.472	0.17396E-12
0.294	0.12443E-12	0.384	0.14925E-12	0.474	0.17432E-12
0.296	0.12494E-12	0.386	0.14969E-12	0.476	0.17493E-12
0.298	0.12569E-12	0.388	0.15028E-12	0.478	0.17543E-12

TABLE 2 (continued)

MONTE CARLO GENERATED CUMULATIVE PROBABILITY DISTRIBUTION P(R)
FOR THE LATERAL DISPERSION OF A PROTON BEAM IN GASEOUS MOLECULAR HYDROGEN

P(r)	r	P(r)	r	P(r)	r
0.480	0.17624E-12	0.570	0.20278E-12	0.660	0.23325E-12
0.482	0.17671E-12	0.572	0.20355E-12	0.662	0.23416E-12
0.484	0.17728E-12	0.574	0.20422E-12	0.664	0.23517E-12
0.486	0.17790E-12	0.576	0.20486E-12	0.666	0.23596E-12
0.488	0.17853E-12	0.578	0.20547E-12	0.668	0.23682E-12
0.490	0.17906E-12	0.580	0.20618E-12	0.670	0.23759E-12
0.492	0.17972E-12	0.582	0.20670E-12	0.672	0.23864E-12
0.494	0.18062E-12	0.584	0.20748E-12	0.674	0.23944E-12
0.496	0.18109E-12	0.586	0.20800E-12	0.676	0.24035E-12
0.498	0.18174E-12	0.588	0.20871E-12	0.678	0.24099E-12
0.500	0.18237E-12	0.590	0.20956E-12	0.680	0.24162E-12
0.502	0.18287E-12	0.592	0.21025E-12	0.682	0.24251E-12
0.504	0.18332E-12	0.594	0.21107E-12	0.684	0.24318E-12
0.506	0.18407E-12	0.596	0.21166E-12	0.686	0.24400E-12
0.508	0.18461E-12	0.598	0.21221E-12	0.688	0.24485E-12
0.510	0.18518E-12	0.600	0.21277E-12	0.690	0.24569E-12
0.512	0.18572E-12	0.602	0.21360E-12	0.692	0.24619E-12
0.514	0.18640E-12	0.604	0.21426E-12	0.694	0.24677E-12
0.516	0.18722E-12	0.606	0.21509E-12	0.696	0.24775E-12
0.518	0.18776E-12	0.608	0.21579E-12	0.698	0.24856E-12
0.520	0.18841E-12	0.610	0.21677E-12	0.700	0.24905E-12
0.522	0.18908E-12	0.612	0.21758E-12	0.702	0.24947E-12
0.524	0.18964E-12	0.614	0.21824E-12	0.704	0.25033E-12
0.526	0.19009E-12	0.616	0.21874E-12	0.706	0.25114E-12
0.528	0.19064E-12	0.618	0.21924E-12	0.708	0.25188E-12
0.530	0.19116E-12	0.620	0.21990E-12	0.710	0.25257E-12
0.532	0.19169E-12	0.622	0.22048E-12	0.712	0.25360E-12
0.534	0.19235E-12	0.624	0.22102E-12	0.714	0.25448E-12
0.536	0.19290E-12	0.626	0.22169E-12	0.716	0.25526E-12
0.538	0.19337E-12	0.628	0.22231E-12	0.718	0.25606E-12
0.540	0.19417E-12	0.630	0.22299E-12	0.720	0.25700E-12
0.542	0.19470E-12	0.632	0.22371E-12	0.722	0.25791E-12
0.544	0.19520E-12	0.634	0.22458E-12	0.724	0.25883E-12
0.546	0.19564E-12	0.636	0.22541E-12	0.726	0.25992E-12
0.548	0.19612E-12	0.638	0.22590E-12	0.728	0.26095E-12
0.550	0.19653E-12	0.640	0.22640E-12	0.730	0.26169E-12
0.552	0.19710E-12	0.642	0.22720E-12	0.732	0.26254E-12
0.554	0.19765E-12	0.644	0.22781E-12	0.734	0.26332E-12
0.556	0.19831E-12	0.646	0.22843E-12	0.736	0.26402E-12
0.558	0.19877E-12	0.648	0.22903E-12	0.738	0.26499E-12
0.560	0.19934E-12	0.650	0.22969E-12	0.740	0.26573E-12
0.562	0.19992E-12	0.652	0.23034E-12	0.742	0.26682E-12
0.564	0.20054E-12	0.654	0.23125E-12	0.744	0.26763E-12
0.566	0.20117E-12	0.656	0.23198E-12	0.746	0.26857E-12
0.568	0.20196E-12	0.658	0.23275E-12	0.748	0.26946E-12

TABLE 2 (continued)

MONTE CARLO GENERATED CUMULATIVE PROBABILITY DISTRIBUTION P(R)
FOR THE LATERAL DISPERSION OF A PROTON BEAM IN GASEOUS MOLECULAR HYDROGEN

P(r)	r	P(r)	r	P(r)	r
0.750	0.27042E-12	0.834	0.31948E-12	0.918	0.40995E-12
0.752	0.27154E-12	0.836	0.32079E-12	0.920	0.41205E-12
0.754	0.27240E-12	0.838	0.32220E-12	0.922	0.41532E-12
0.756	0.27328E-12	0.840	0.32369E-12	0.924	0.41902E-12
0.758	0.27415E-12	0.842	0.32561E-12	0.926	0.42388E-12
0.760	0.27539E-12	0.844	0.32722E-12	0.928	0.42828E-12
0.762	0.27661E-12	0.846	0.32849E-12	0.930	0.43153E-12
0.764	0.27751E-12	0.848	0.33017E-12	0.932	0.43547E-12
0.766	0.27889E-12	0.850	0.33135E-12	0.934	0.44079E-12
0.768	0.28004E-12	0.852	0.33318E-12	0.936	0.44447E-12
0.770	0.28081E-12	0.854	0.33525E-12	0.938	0.44826E-12
0.772	0.28180E-12	0.856	0.33626E-12	0.940	0.45424E-12
0.774	0.28318E-12	0.858	0.33795E-12	0.942	0.45996E-12
0.776	0.28402E-12	0.860	0.33938E-12	0.944	0.46590E-12
0.778	0.28497E-12	0.862	0.34117E-12	0.946	0.46929E-12
0.780	0.28603E-12	0.864	0.34335E-12	0.948	0.47517E-12
0.782	0.28736E-12	0.866	0.34548E-12	0.950	0.48076E-12
0.784	0.28858E-12	0.868	0.34700E-12	0.952	0.48744E-12
0.786	0.28966E-12	0.870	0.34913E-12	0.954	0.49453E-12
0.788	0.29046E-12	0.872	0.35082E-12	0.956	0.49977E-12
0.790	0.29155E-12	0.874	0.35290E-12	0.958	0.50718E-12
0.792	0.29275E-12	0.876	0.35411E-12	0.960	0.51744E-12
0.794	0.29386E-12	0.878	0.35584E-12	0.962	0.52581E-12
0.796	0.29534E-12	0.880	0.35802E-12	0.964	0.53440E-12
0.798	0.29634E-12	0.882	0.36012E-12	0.966	0.54570E-12
0.800	0.29745E-12	0.884	0.36294E-12	0.968	0.55628E-12
0.802	0.29886E-12	0.886	0.36595E-12	0.970	0.56652E-12
0.804	0.29989E-12	0.888	0.36812E-12	0.972	0.58019E-12
0.806	0.30115E-12	0.890	0.37096E-12	0.974	0.59204E-12
0.808	0.30252E-12	0.892	0.37316E-12	0.976	0.61346E-12
0.810	0.30352E-12	0.894	0.37582E-12	0.978	0.64103E-12
0.812	0.30526E-12	0.896	0.37782E-12	0.980	0.66425E-12
0.814	0.30643E-12	0.898	0.38018E-12	0.982	0.68486E-12
0.816	0.30751E-12	0.900	0.38313E-12	0.984	0.71952E-12
0.818	0.30863E-12	0.902	0.38501E-12	0.986	0.77592E-12
0.820	0.30961E-12	0.904	0.38823E-12	0.988	0.82422E-12
0.822	0.31139E-12	0.906	0.39083E-12	0.990	0.91943E-12
0.824	0.31250E-12	0.908	0.39408E-12	0.992	0.10104E-11
0.826	0.31411E-12	0.910	0.39677E-12	0.994	0.11187E-11
0.828	0.31518E-12	0.912	0.39932E-12	0.996	0.12767E-11
0.830	0.31672E-12	0.914	0.40195E-12	0.998	0.16732E-11
0.832	0.31847E-12	0.916	0.40545E-12	1.000	0.12010E-10

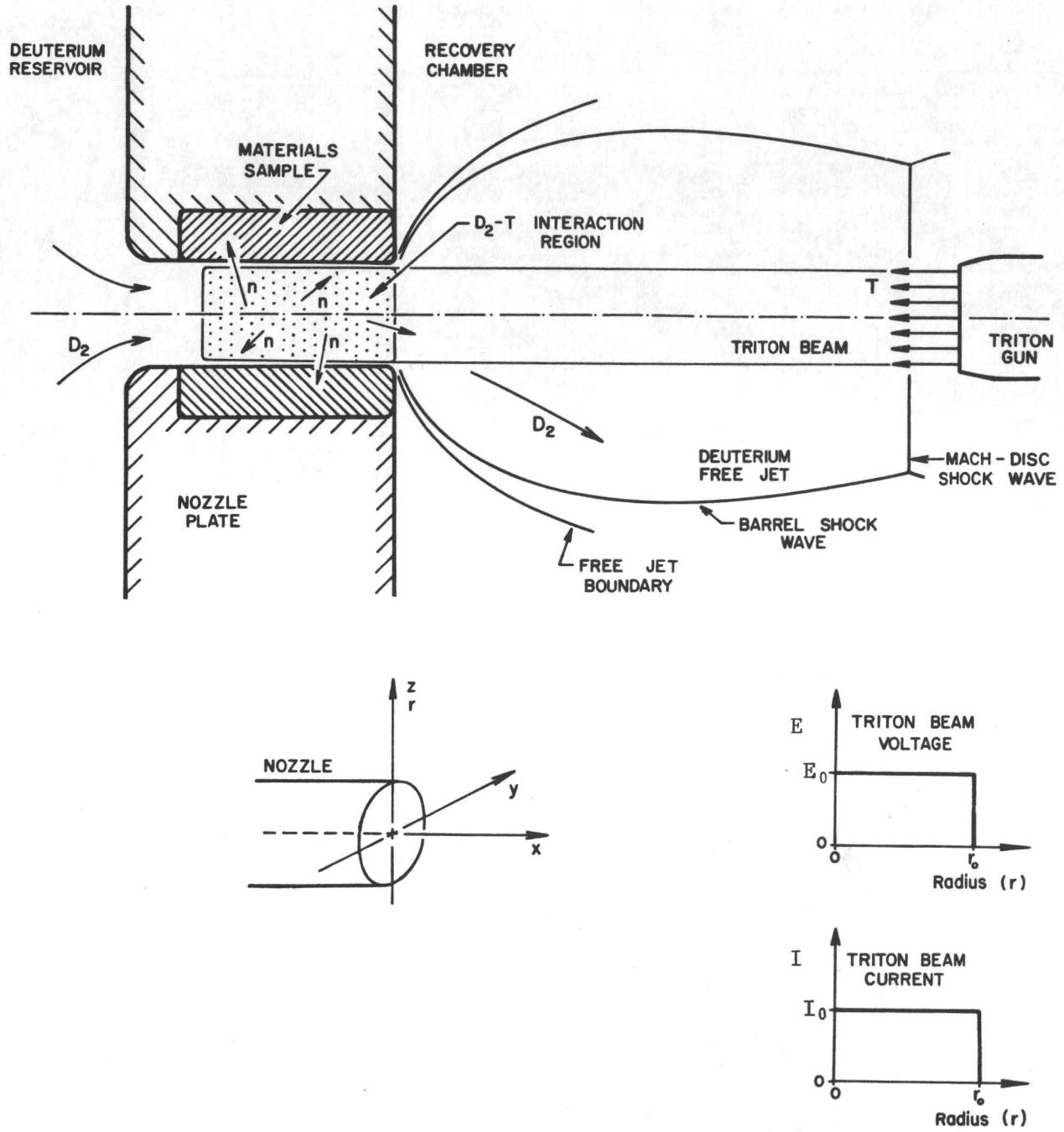

Fig. 1. Schematic diagram of a subsonic gas target neutron generator for testing materials from 14 MeV neutron bombardment [3-6].

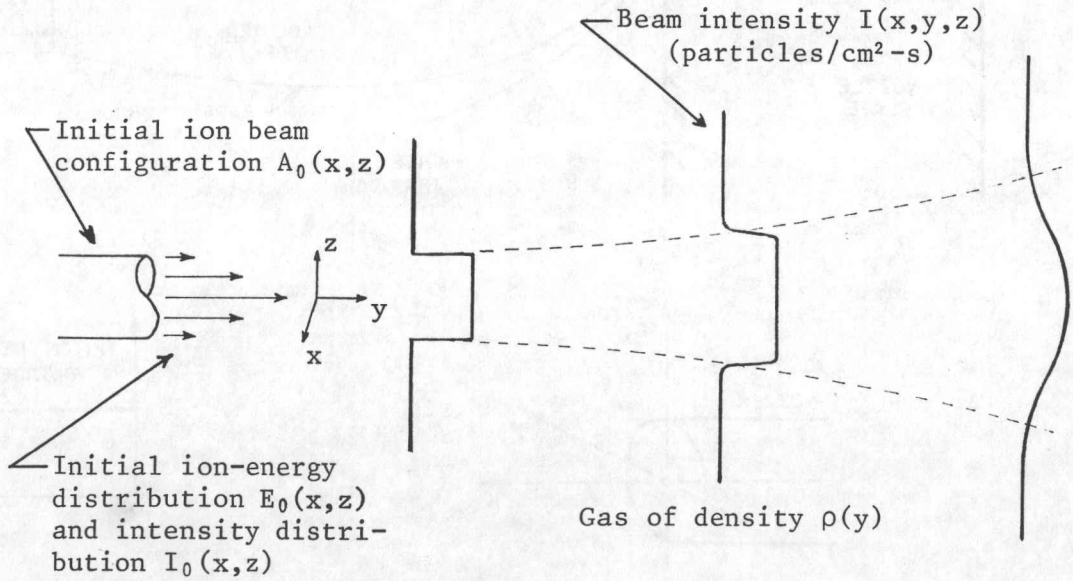

Fig. 2. Illustration of an ion beam spreading in a scattering medium of varying density.

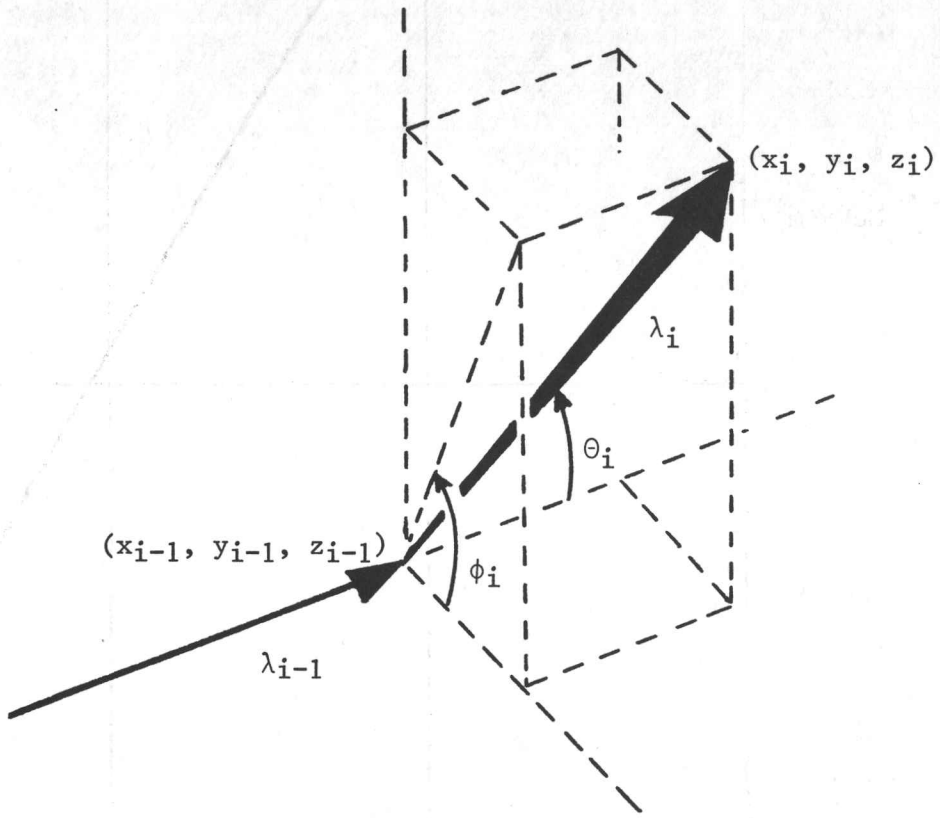

Fig. 3. Illustration of the parameters describing a collision.

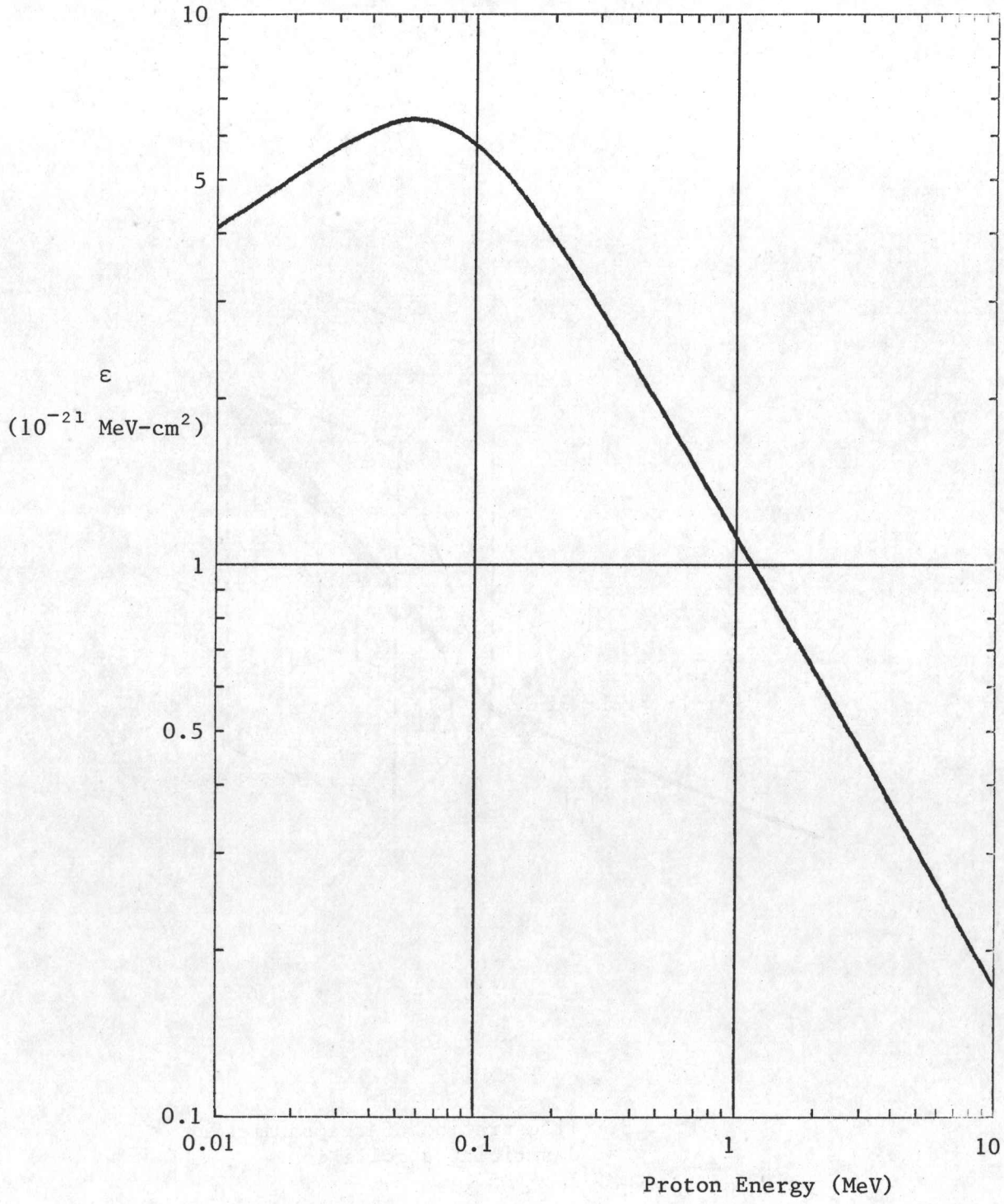

Fig. 4. Stopping cross section of atomic hydrogen for protons as a function of proton energy [16].

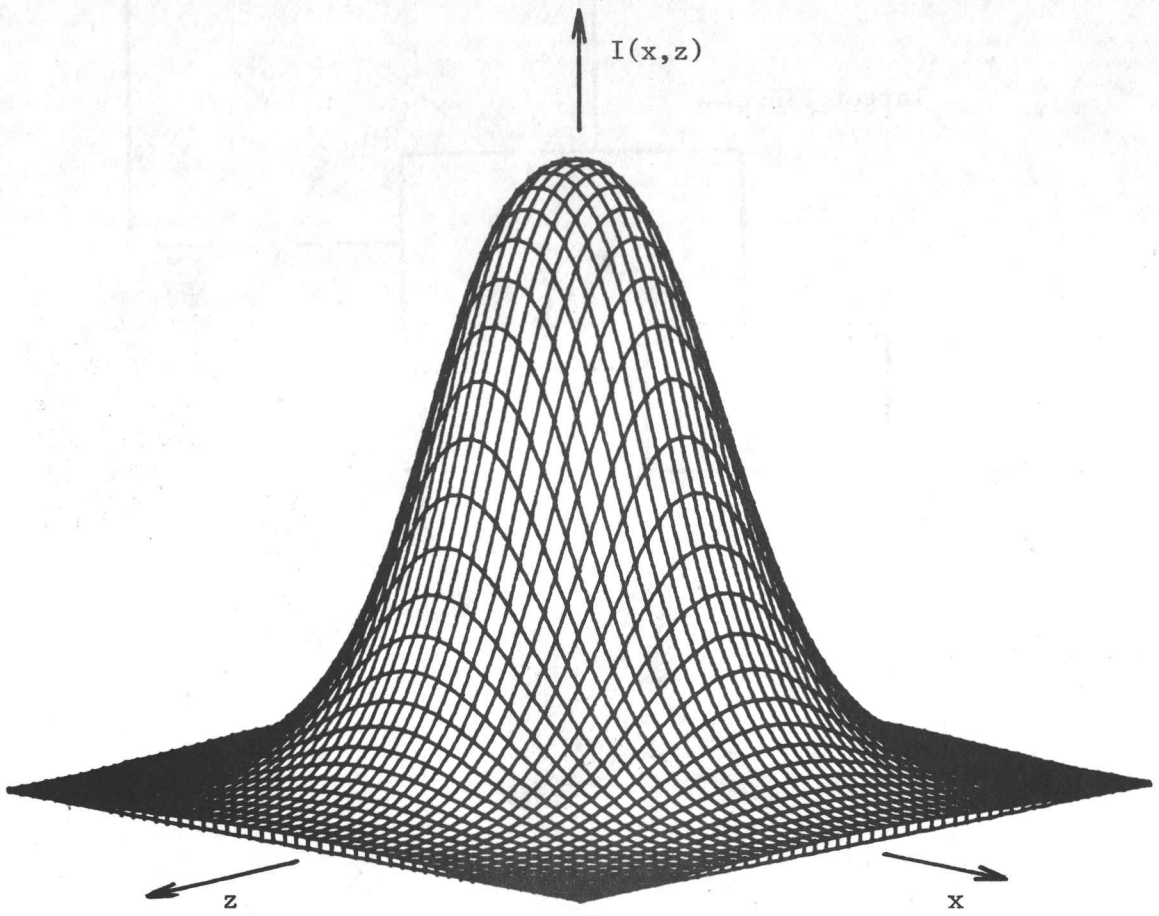

Fig. 5. Illustration of the ion beam intensity I(x,z) for a point source.

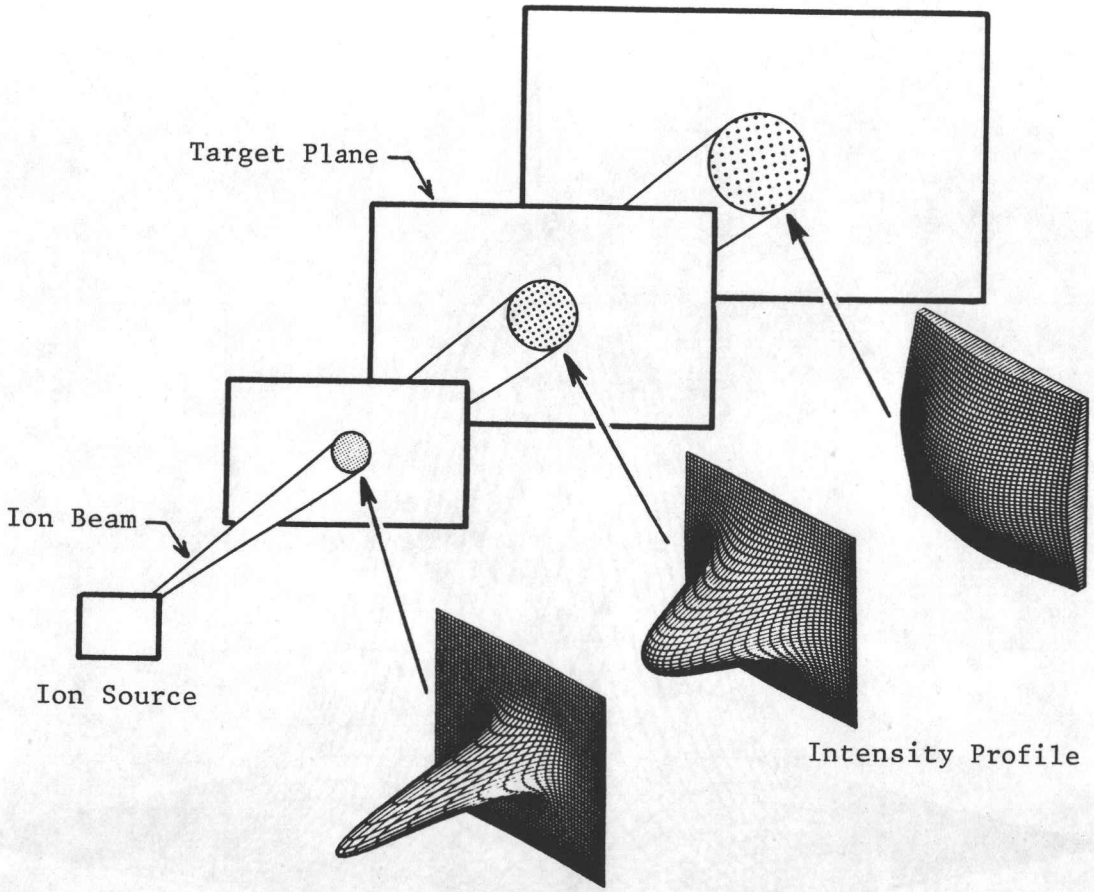

Fig. 6. Illustration of the lateral spreading of an ion beam with distance from a unidirectional point source.

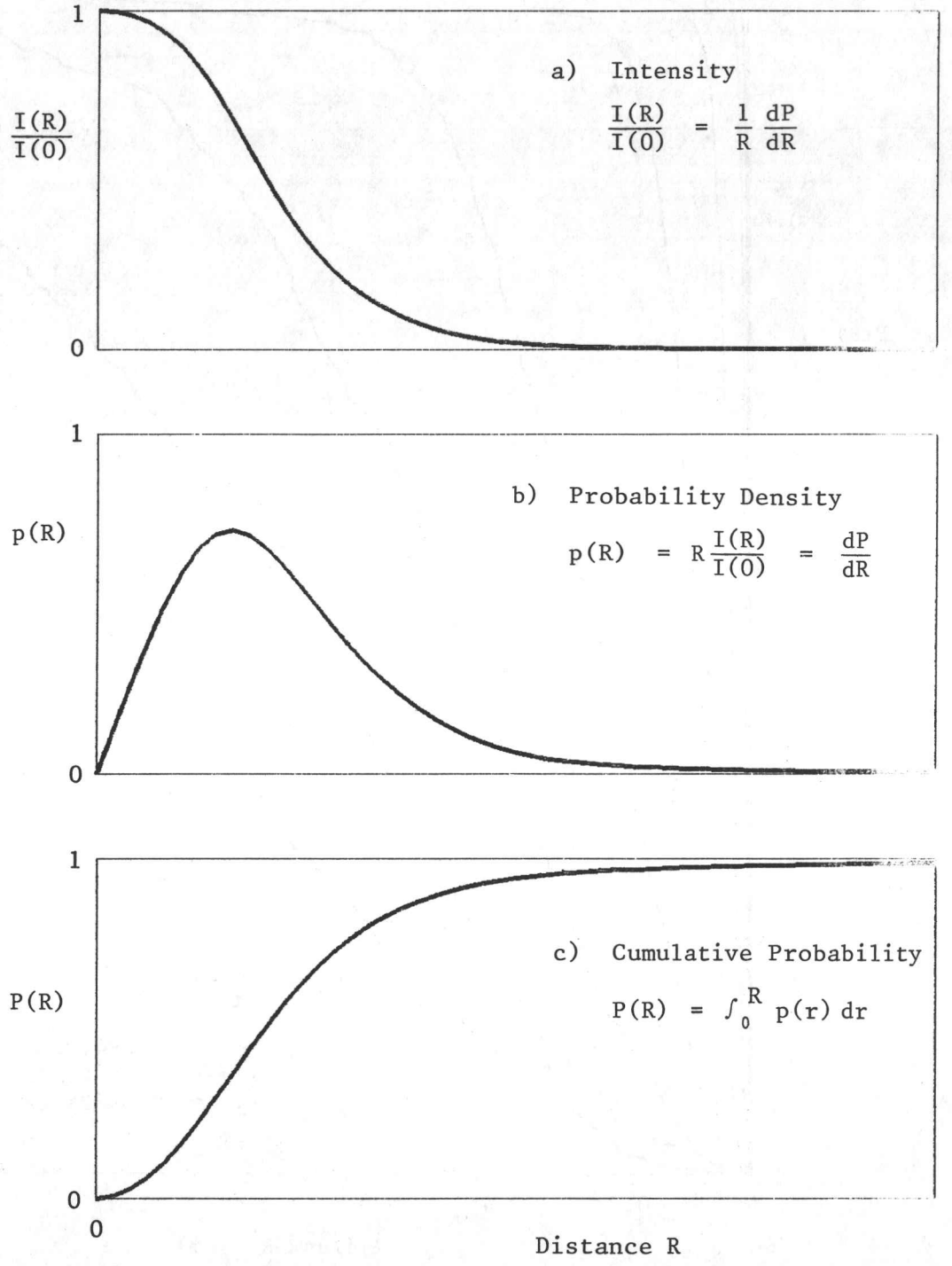

Fig. 7. Relationship between the ion beam intensity, probability density, and cumulative probability profiles.

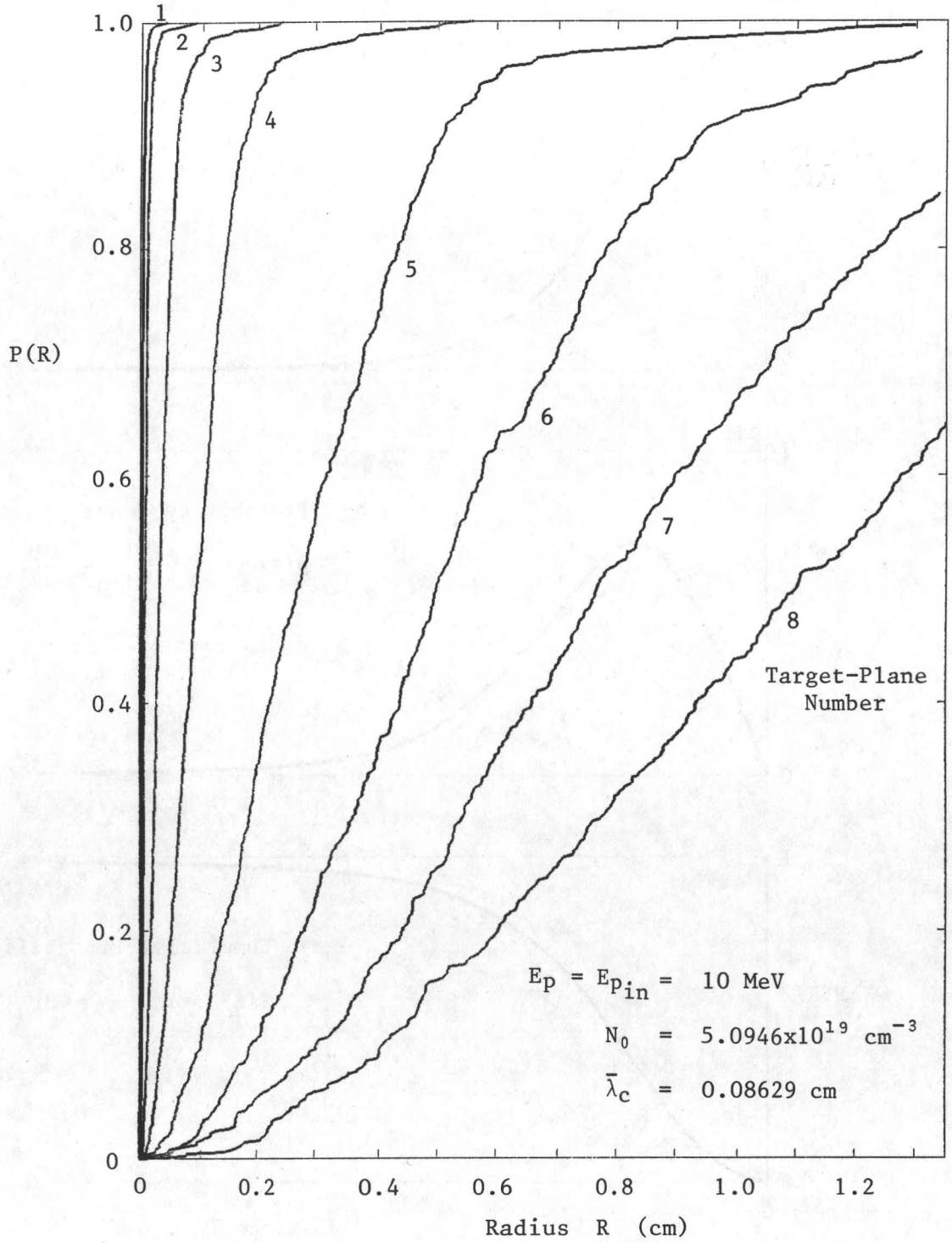

Fig. 8. Cumulative probability distributions generated by the Monte Carlo simulation for example 1 (constant proton energy and constant molecular hydrogen density). The numbered distributions correspond to target planes at increasing distances away from the point source (see the table in the text).

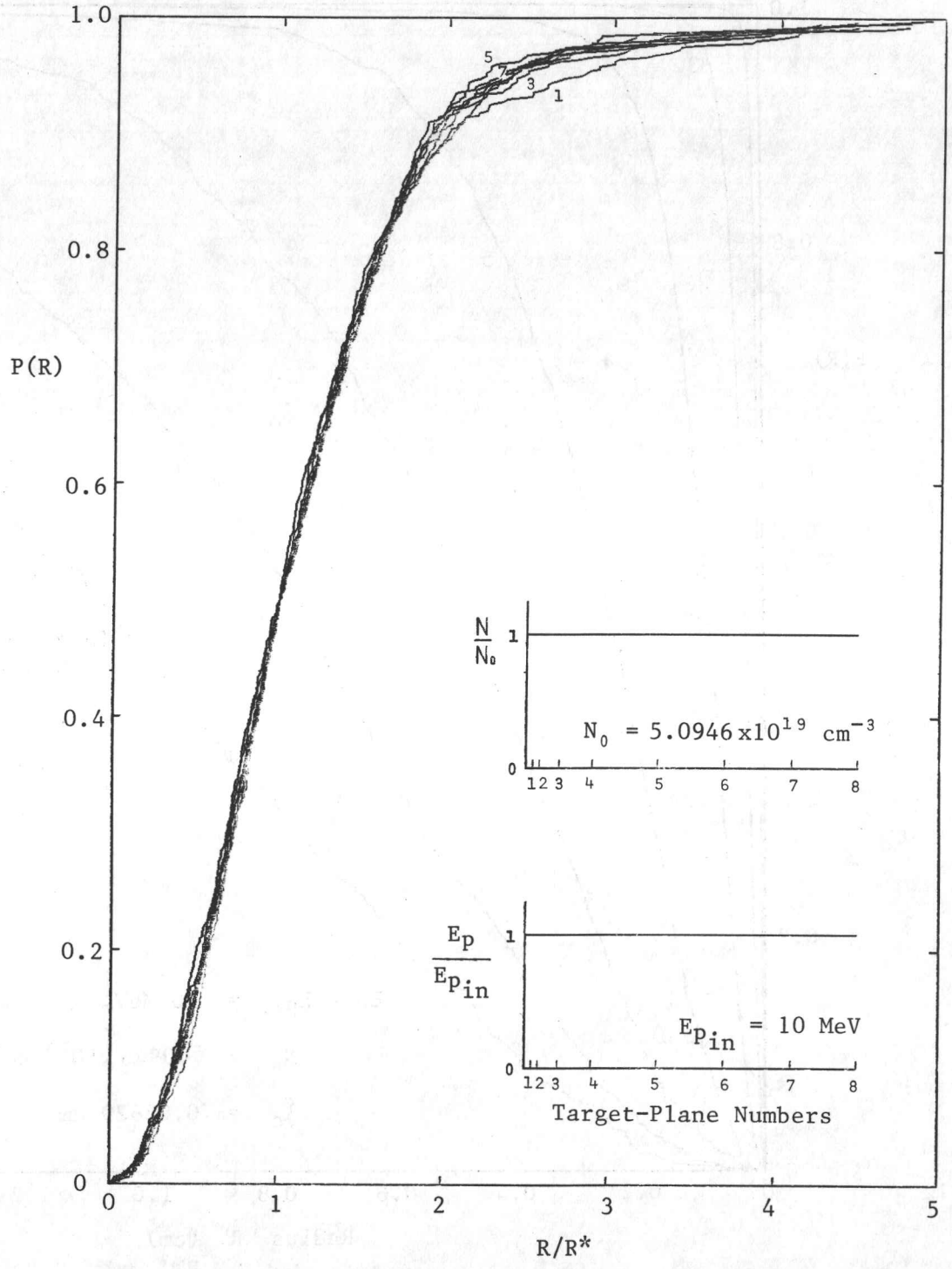

Fig. 9. Scaled cumulative probability distributions for example 1, to illustrate the self similarity of the successive distributions at increasing distances from the point source.

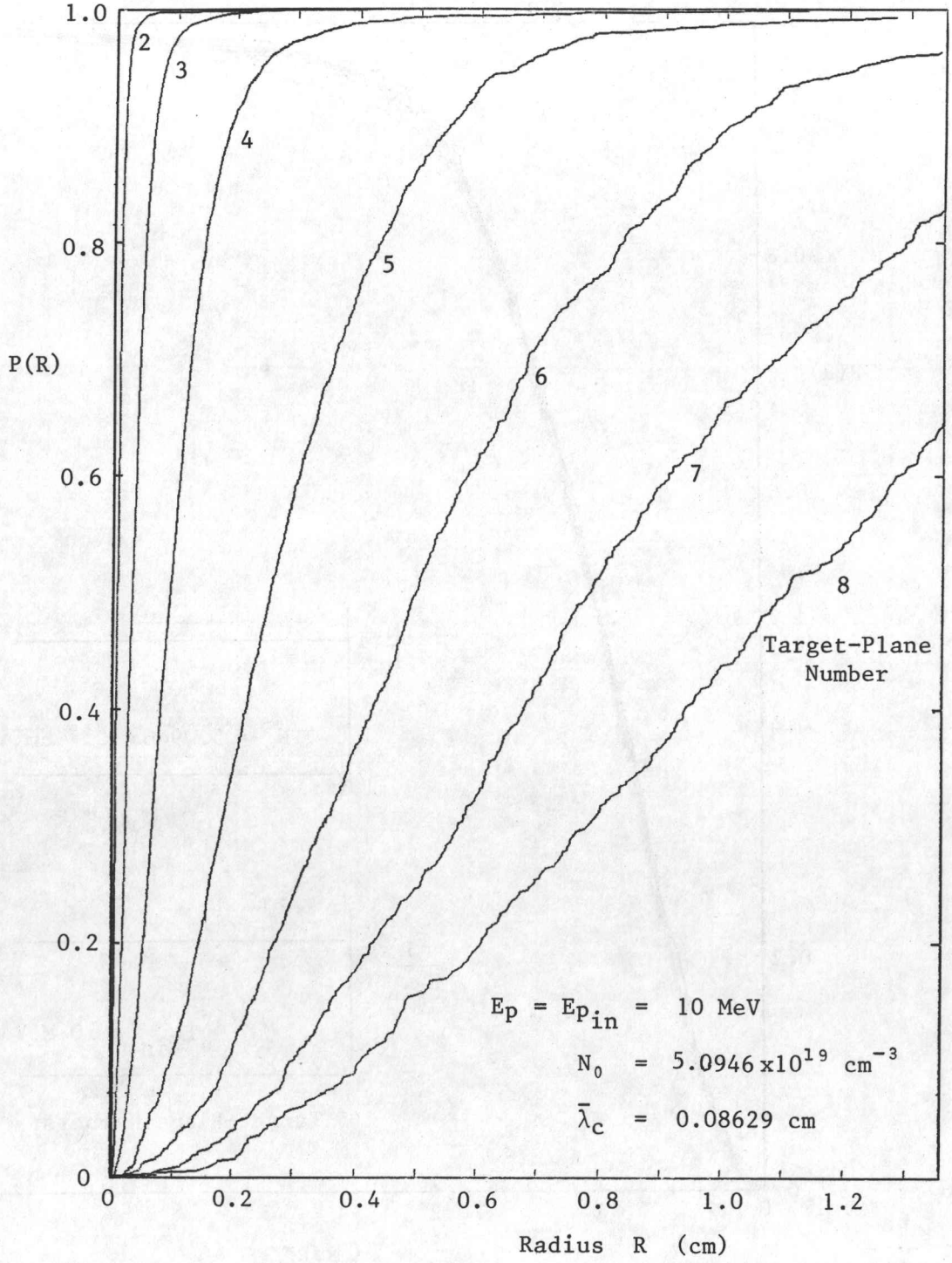

Fig. 10. Cumulative probability distributions for example 1, for which each distribution is now generated by the use of an equal number of collisions (not an equal number of proton paths).

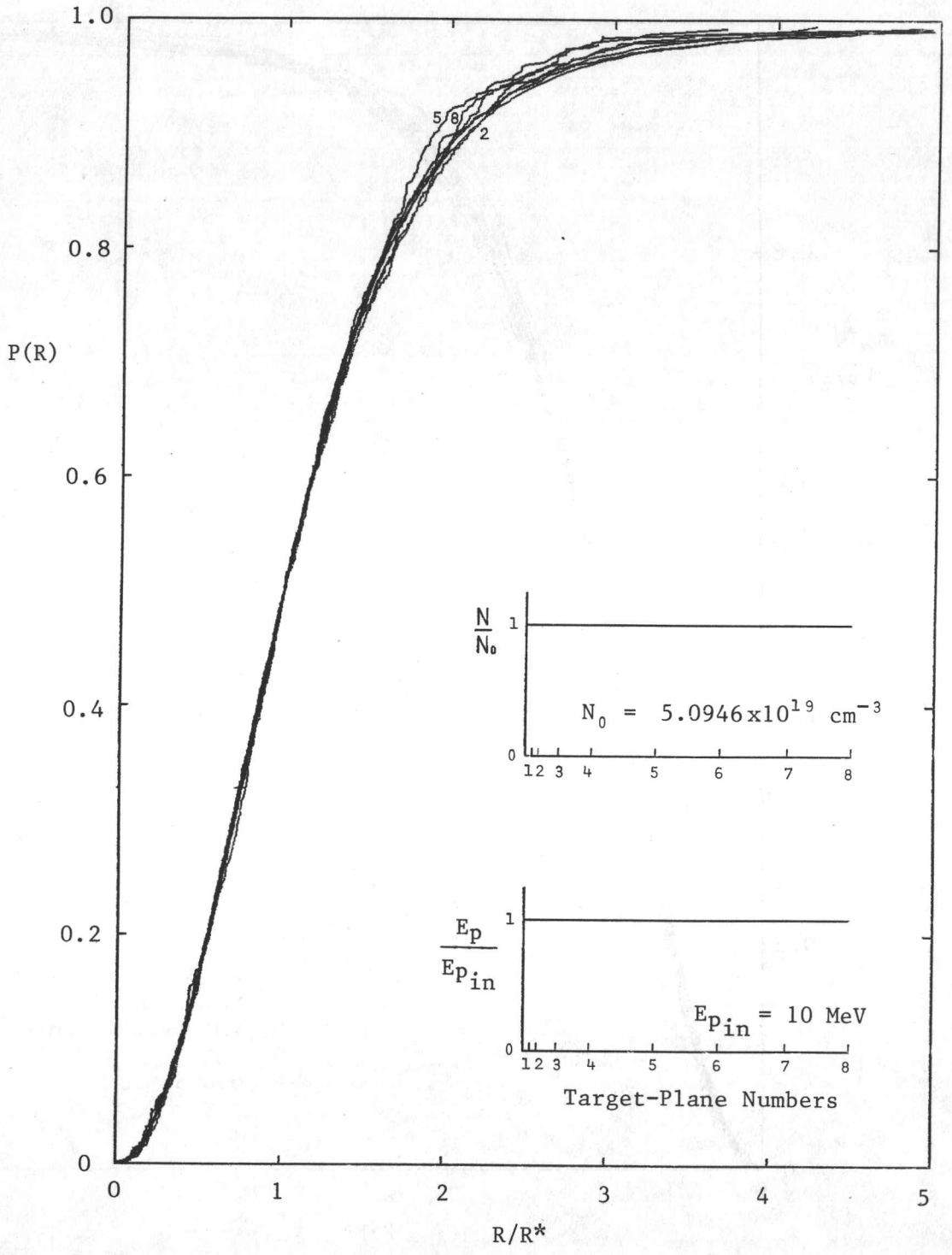

Fig. 11. Scaled cumulative probability distributions for example 1, for which each distribution is generated by using an equal number of collisions, in order to illustrate the self similarity of these successive distributions.

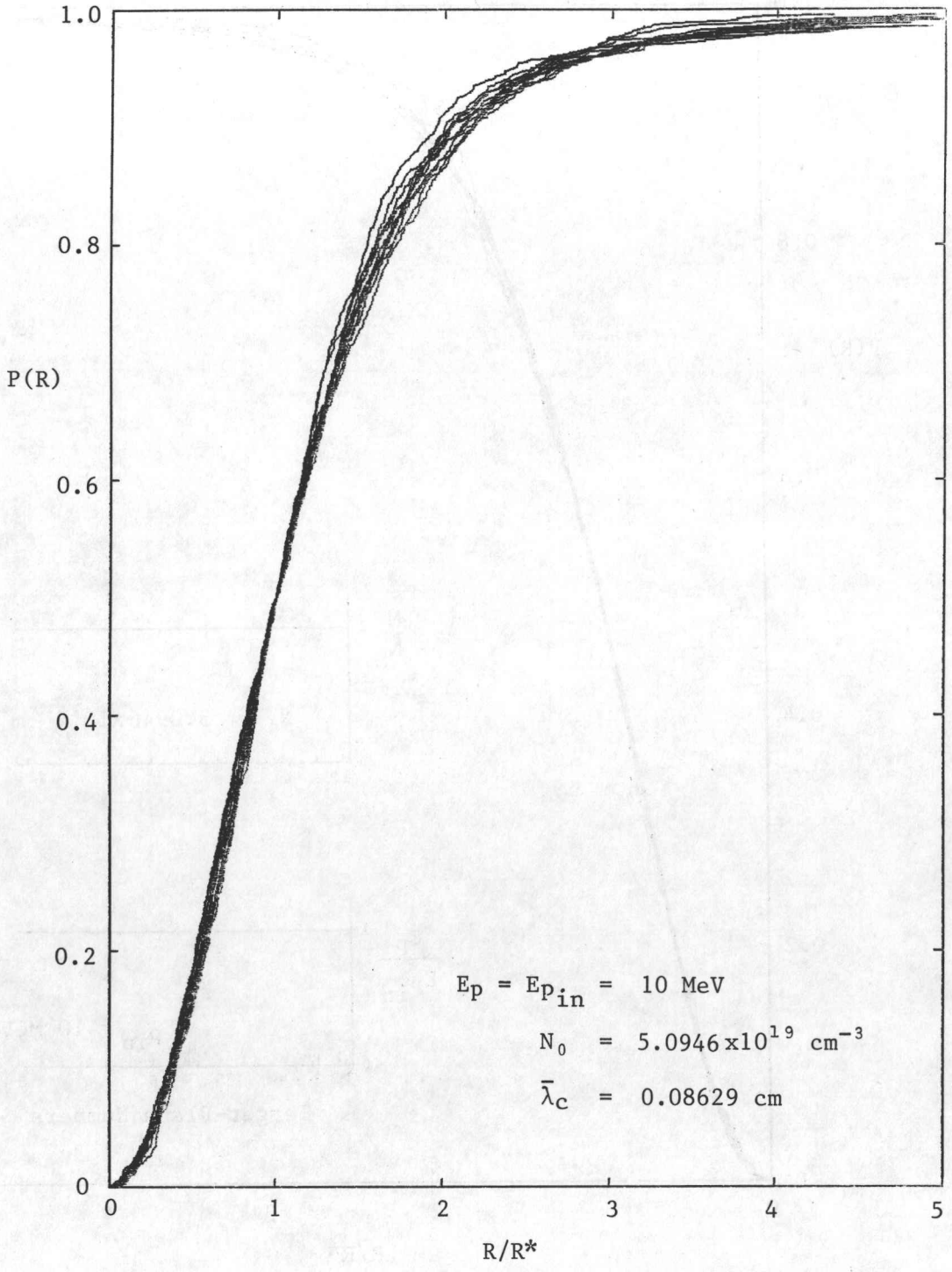

Fig. 12. Twelve scaled cumulative probability distributions for twelve separate Monte Carlo simulations with 1000 proton paths each, to the same target plane located 200 mean free paths ($\bar{\lambda}_c$) from the source.

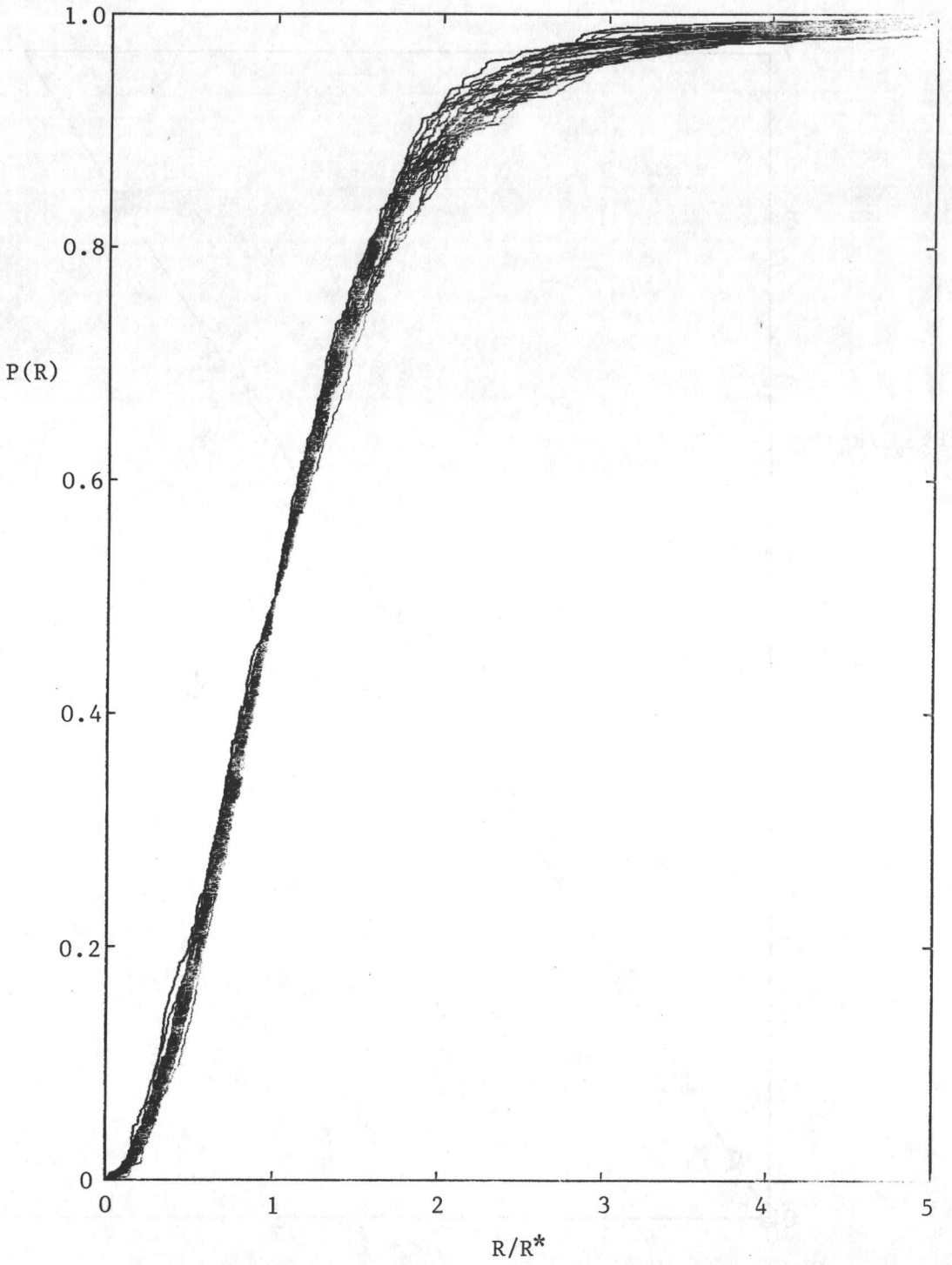

Fig. 13. Scaled cumulative probability distributions for the following three cases:

a) E_p = 10 MeV, $N_0 = 5.0946 \times 10^{19}$ cm^{-3}, $\bar{\lambda}_c = 8.629 \times 10^{-2}$ cm

b) E_p = 0.01 MeV, $N_0 = 5.0946 \times 10^{19}$ cm^{-3}, $\bar{\lambda}_c = 8.629 \times 10^{-5}$ cm

c) E_p = 10 MeV, $N_0 = 5.0946 \times 10^{18}$ cm^{-3}, $\bar{\lambda}_c = 8.629 \times 10^{-1}$ cm

For each case the target planes are located at distances of 100, 200, 500, 1000, 2000, 3000, 4000, and 5000 $\bar{\lambda}_c$.

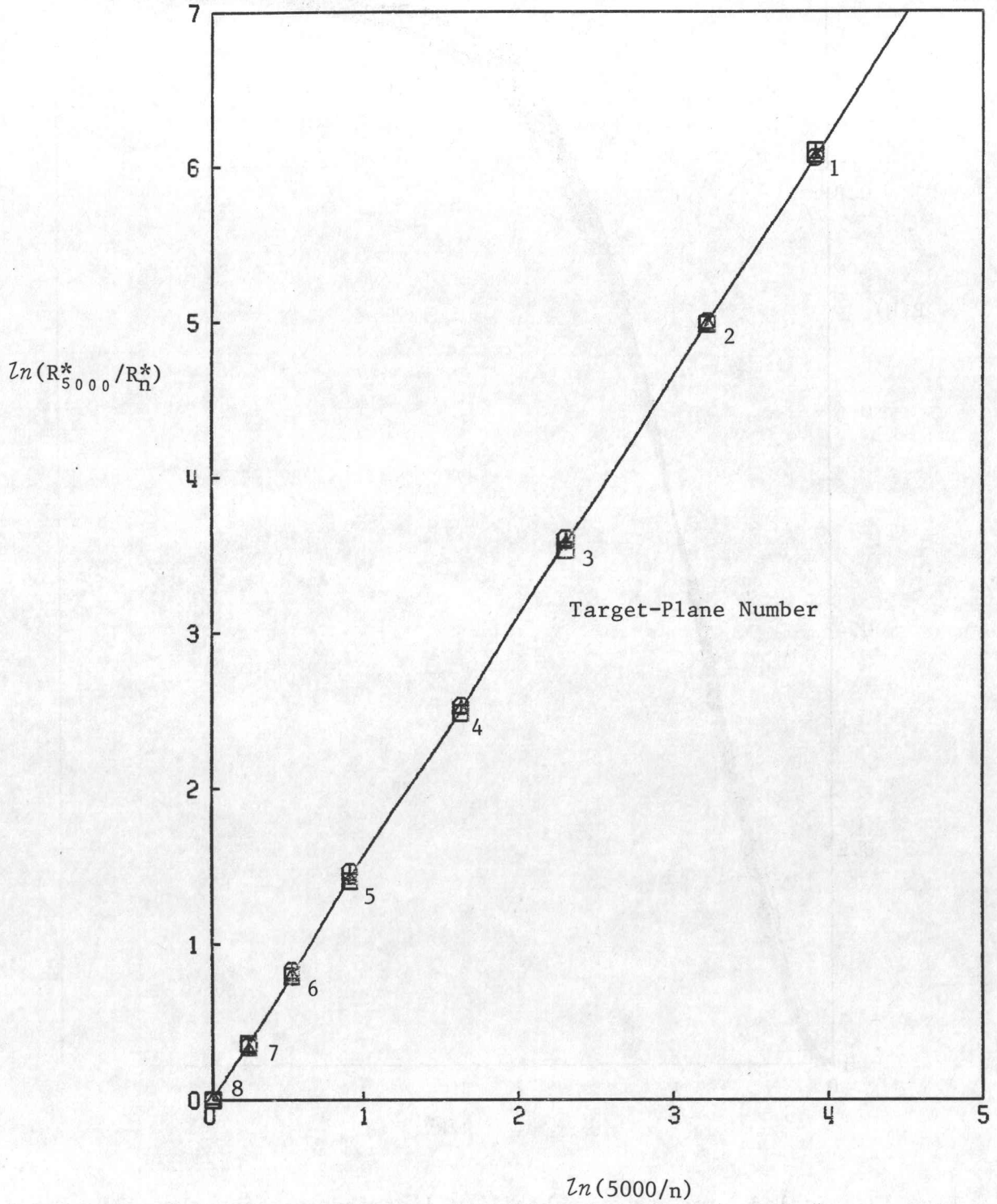

Fig. 14. Plot of the R values given by P(R) = 0.5 from the cumulative probability distributions for cases a (□), b (○), and c (△). The straight line through these points is the first-order, least-squares best fit.

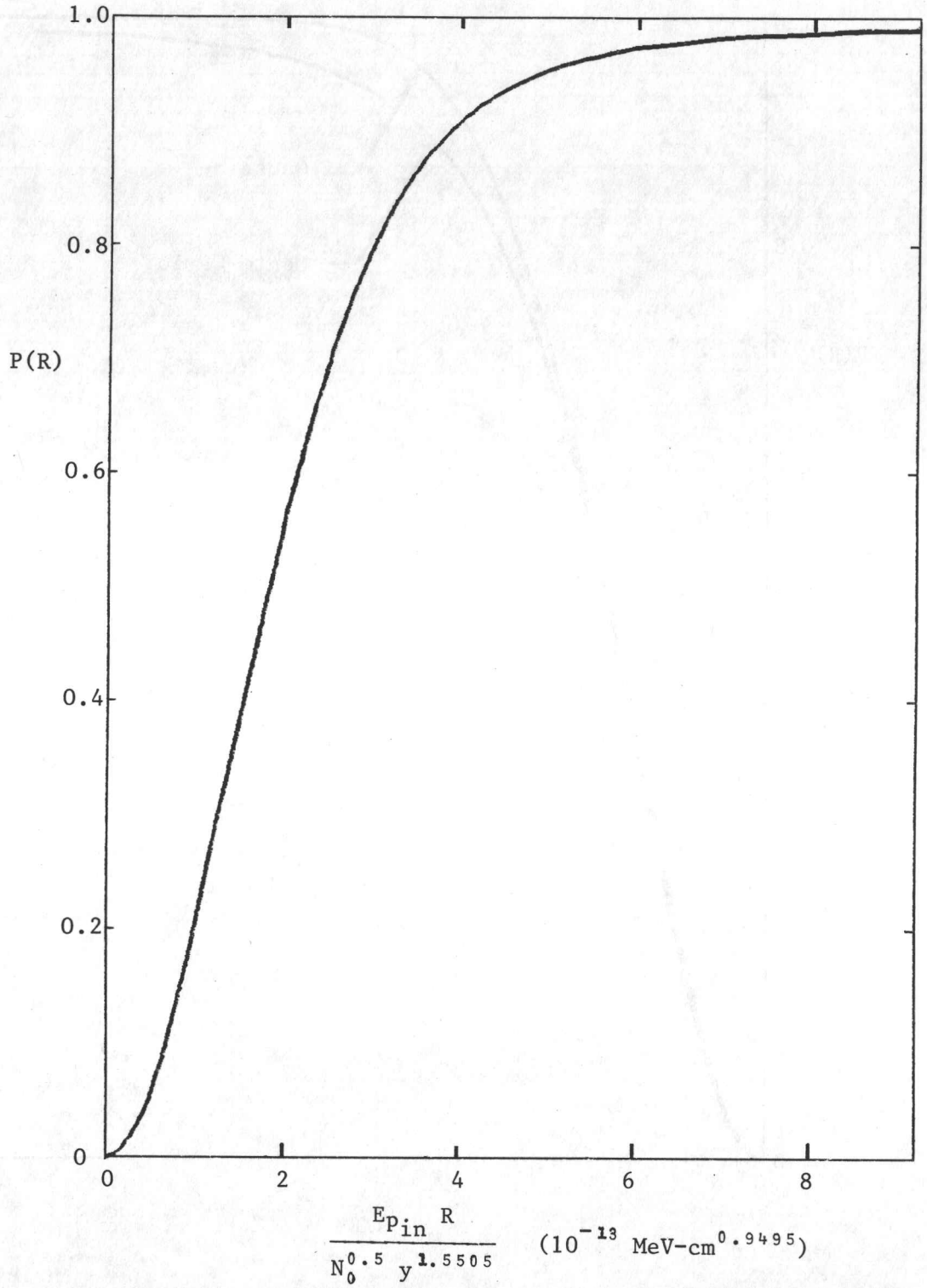

Fig. 15. Reference cumulative probability distribution generated by a Monte Carlo simulation, for which 12,500 proton paths were followed from the point source out to a distance of 200 mean-free paths.

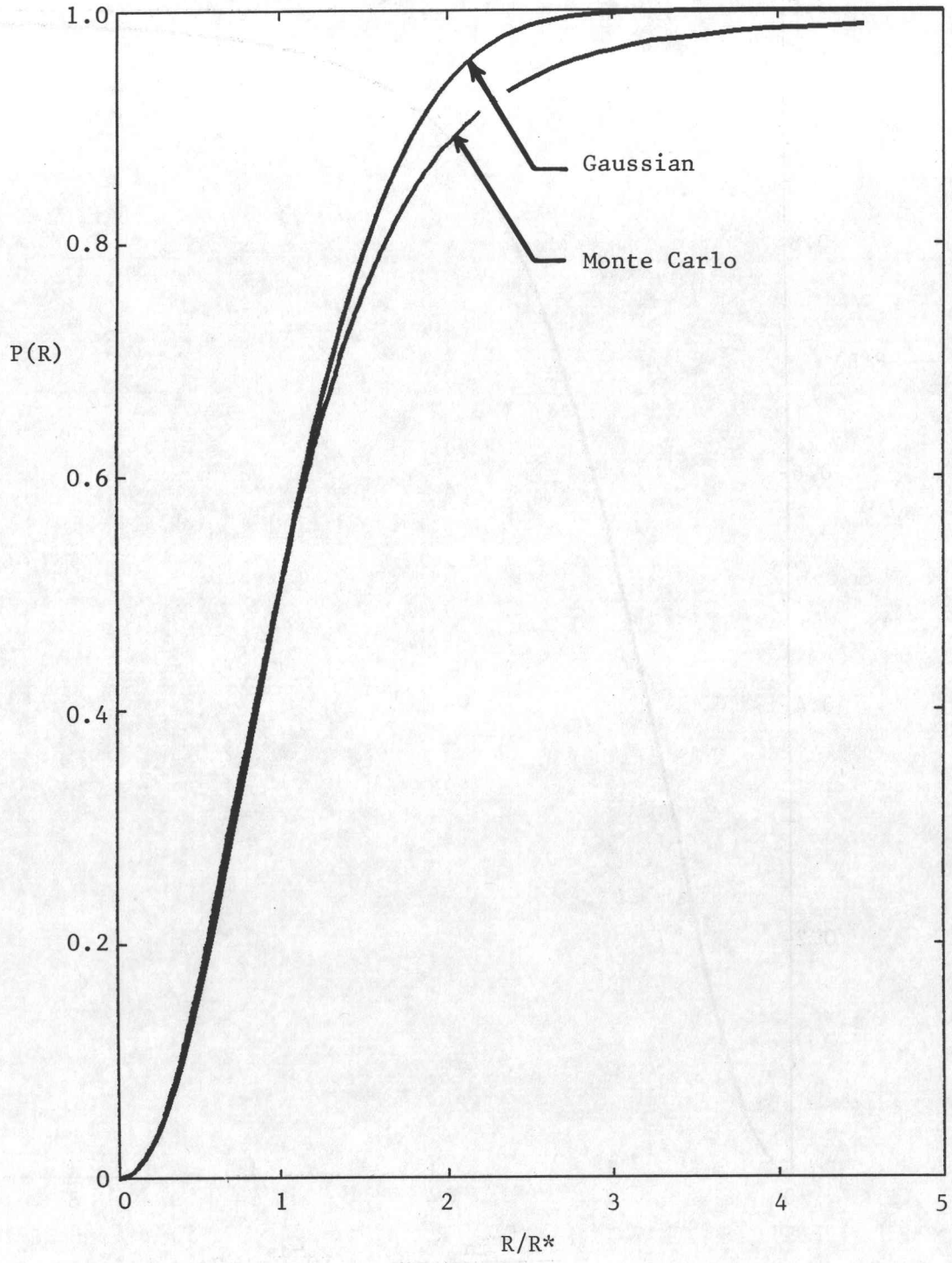

Fig. 16. Comparison of the Monte Carlo generated cumulative probability distribution with the Gaussian distribution predicted by the multiple small angle scattering theory. The single large angle scattering tail is clearly seen in the Monte Carlo distribution.

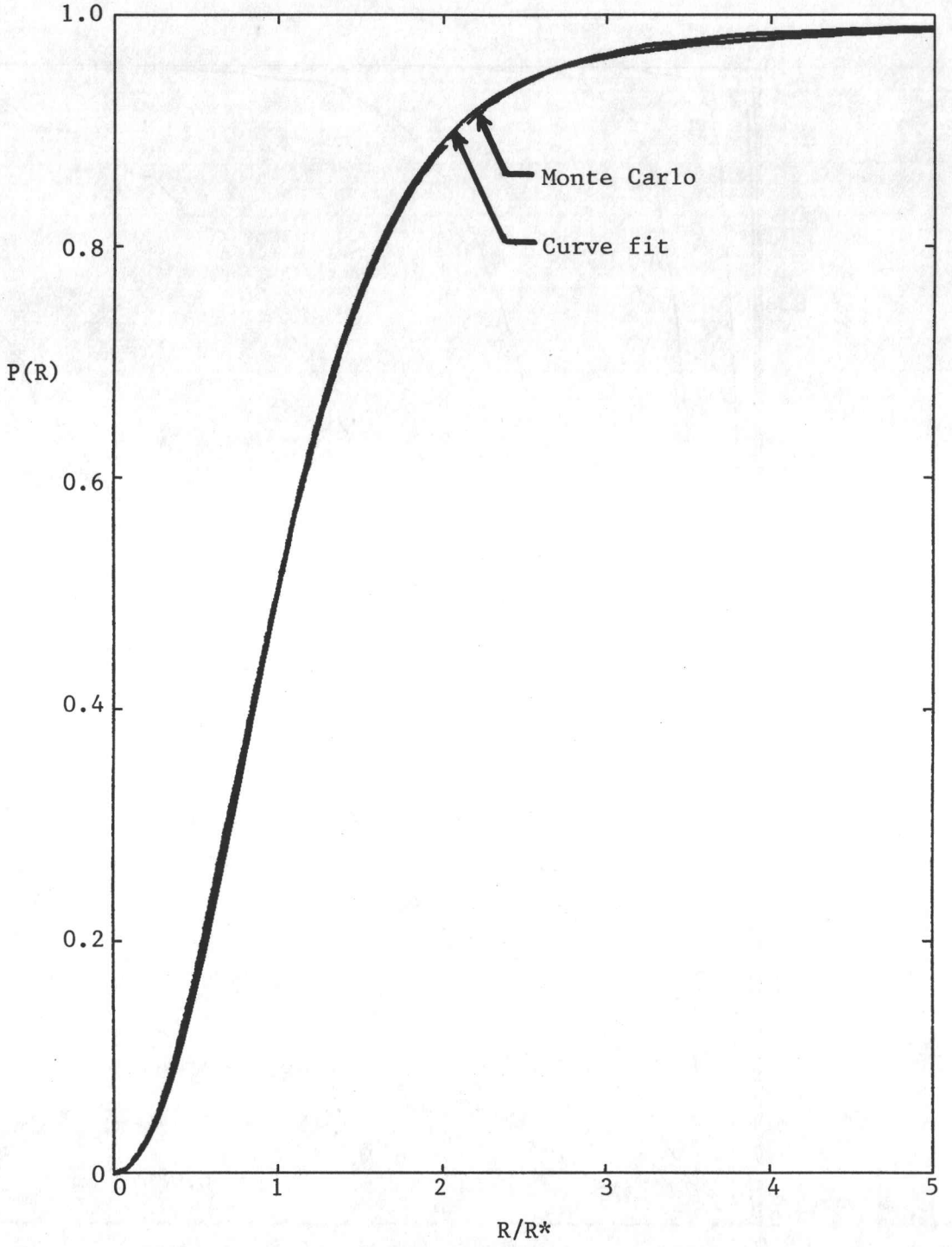

Fig. 17. Comparison of the Monte Carlo generated cumulative probability distribution P(R) and the curve fit given by equation 2.36.

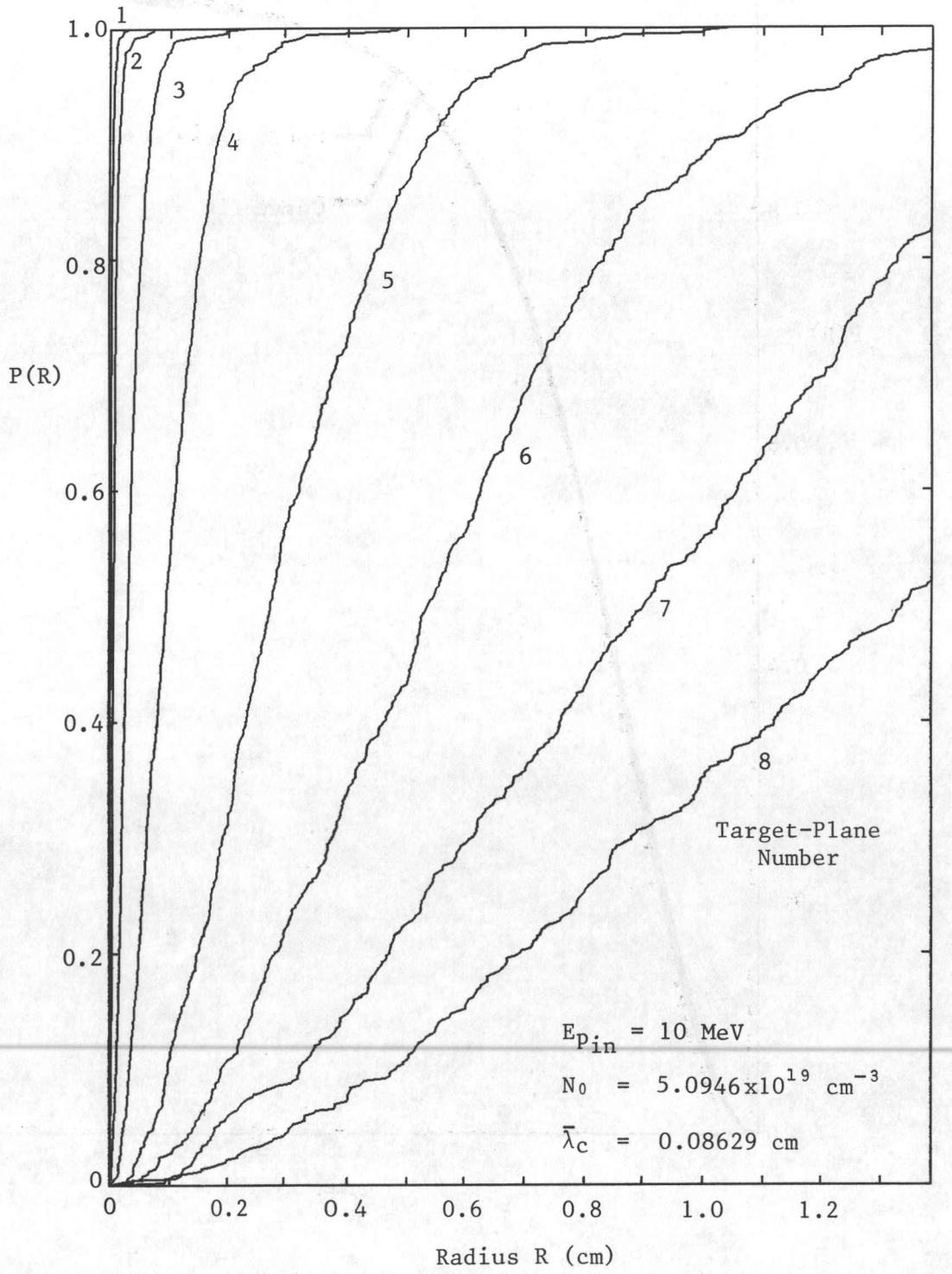

Fig. 18. Cumulative probability distributions generated by the Monte Carlo simulation for example 2 (constant molecular hydrogen gas and decreasing proton energy). The numbered distributions correspond to target planes at increasing distances away from the point source (see the table in the text).

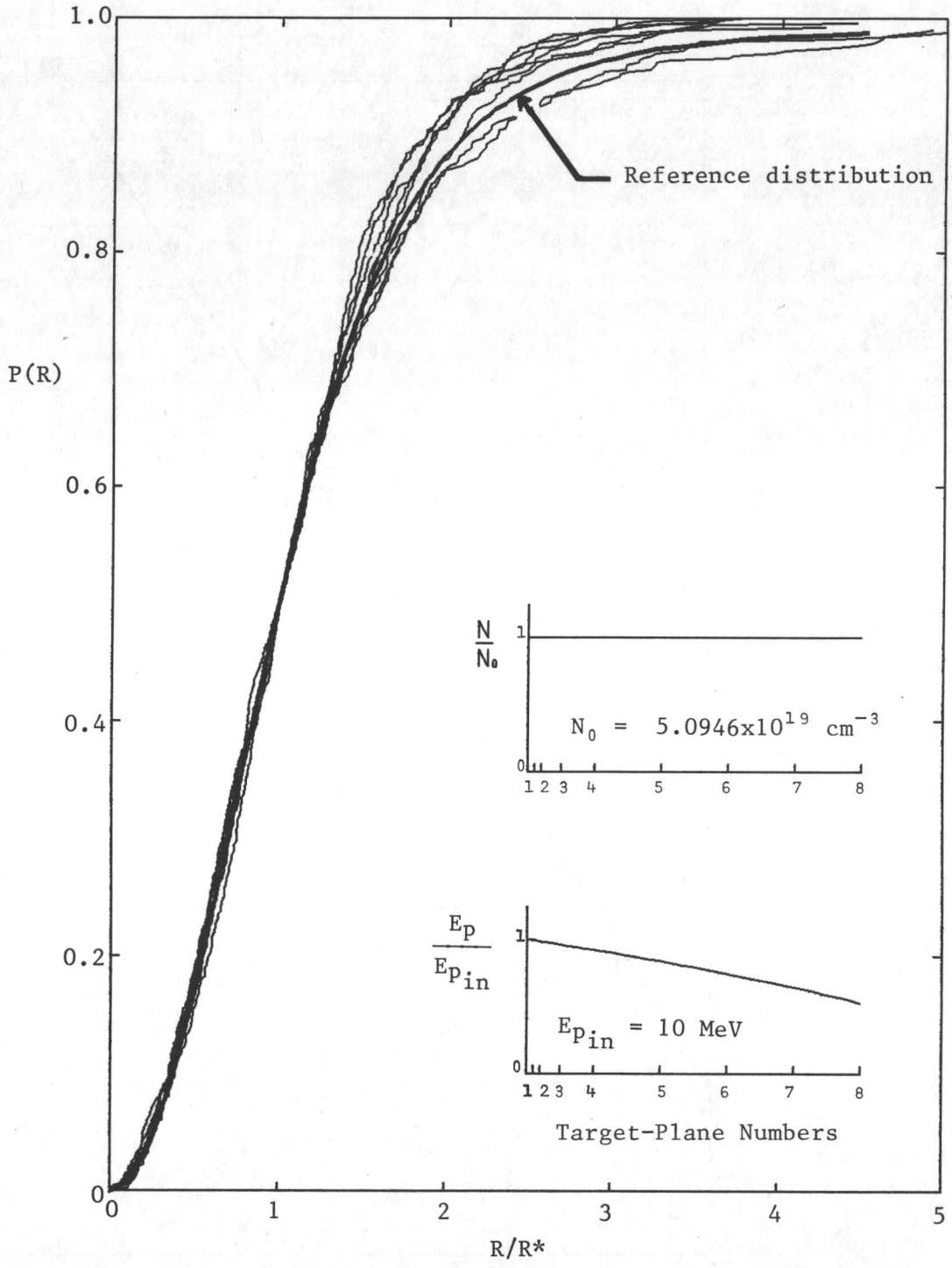

Fig. 19. Scaled cumulative probability distributions for example 2, to illustrate the self similarity of the successive distributions at increasing distances from the point source. The distribution indicated by the thickest line is the reference distribution obtained in example 1. This illustrates that similarity between the distributions exists for examples 1 and 2.

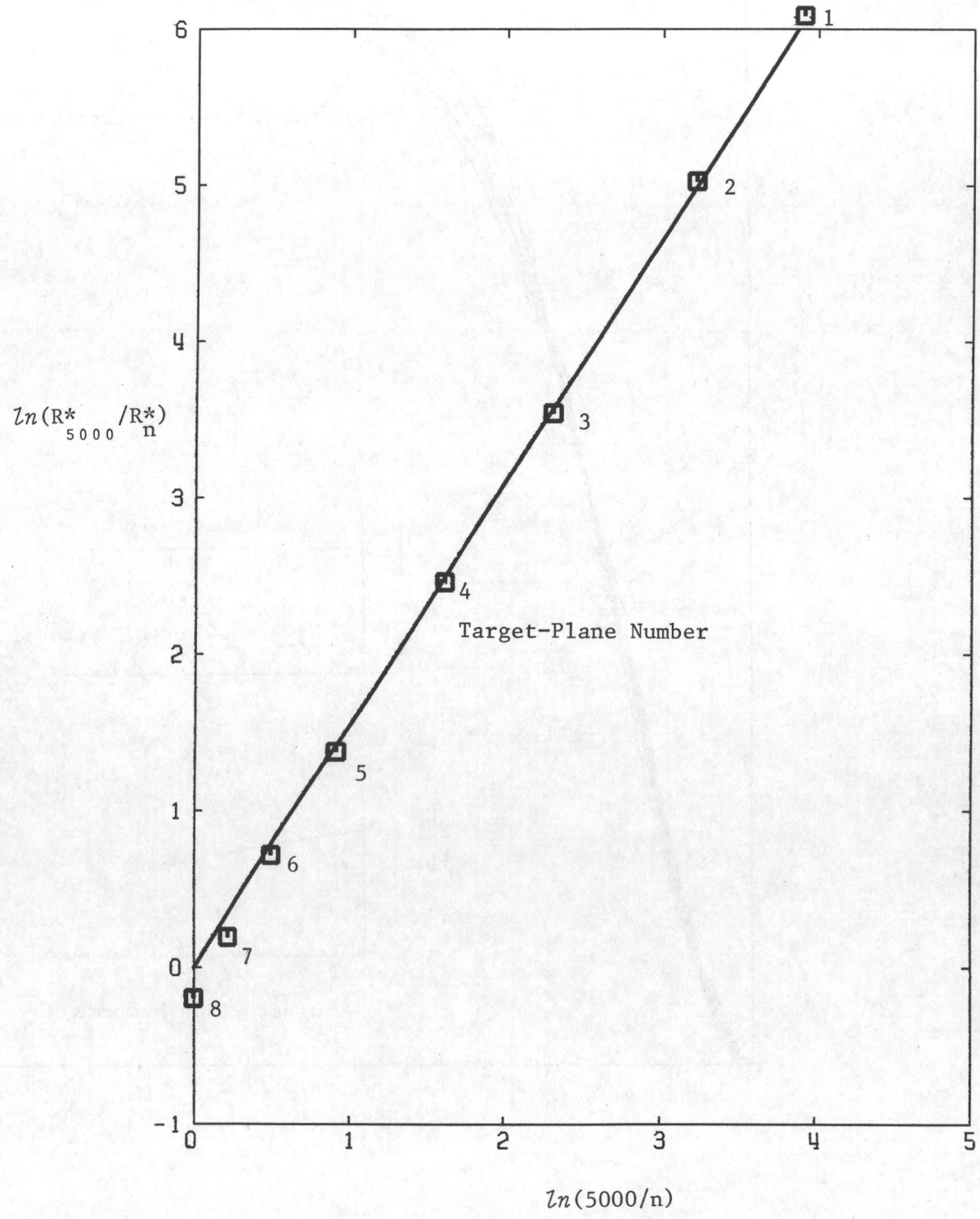

Fig. 20. Plot of the R values given by P(R) = 0.5 from the cumulative probability distributions for example 2. The straight line is the first-order, least-squares best fit given by Eq. 2.34.

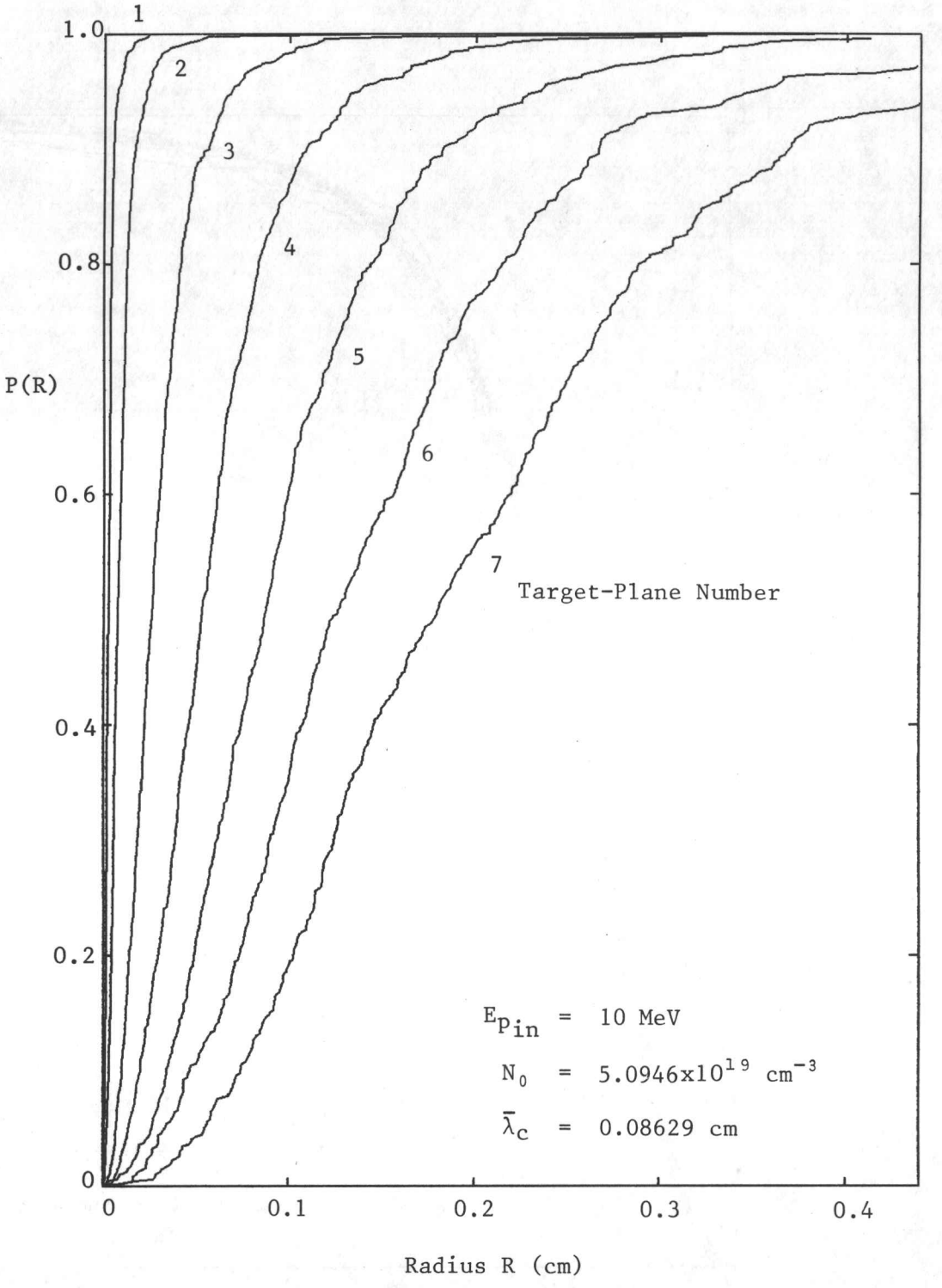

Fig. 21. Cumulative probability distributions generated by the Monte Carlo simulation for example 3. The numbered distributions correspond to target planes at increasing distances away from the point source (see the table in the text).

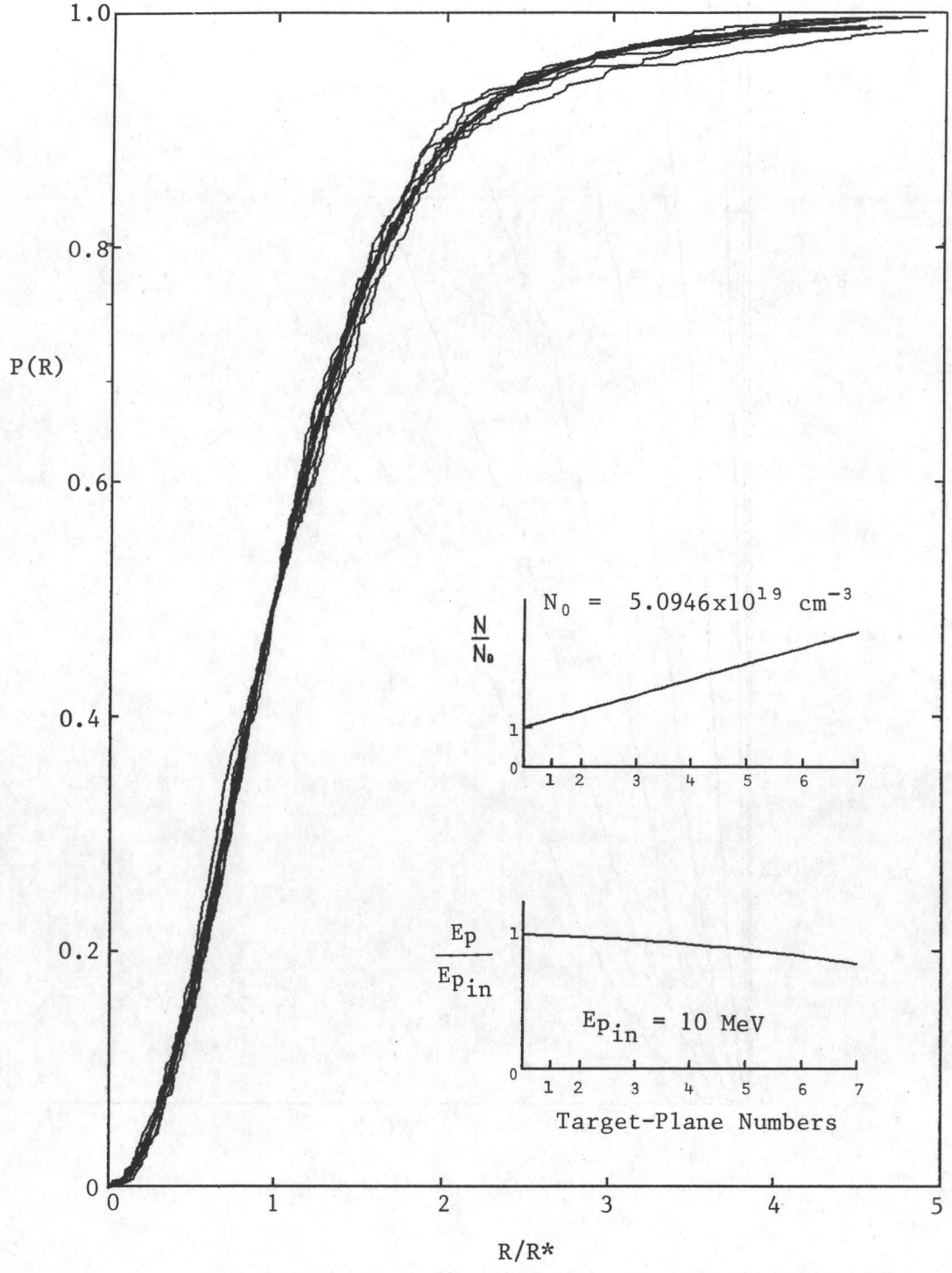

Fig. 22. Scaled cumulative probability distributions for example 3, to illustrate the self similarity of the successive distributions at increasing distances from the point source. The distribution indicated by the thickest line is the reference distribution obtained in example 1. This illustrates that similarity between the distributions exists for examples 1 and 3.

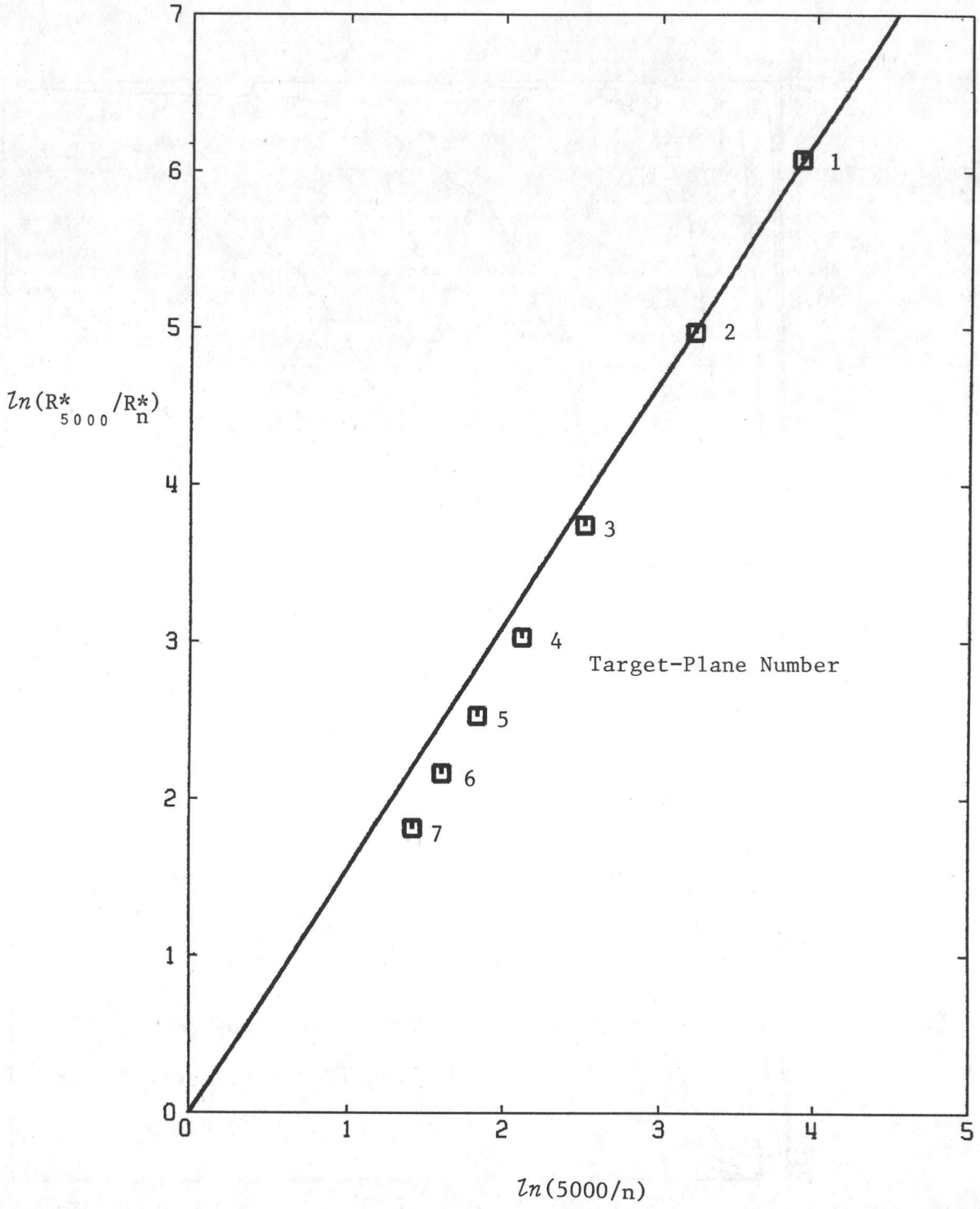

Fig. 23. Plot of the R values given by P(R) = 0.5 from the cumulative probability distributions for example 3. The straight line is the first-order, least-squares best fit given by Eq. 2.34.

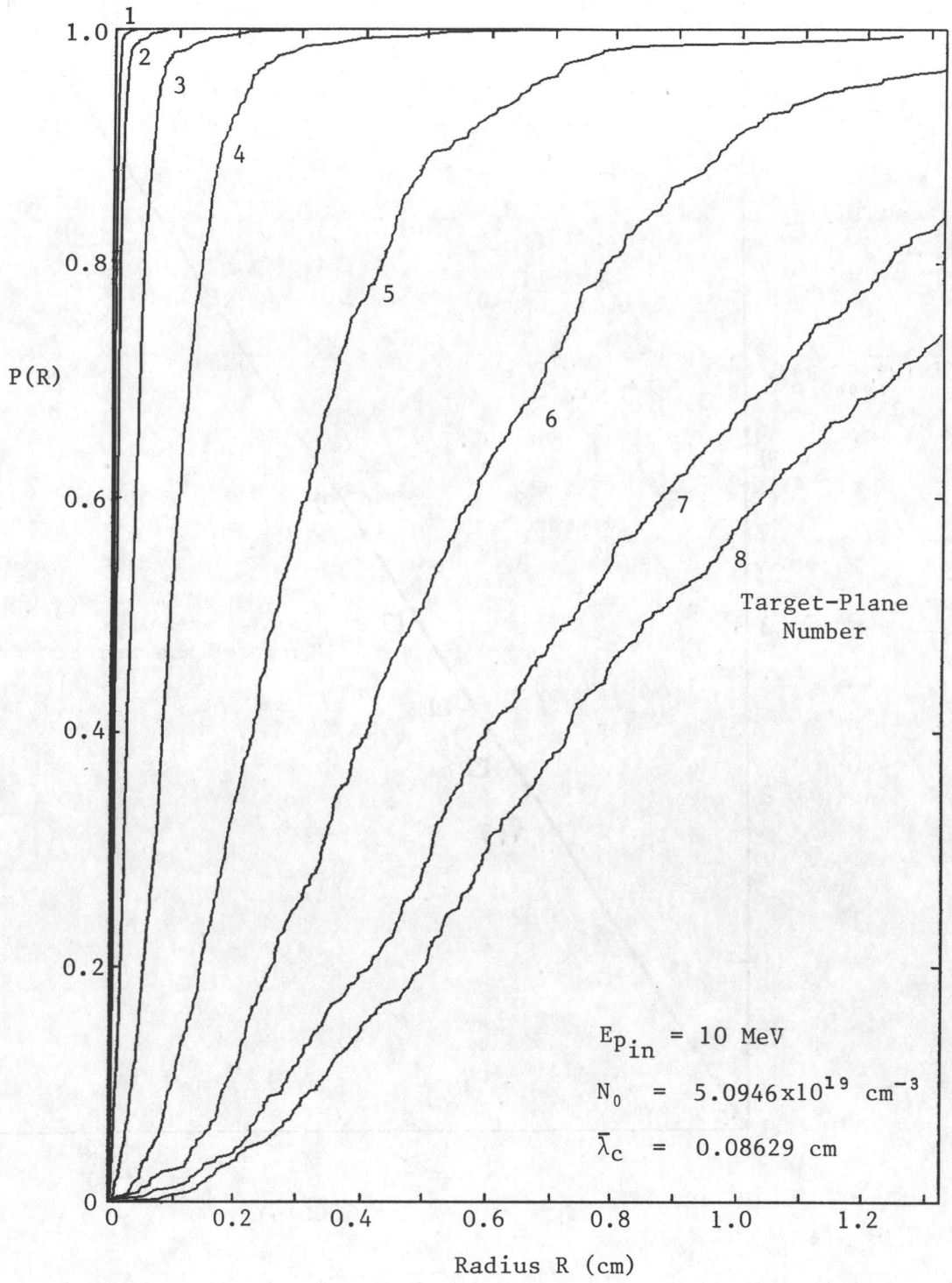

Fig. 24. Cumulative probability distributions generated by the Monte Carlo simulation for example 4. The numbered distributions correspond to target planes at increasing distances away from the point source (see the table in the text).

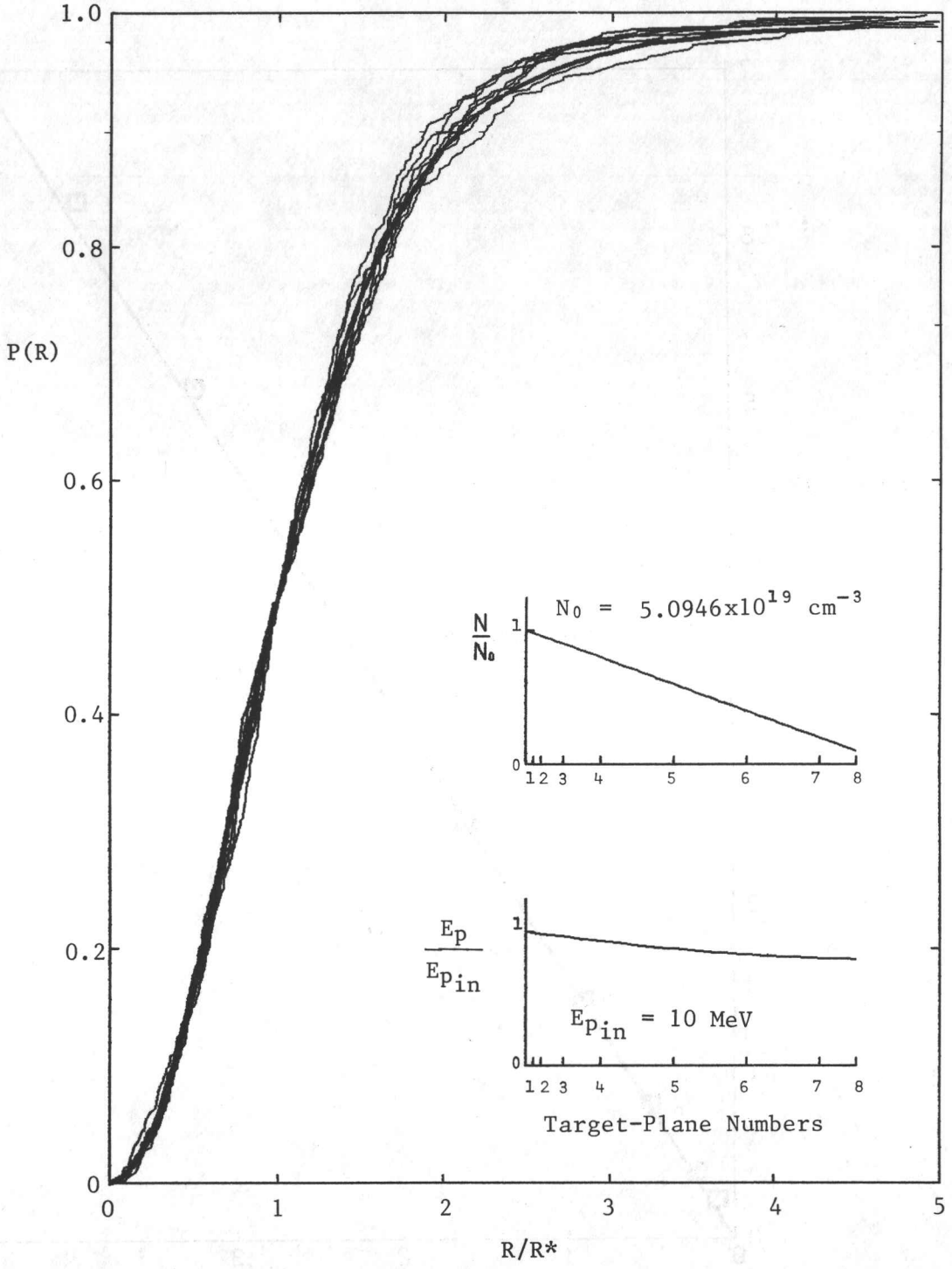

Fig. 25. Scaled cumulative probability distributions for example 4, to illustrate the self similarity of the successive distributions at increasing distances from the point source. The distribution indicated by the thickest line is the reference distribution obtained in example 1. This illustrates that similarity between the distributions exists for examples 1 and 4.

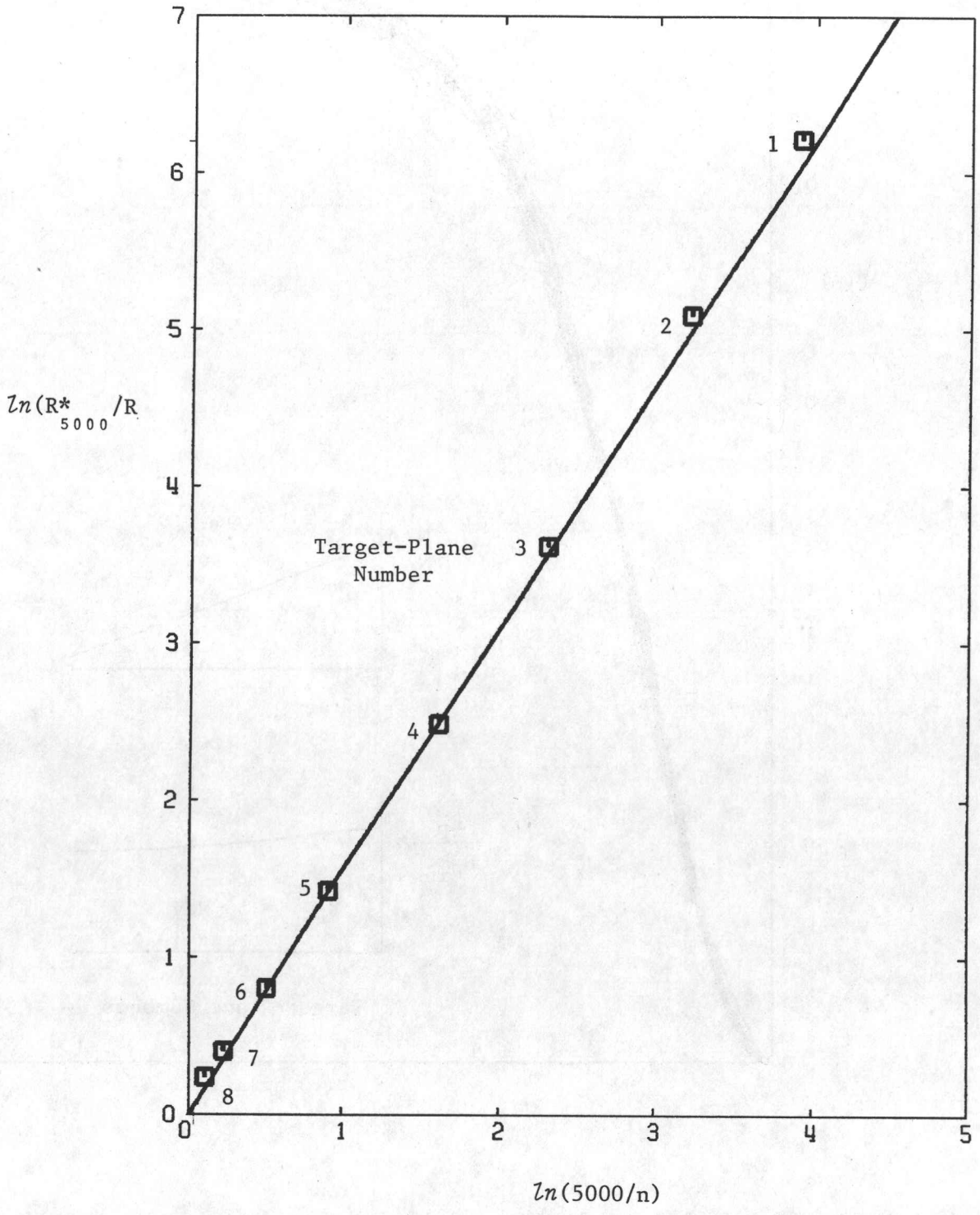

Fig. 26. Plot of the R values given by P(R) = 0.5 from the cumulative probability distributions for example 4. The straight line is the first-order, least-squares best fit of Eq. 2.34.

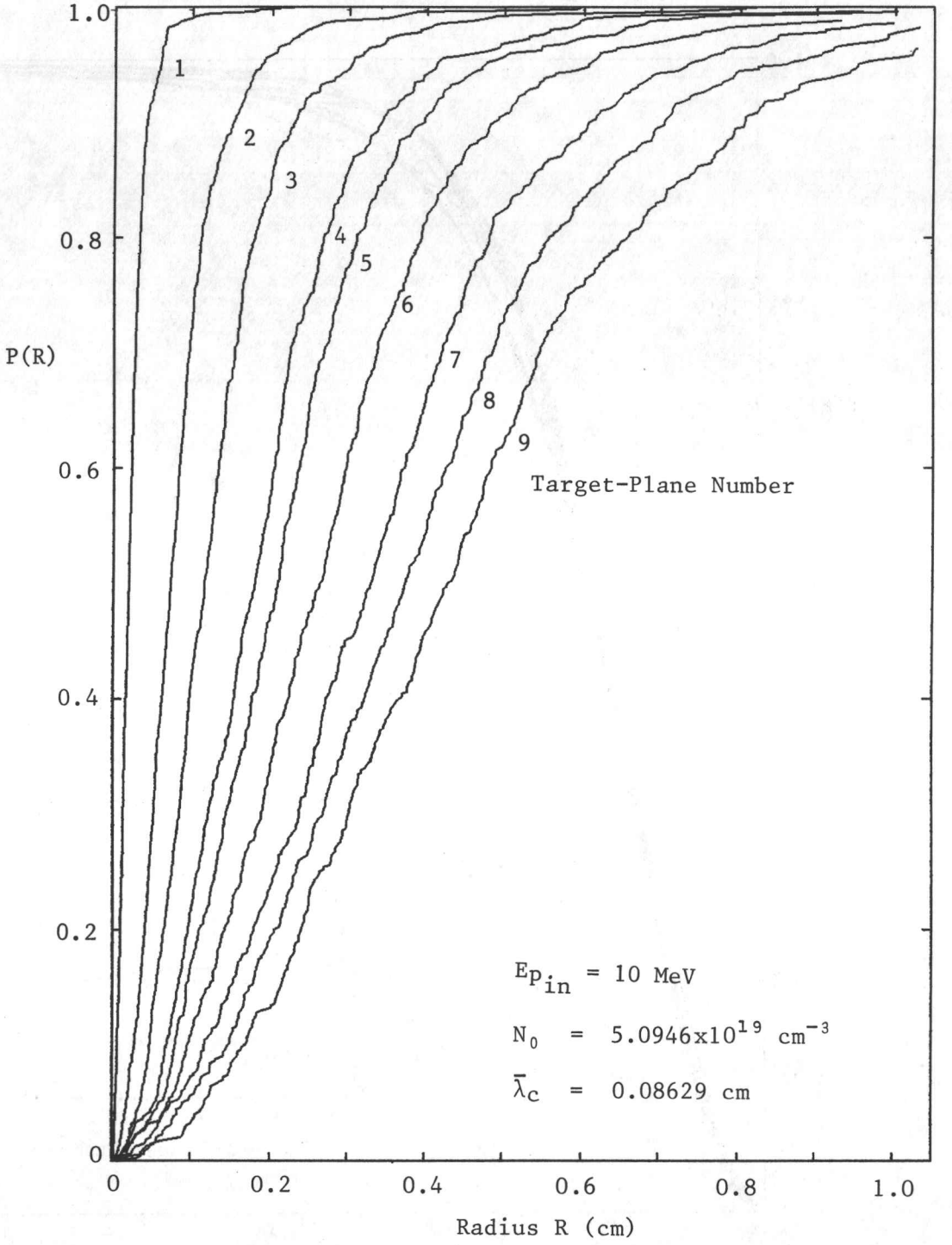

Fig. 27. Cumulative probability distributions generated by the Monte Carlo simulation for example 5. The numbered distributions correspond to target planes at increasing distances away from the point source (see the table in the text).

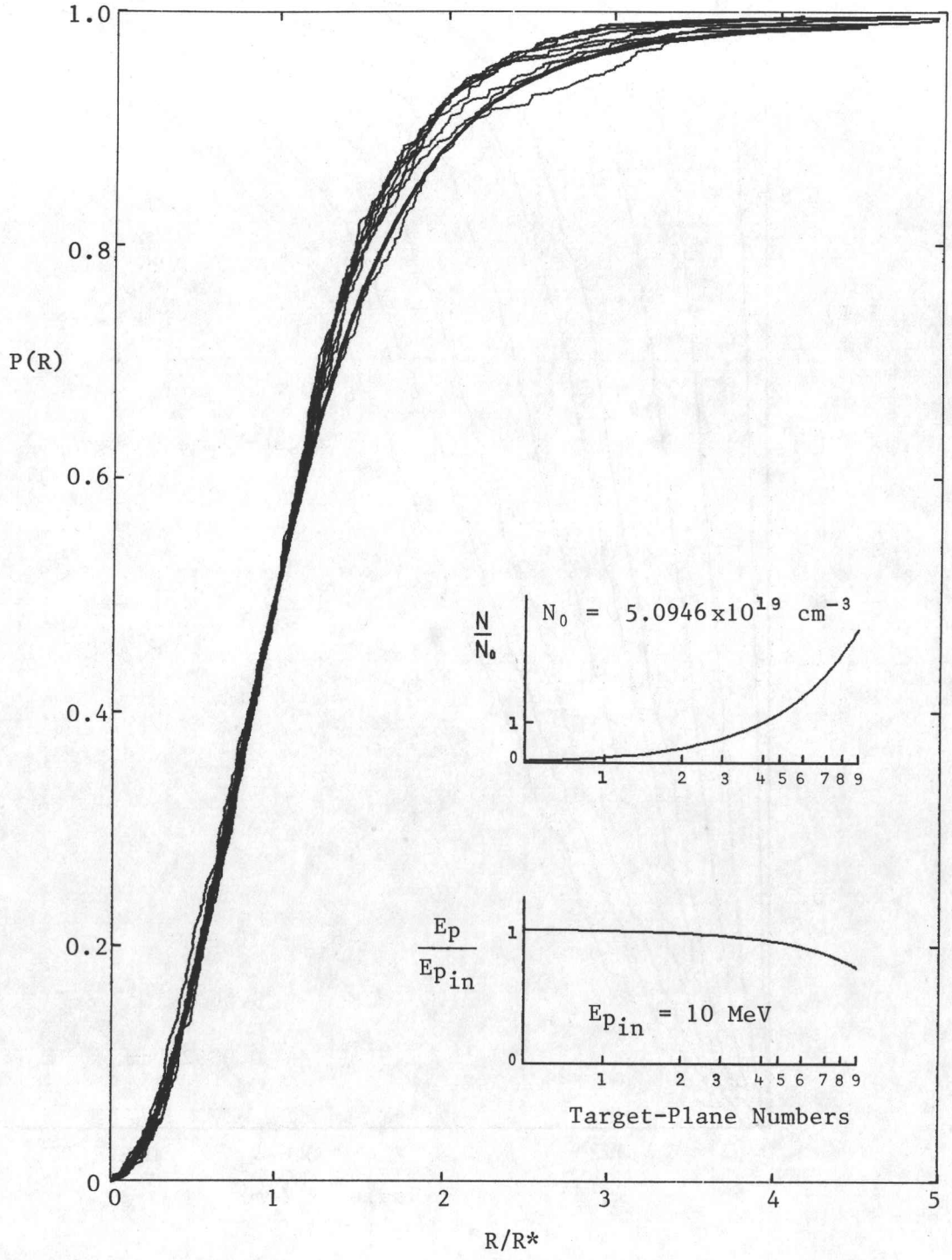

Fig. 28. Scaled cumulative probability distributions for example 5, to illustrate the self similarity of the successive distributions at increasing distances from the point source. The distribution indicated by the thickest line is the reference distribution obtained in example 1. This illustrates that similarity between the distributions exists for examples 1 and 5.

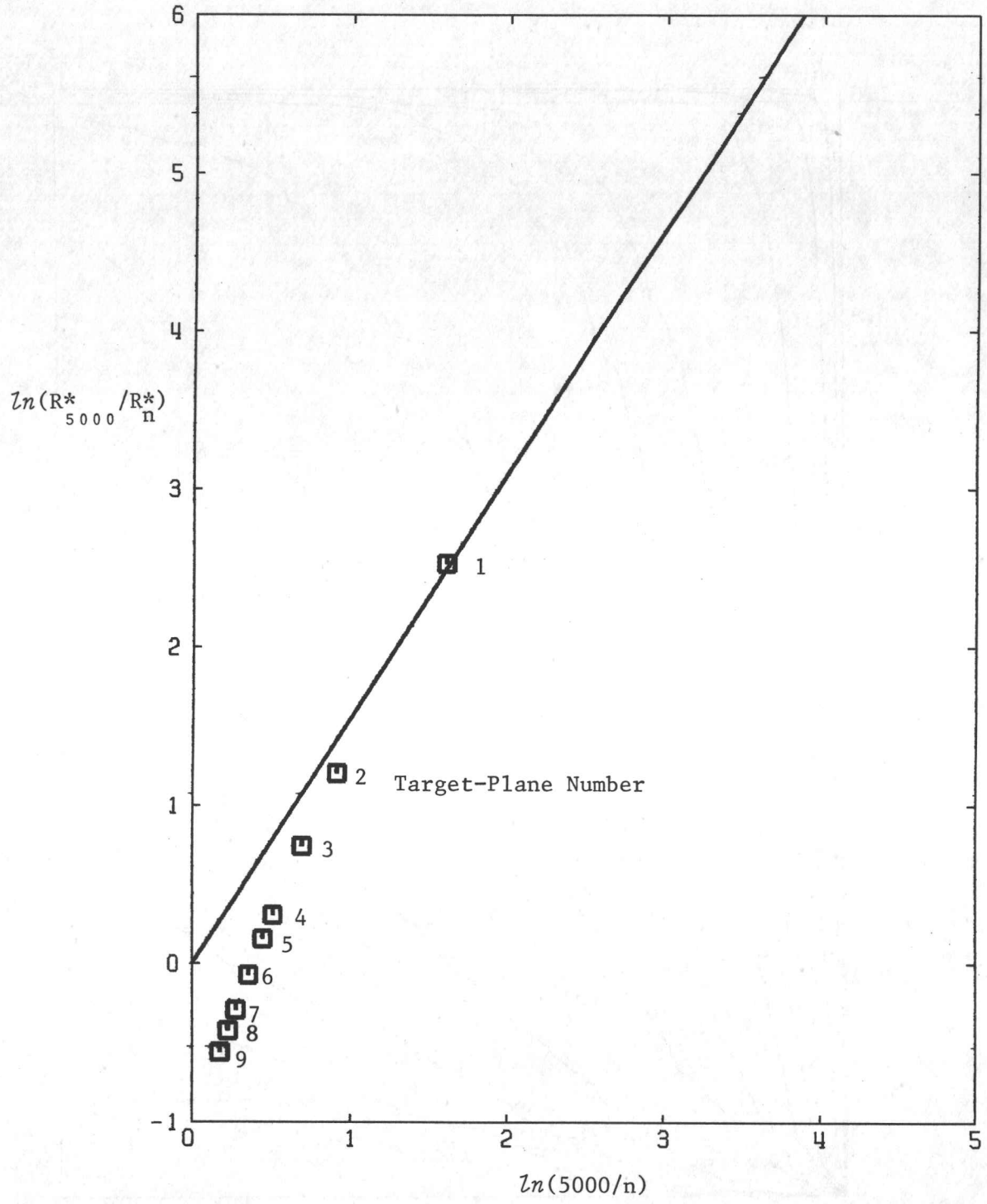

Fig. 29. Plot of the R values given by P(R) = 0.5 from the cumulative probability distributions for example 5. The straight line is the first-order, least-squares best fit of Eq. 2.34.

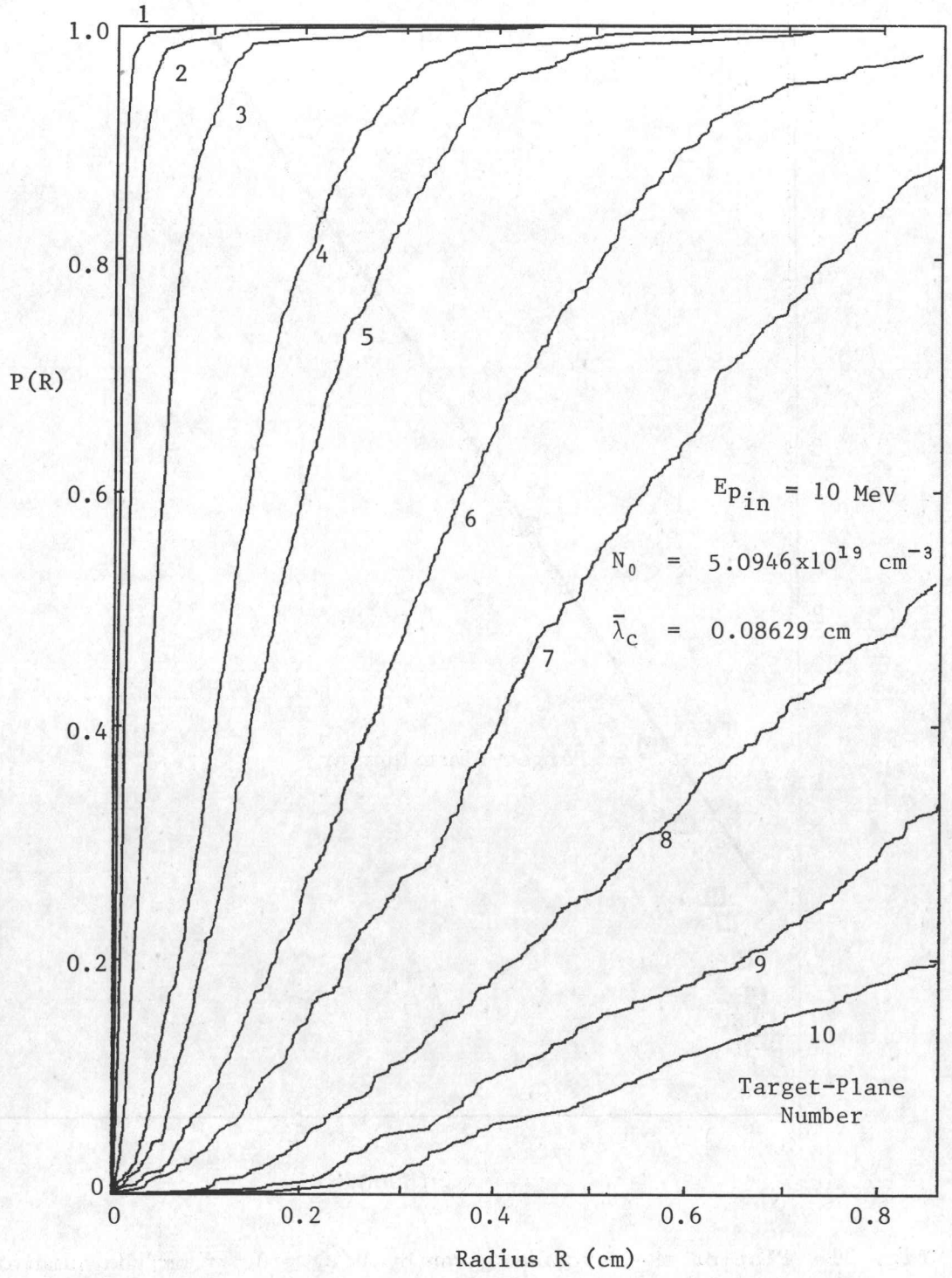

Fig. 30. Cumulative probability distributions generated by the Monte Carlo simulation for example 6. The numbered distributions correspond to target planes at increasing distances away from the point source (see the table in the text).

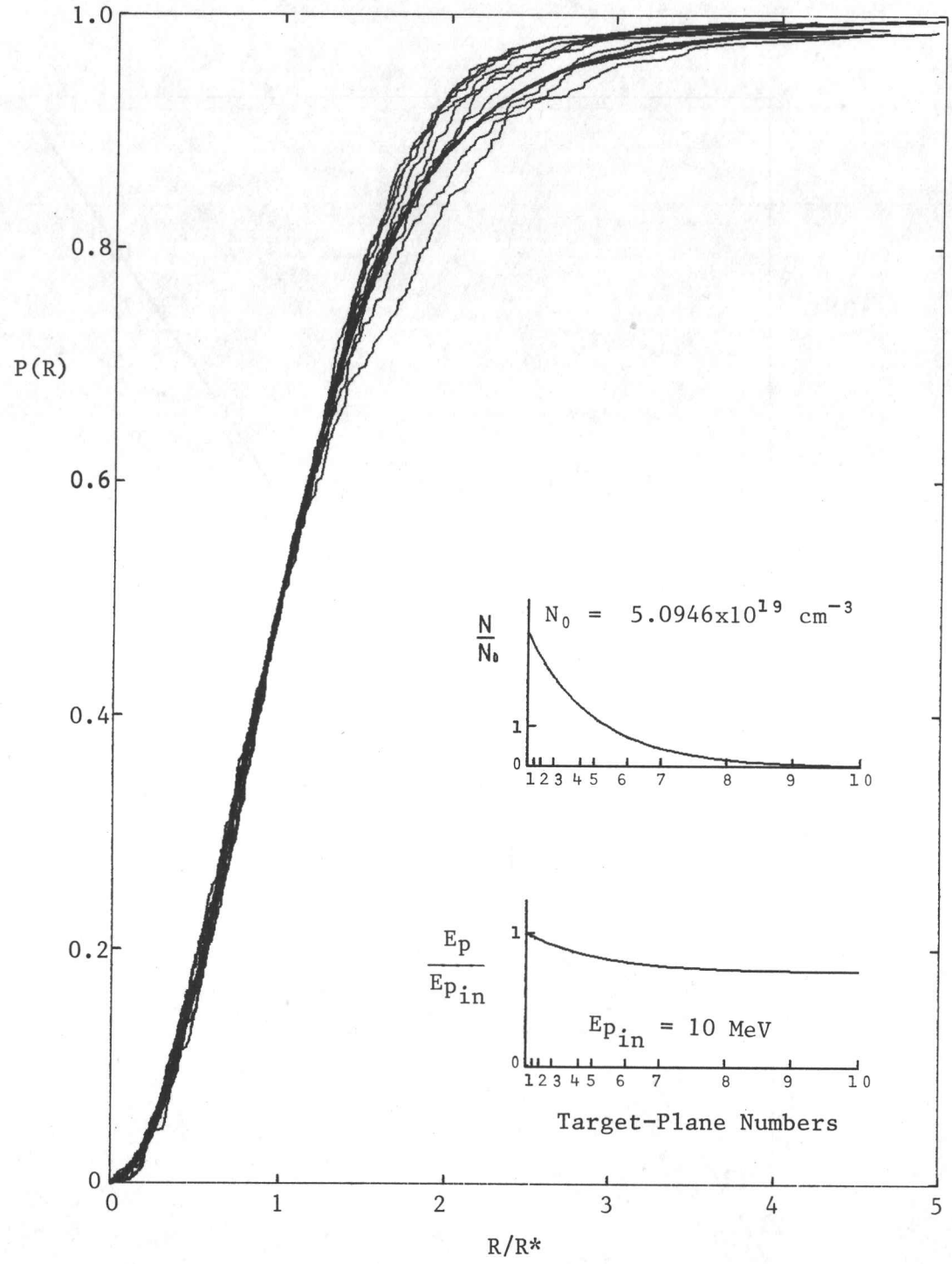

Fig. 31. Scaled cumulative probability distributions for example 6, to illustrate the self similarity of the successive distributions at increasing distances from the point source. The distribution indicated by the thickest line is the reference distribution obtained in example 1. This illustrates that similarity between the distributions exists for examples 1 and 6.

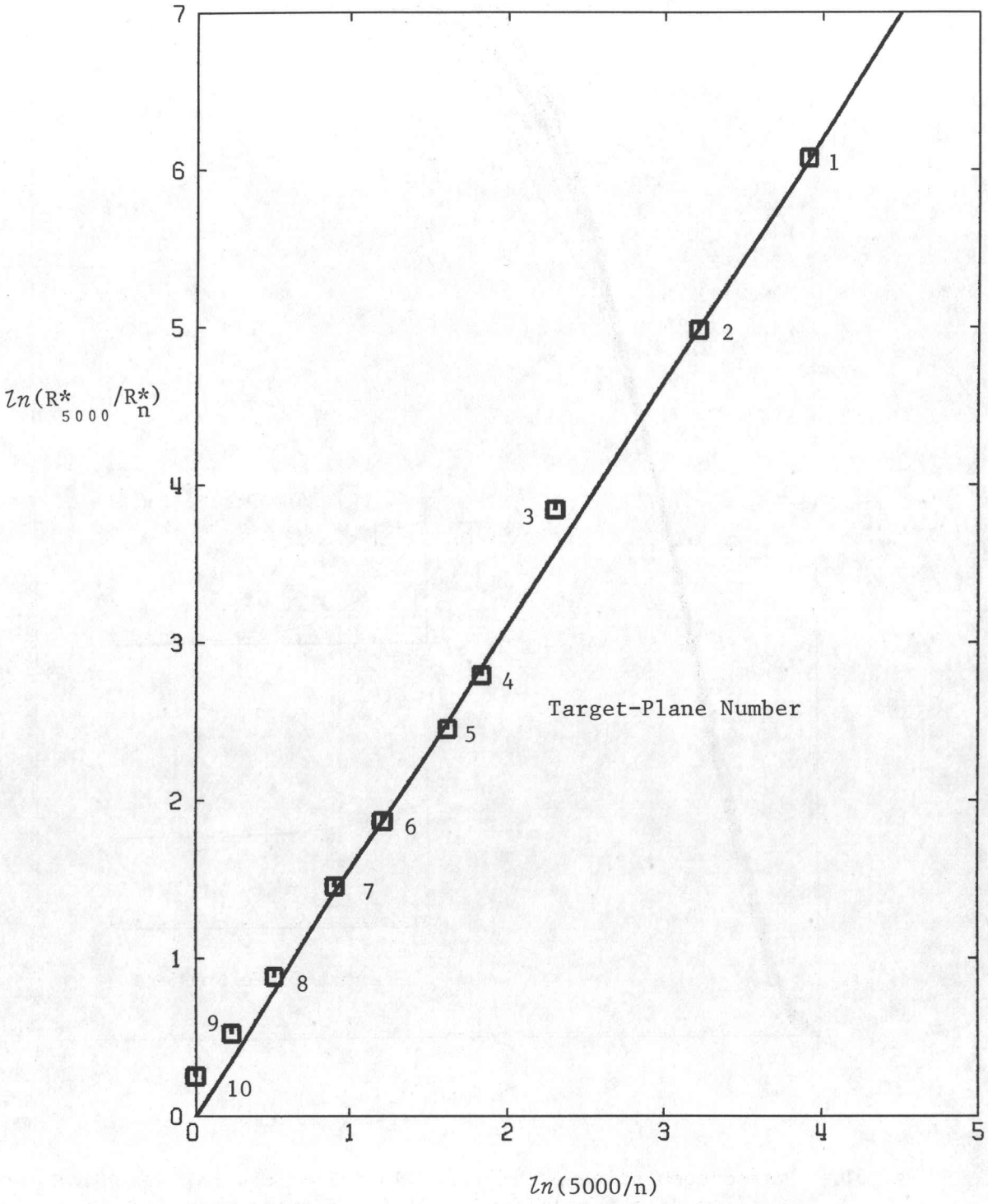

Fig. 32. Plot of the R values given by P(R) = 0.5 from the cumulative probability distributions for example 6. The straight line is the first-order, least-squares best fit of Eq. 2.34.

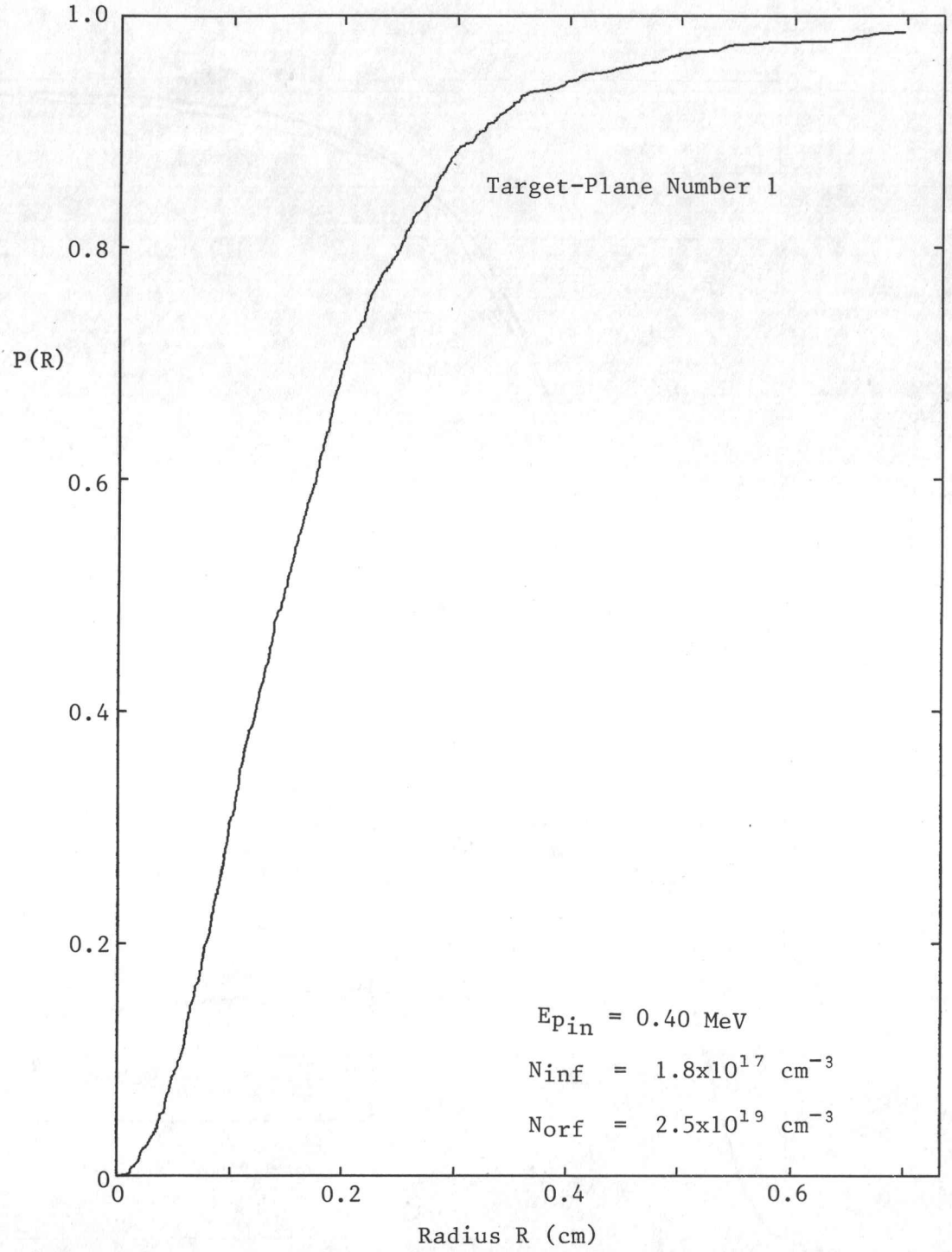

Fig. 33. Cumulative probability distribution generated by the Monte Carlo simulation for example 7. The target plane is situated at a 2 cm orifice that is 100 cm away from the point source.

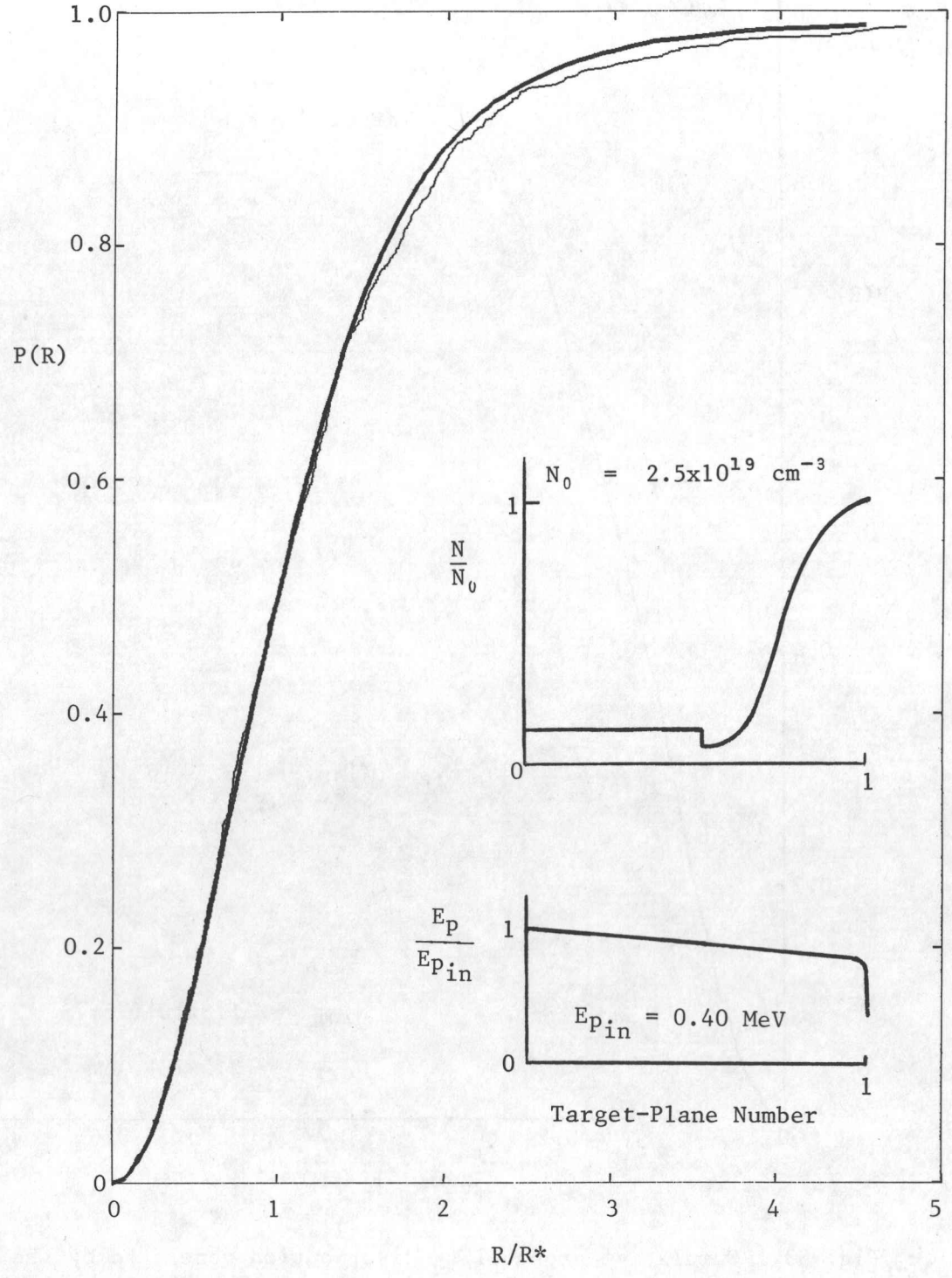

Fig. 34. Scaled cumulative probability distribution for example 7, to illustrate that similarity between the distributions exists for examples 1 and 7. The distribution indicated by the thickest line is the reference distribution obtained in example 1.

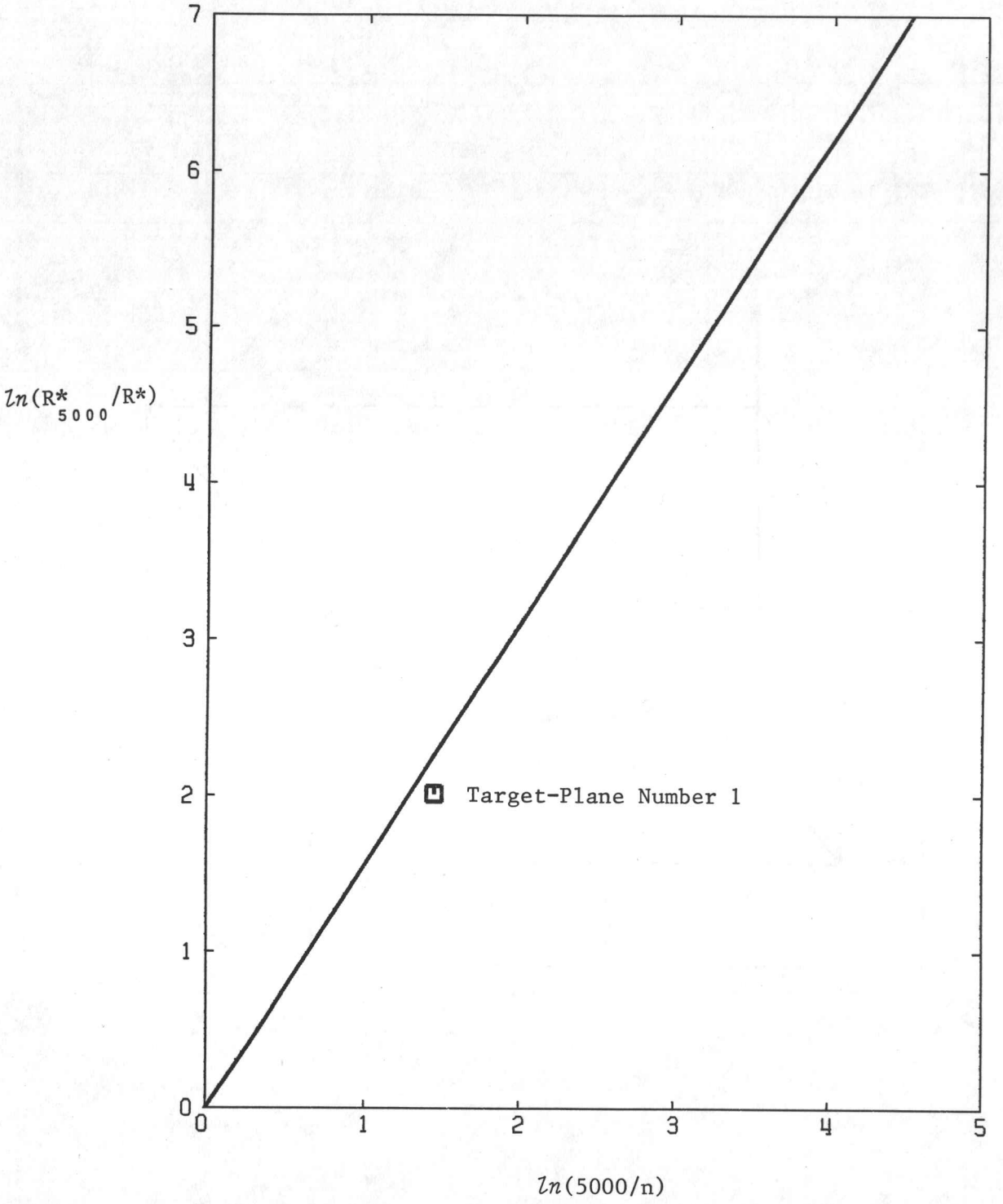

Fig. 35. Plot of the R value given by P(R) = 0.5 from the cumulative probability distribution for example 7. The straight line is the first-order, least-squares best fit given by Eq. 2.34.

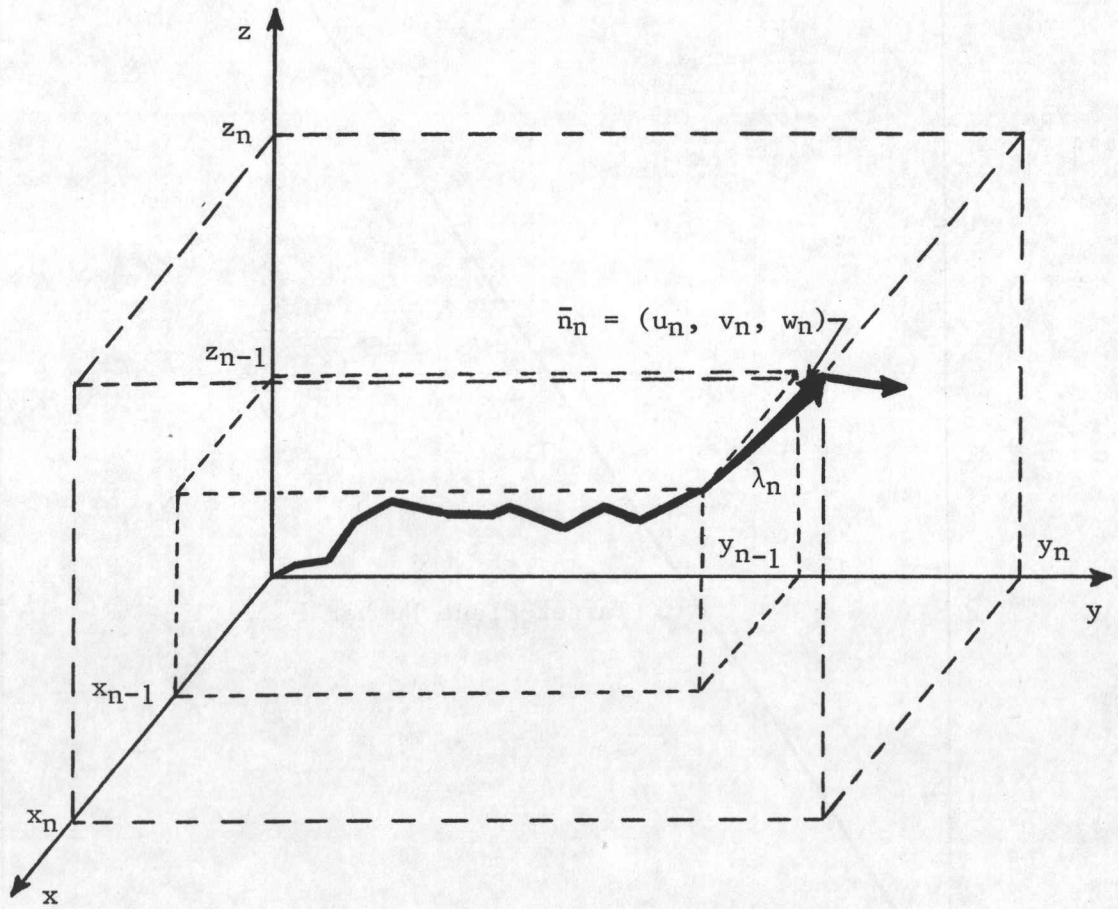

Fig. 36. Illustration of the step increments in the particle path that lead to the current cumulative displacement of the ion.

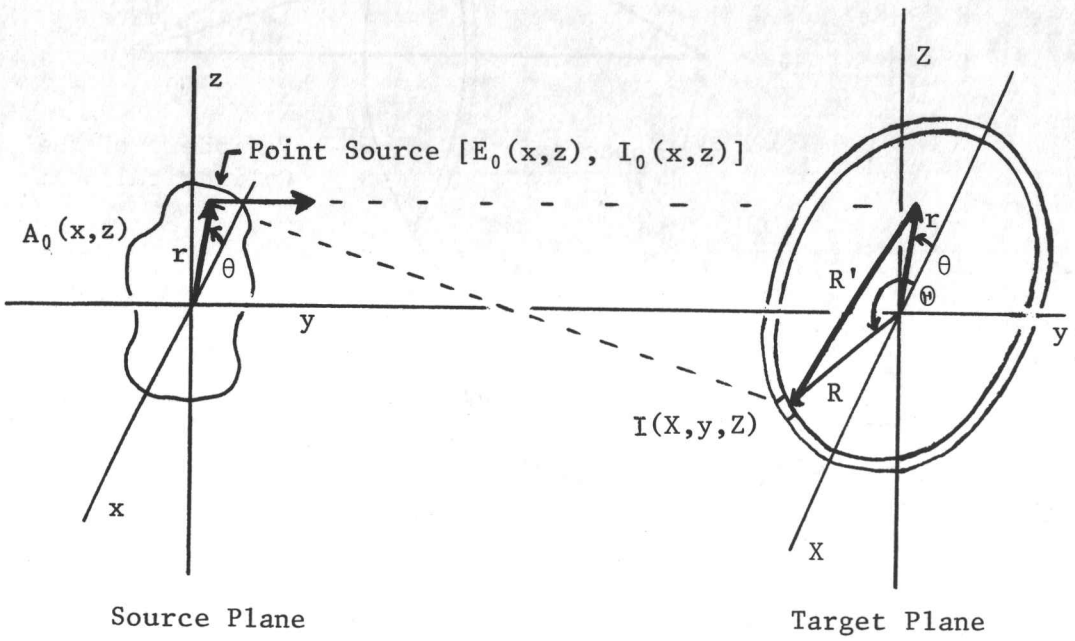

Fig. 37. Illustration of the intensity I(X,y,Z) experienced at the point (R,Θ) or (X,y,Z) in the target plane from a point source of initial intensity $I_0(x,z)$ and initial energy $E_0(x,z)$ at the point (r,θ) or (x,0,z) in the source plane of the ion beam of initial area $A_0(x,z)$.

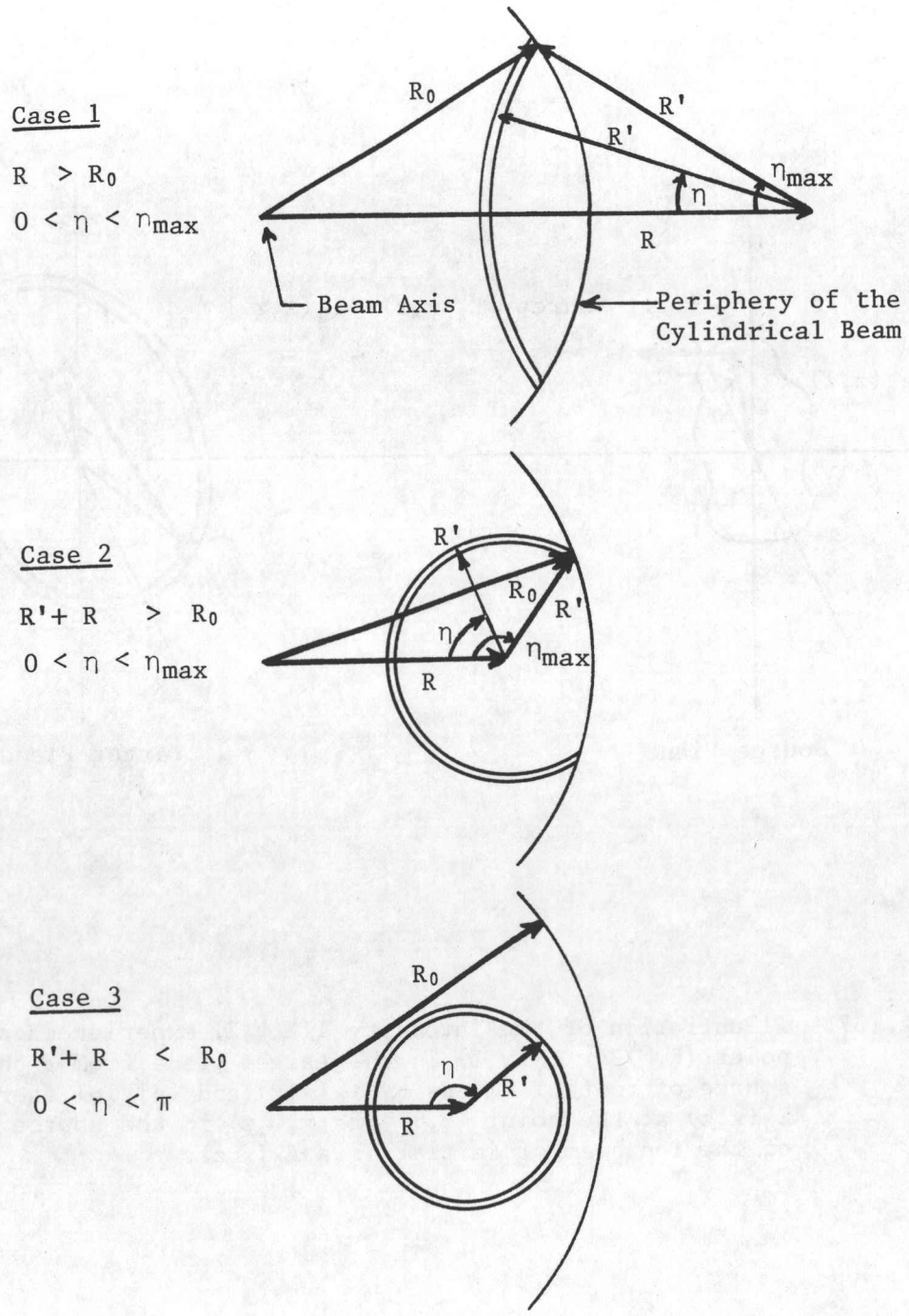

Fig. 38. Three different geometries that need to be considered for the integration of Eq. 4.8. In each case the range of η can be limited to positive angles because of symmetry.

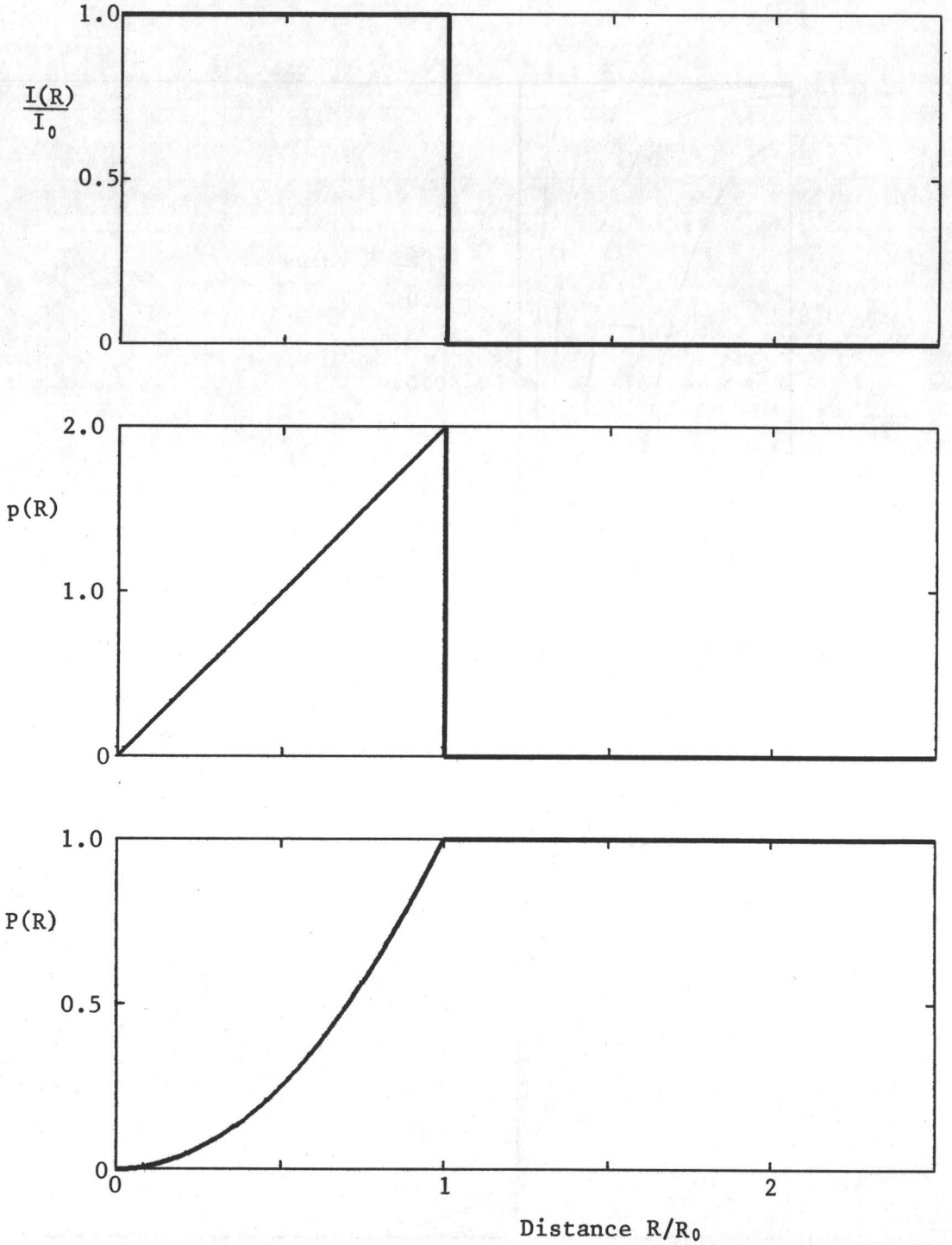

Fig. 39. Initial intensity, probability density, and cumulative probability distributions for a cylindrical ion beam at the source plane, where the beam radius is R_0 and the ion intensity and energy are constant over the ion beam cross section.

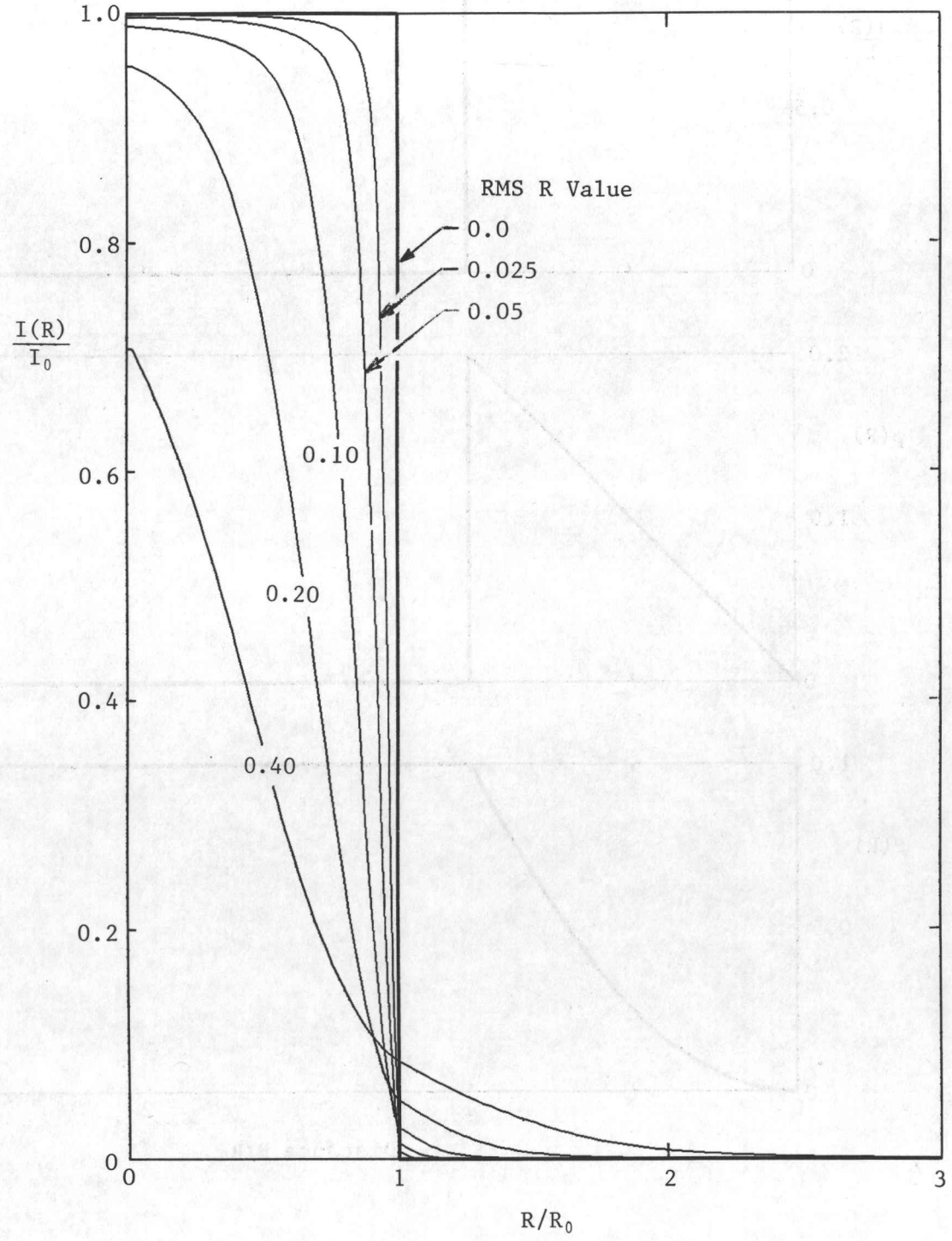

Fig. 40. Illustration of how the intensity distribution of a finite-sized ion beam changes shape with distance from the source plane.

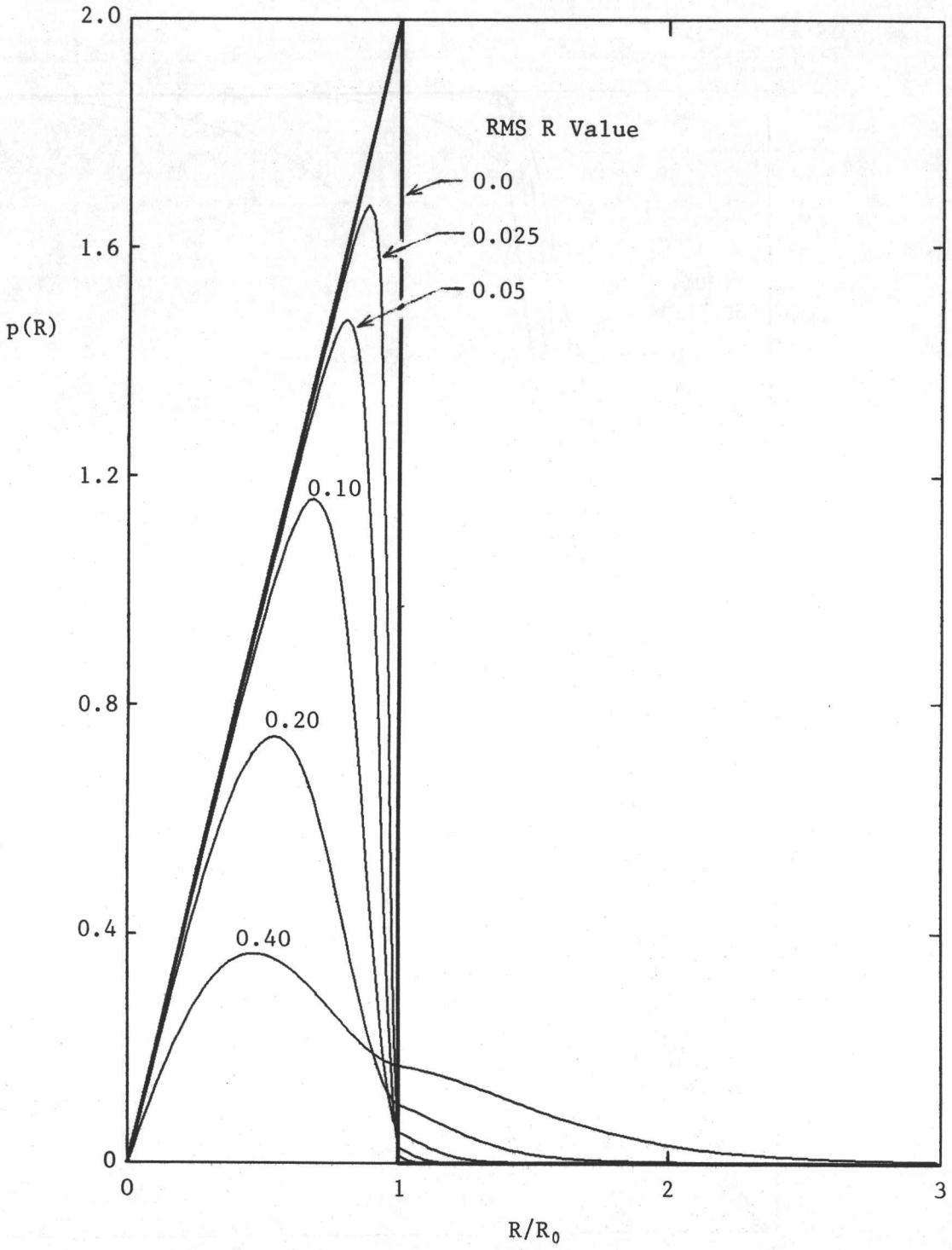

Fig. 41. Illustration of how the probability density distribution of a finite-sized ion beam changes shape with distance from the source plane.

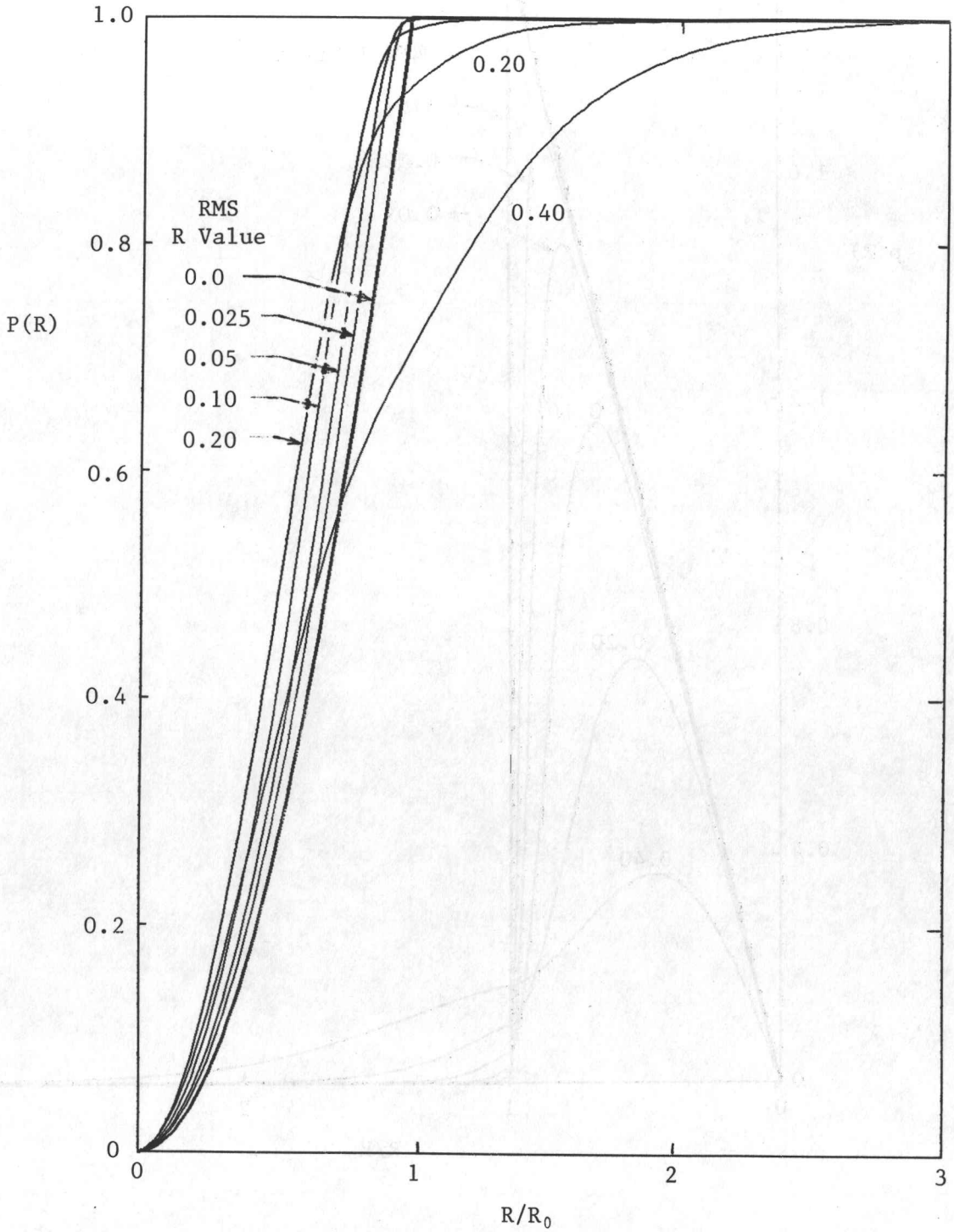

Fig. 42. Illustration of how the cumulative probability distribution of a finite-sized ion beam changes shape with distance from the source plane.

APPENDIX A

FREE PATH LENGTH BETWEEN COLLISIONS FOR THE MONTE CARLO METHOD

In all Monte Carlo simulations of a particle travelling through a scattering medium an important part of the algorithm is the calculation of the free path length between consecutive collisions. For realistic simulations, this path length must be allowed to vary about some mean value, the so-called mean free path, according to some probability density function that is based on the physics of the collision process.

Consider a beam of monoenergetic particles that penetrates a scattering medium. If N is the number density of the scattering medium, Q the total collision cross section of individual scatterers, n the number density of the incident beam particles that have not undergone a collision, and y the distance in the direction of the beam into the scattering medium, then the attenuation law for unscattered particles is [1]

$$-dn/n = QN\,dy. \tag{1}$$

If the number density N of the scattering medium is constant in this differential expression, integration from zero to y yields

$$n/n_0 = \exp(-QNy), \tag{2}$$

where $n = n_0$ at $y = 0$. However, for more general applications like those in the present work, the number density of the scattering medium must be allowed to vary with distance. Let the variation of the number density N in the direction of the incident particle beam be

$$N = N_0 f(y), \tag{3}$$

where f(y) is a dimensionless density profile. Further, let the particle be at a position $y = y_1$ within the scattering medium. The integral of Eq. 1 is now

$$\frac{n}{n_0} = \exp\left(-QN_0 \int_{y_1}^{y_1 + y} f(y')\,dy' \right), \tag{4}$$

where $n = n_0$ at $y = 0$.

The probability density function and its associated cumulative probability function can be obtained from Eq. 4. The right hand side of this equation can be interpreted as the probability density for which a particle experiences its first collision in the distance y to y + dy [1]. Hence, the normalized probability density function is

$$p(y) = QN_0\, f(y + y_1) \exp\left(-QN_0 \int_{y_1}^{y_1 + y} f(y')\,dy' \right). \tag{5}$$

The cumulative probability function P(y), defined as the integral of p(y)dy

from y_1 to $y_1 + y$, is

$$P(y) = \int_{y_1}^{y_1+y} QN_0\, f(y' + y_1) \exp\left(-QN_0 \int_{y_1}^{y_1+y'} f(y'')\, dy'' \right) dy' \quad . \qquad (6)$$

It represents the probability that the particle has experienced its first collision in the distance y or less. This distance is precisely the free path length of the particle from one collision to the next, and it is denoted by λ.

To calculate a specific free path length for the Monte Carlo simulation, a random number r is chosen from a uniform distribution of random numbers in the range of zero to unity. That value of r can then be assigned to either $P(\lambda)$ or $1 - P(\lambda)$, which both have the same range of zero to unity. Equation 6 can then be inverted to obtain an expression for the free path length λ,

$$r = \exp\left(-QN_0 \int_{y_1}^{y_1+\lambda} f(y')\, dy' \right) , \qquad (7)$$

or

$$\int_{y_1}^{y_1+\lambda} f(y')\, dy' = -\frac{1}{N_0 Q}\, ln(r) \quad , \qquad (8)$$

where the density variation $N_0 f(y)$ and the total collsion cross section, are specified. Equation 8 can be used to obtain values of the free path length for each random number r.

It is of interest to derive an expression for the mean free path length (or just the mean free path). The general definition of the mean free path is

$$\overline{\lambda} = \int_0^\infty y\, p(y)\, dy \, . \qquad (9)$$

By using Eq. 5, this expression can be rewritten as

$$\overline{\lambda} = \int_0^\infty QN_0\, f(y_1 + y)\, y \exp\left(-QN_0 \int_{y_1}^{y_1+y} f(y')\, dy' \right) dy \quad , \qquad (10)$$

which is still general. If the density N is constant [f(y) = 1], this integral can be integrated readily to yield

$$\overline{\lambda}_c = 1/N_0 Q, \qquad (11)$$

where the subscipt c denotes constant density. However, once N is allowed to vary, this integral becomes more difficult to evaluate analytically. For example, if N is simply equal to $N_0(1 + by)$, then Eq. 10 becomes

$$\overline{\lambda} = \int_0^\infty QN_0\, y\, [1 + b(y + y_1)] \exp\left(-QN_0\, [\, by^2/2 + y(1 + by_1)] \right) dy \quad . \qquad (12)$$

This expression was integrated numerically for numerous combinations of b and y_1, and it was found that a good approximation to the integral for this density variation is

$$\overline{\lambda} = \overline{\lambda}_c/(1 + by_1) . \qquad (13)$$

Further, it was found that this approximation is worst for small values of y_1 (of the order $\bar{\lambda}_c$) but becomes accurate very rapidly as y_1 increases and the density variation over a mean free path becomes smaller. For example, when $b = 1/\bar{\lambda}_c$, then at $y = 0$ the approximation of Eq. 13 is in error by 65 percent, but when $y = 10\bar{\lambda}_c$ the error decreases to less than 1 percent. The approximation given by Eq. 13 is expected intuitively. When the density does not change substantially over a distance of one collision, one might expect that the mean free path would be inversely proportional to the density, or depend on the local value of the density.

It should be noted that the energy E of the particle (and therefore Q) is kept constant over the entire range of the integration indicated in Eqs. 1 and 9, because a particle loses energy only during the collision process. Futhermore, the energy E at the point y_1 must be used when calculating λ, because Q is in general a function of the energy of the incident particle. For the particular problem of a high energy proton colliding with molecular hydrogen it was found in appendix B that

$$Q = \pi a_0^2 \left(\frac{m}{m_0}\right)^2 \frac{4 + 6E_x + 7E_x^2/3}{(1 + E_x)^3} , \tag{14}$$

which for high energies is approximated well by

$$Q = \pi a_0^2 \left(\frac{m}{m_0}\right)^2 \frac{7}{3E_x} . \tag{15}$$

In these expressions, a_0, m, m_0, and E_x denote the first Bohr orbit, the reduced mass, the mass of an electron, and the nondimensional energy. As the incident particle travels through the scattering medium and experiences collisions, it loses a discrete amount of energy at each collision. In the present work, the range-energy relationship of chapter 2 is used to describe the energy loss with distance. Therefore, after each collision, the reduced energy of the particle must be used in Eq. 15 to calculate the new total collision cross section for the next collision.

For density variations of interest in this work, the inversion of Eq. 8 can be done analytically. Some sample expressions for the free path length for particular density variations are summarized below.

Case 1. Constant Density: $N = N_0$ because $f(y) = 1$.

$$\lambda = -\bar{\lambda}_c \ln(r) \tag{16}$$

Case 2. Linear change in Density: $N = N_0(1 + by)$.

$$\lambda = \frac{1}{b}(1 + by_1)\left[\sqrt{1 - \frac{2b\,\bar{\lambda}_c \ln(r)}{(1 + y_1)^2}} - 1\right] \tag{17}$$

Case 3. Exponential change in Density: $N = N_0 \exp[a(y - y')]$.

$$\lambda = \frac{1}{a} \ln\left(1 - a\bar{\lambda}_c \ln(r) \exp\{a(y' - y_1)\}\right) \tag{18}$$

Reference

1. Cashwell, E. D. & C. J. Everett, "The Monte Carlo Method for Random Walk Problems", Vol. 1, Pergamon Press, 1959.

APPENDIX B

SCATTERING ANGLE FOR A HIGH-ENERGY PROTON COLLISION WITH MOLECULAR HYDROGEN

In all Monte Carlo simulations of particles moving through a scattering medium, an integral part of the computer program involves the selection of a scattering or deflection angle for each collision. This deflection must be sampled randomly from an appropriately weighted distribution of angles. To get this distribution, called the differential scattering cross section, four approaches are available, depending on the problem being considered. These approaches are:

a) classical mechanics,

b) exact quantum mechanical treatment (method of partial waves),

c) Born's expansion (integral scattering equation),

d) curve fit to experimental data.

The first and third approaches will be discussed in the following paragraphs. Note that the third approach is an approximation to the second, and the fourth requires extensive experimental data that is normally unavailable.

The interaction between two like charges (that are unscreened) is governed by Coulomb's potential equation,

$$V(r) = Z_1 Z_2 e^2 / r, \tag{1}$$

where Z_1 and Z_2 denote the charges on the two particles, e is the fundamental unit of charge, and r is the distance between the two charges. In a classical treatment, the scattering cross section for Coulomb's potential is [1]

$$I(\theta) = [Z_1 Z_2 e^2 / 8E] \csc^4(\theta/2), \tag{2}$$

which is known as Rutherford's scattering law, where E is the energy of the incident particle and θ is the scattering angle in the center-of-mass coordinate frame.

To determine the probability density function $p(\theta) = I(\theta)/Q$, the total cross section Q must be calculated. Q is given in general by

$$Q = \int_0^{2\pi} \int_0^{\pi} I(\theta) \sin(\theta) \, d\theta \, d\phi, \tag{3}$$

where ϕ is the azimuthal angle in the center-of-mass coordinate frame. When an expression for Q is derived for the Coulomb scattering cross section (Eq. 2), an infinitely large cross section is obtained. This renders the classical treatment of the problem of no use for realistic Monte Carlo calculations, and another approach must be sought.

The quantum mechanical approach for two particles in a central potential field V(r) leads to an integral scattering equation, if only asymptotic behaviour is considered. However, by simple iteration of the integral scattering equation the Born expansion can be obtained. In the use of this expansion the number of terms of the expansion retained determines the accuracy of the solution. Born's first approximation for the differential scattering cross section of a central potential field V(r) is given by [2]

$$I(\theta) = \frac{4m^2}{\hbar^4 K^2} \left| \int_0^\infty \sin(Kr)\, V(r)\, r\, dr \right|^2, \qquad (4)$$

where K is the magnitude of the scattering wave vector, m is the reduced mass of the particles, and $\hbar = h/2\pi$ is the rationalized Planck constant. K is found by considering the triangle in figure 1. The cosine law yields

$$K^2 = k_i^2 + k_d^2 - 2k_i k_d \cos(\theta), \qquad (5)$$

where k_i is the magnitude of the incident wave vector, k_d is the magnitude of the scattered wave vector, and θ is the scattering angle. If an inelastic collision is considered, for which the incident particle loses a differential amount of energy dE, where

$$E = mv^2/2 = \hbar^2 k^2/2m \qquad (6)$$

with v being the speed of the incident particle, then k_i and k_d can be written as

$$k_i = k, \qquad k_d = k - dk, \qquad (7)$$

where

$$dk/k = dE/2E. \qquad (8)$$

The substitution of Eqs. 7 and 8 into Eq. 5 yields

$$K^2 = 2k^2 \left[\left(1 - \frac{dE}{2E}\right) 2\sin^2(\theta/2) + \frac{1}{8}\left(\frac{dE}{E}\right)^2 \right]. \qquad (9)$$

For high energies (i.e., $dE/E \ll 1$), expression 9 reduces to

$$K = 2k \sin(\theta/2) = (2mv/\hbar) \sin(\theta/2) \qquad (10)$$

which is the result for elastic collision scattering. In the present work the energy of the colliding particles is almost always large. Consequently, it is reasonable to ignore inelastic effects for simplicity, and Eq. 10 is used in lieu of Eq. 9. In typical Monte Carlo simulations in the present work, the energy was seldom less than 1 MeV, at which point dE/E is small at only 0.05.

It now remains to pick the potential V(r) for the present work. For a hydrogen atom, if the incident particle is an electron, V(r) is given exactly as [3]

$$V(r) = -e^2 \left[\frac{1}{r} + \frac{1}{a_0} \right] \exp\left(\frac{-2r}{a_0}\right), \qquad (11)$$

where $a_0 = \hbar^2/m_0e^2$ is the radius of the first Bohr electron orbit, and m_0 is the mass of the electron. This potential can be used, with a change in sign, for a high-energy proton colliding with a hydrogen molecule, because the interaction of the proton with the hydrogen molecule will be assumed to occur only between the proton and a single hydrogen atom. This assumption is valid because the distance between the atoms of the hydrogen molecule is larger than the impact parameter.

Born's approximation is valid for the range of scattering angles for which the following condition is satisfied [3],

$$Z = \frac{V(\hbar/mv\theta)}{mv^2\theta} << 1 , \tag{12}$$

where v is the velocity (magnitude) of the incident particle in the center-of-mass reference frame. For this particular potential, and for proton energies in the range 1 to 10 MeV, Born's approximation becomes inaccurate for angles smaller than about 10^{-5} radians. The validity of this approximation will be dicussed later, after an expression for θ has been developed.

The substitution of Eq. 11 in Eq. 4 yields

$$I(\theta) = \frac{m^2e^4}{\hbar^4} \frac{a_0^4}{4} \frac{[2 + (Ka_0/2)^2]^2}{[1 + (Ka_0/2)^2]^4} , \tag{13}$$

which in terms of E and θ becomes

$$I(\theta) = \left(\frac{m}{m_0}\right)^2 \frac{a_0^2}{4} \frac{[2 + (mE/m_0E_0)\sin^2(\theta/2)]^2}{[1 + (mE/m_0E_0)\sin^2(\theta/2)]^4} , \tag{14}$$

where m_0 is the mass of an electron and $E_0 = e^2/2a_0 = \hbar^2/2m_0e^2$ is a reference energy equal to the ionization potential of hydrogen (13.58 eV). A more suitable variable for use in this study can be defined as

$$x = \frac{m\,E}{m_0E_0} \sin^2(\theta/2) = E_x\sin^2(\theta/2) ; \tag{15}$$

where $E_x = mE/m_0E_0$. Therefore,

$$\begin{aligned} I(x) &= \left(\frac{m}{m_0}\right)^2 \frac{a_0^2}{4} \frac{[2 + x]^2}{[1 + x]^4} \\ &= \left(\frac{m}{m_0}\right)^2 \frac{a_0^2}{4} \left[\frac{1}{(1+x)^2} + \frac{2}{(1+x)^3} + \frac{1}{(1+x)^4} \right] . \end{aligned} \tag{16}$$

The normalized distribution of $I(\theta)$ [i.e., $I(\theta)/I(0)$] is shown in figure 2 for the specific case of E = 5 MeV.

The probability that a particular value of the scattering angle θ_i is less than or equal to θ defines a cumulative probability distribution.

Therefore,

$$P(\theta) = \frac{1}{Q}\int_0^{2\pi}\int_0^{\theta} I(\theta)\,\sin(\theta)\,d\theta\,d\phi. \tag{17}$$

For a proton collision with a hydrogen molecule,

$$Q = \pi a_0^2 \left(\frac{m}{m_0}\right)^2 \frac{4 + 6E_x + 7E_x^2/3}{(1 + E_x)^3}, \tag{18}$$

$$P(x) = \frac{x}{E_x}\,\frac{4 + 6x + 7x^2/3}{4 + 6E_x + 7E_x^2/3}\left[\frac{1 + E_x}{1 + x}\right]^3. \tag{19}$$

The dependence of Q on the energy E_x for the above expression is illustrated in figure 3.

The intent of the following work is to obtain an expression that relates the scattering angle θ (in the form of the variable x) to a particular probability P(x). In other words, a function is being sought such that

$$\theta = F(P\{x\}). \tag{20}$$

Manipulation of equation 19 to achieve this would be difficult, because x would appear in a cubic polynomial. An approximation to Eq. 16 is then sought such that, on integration to obtain expressions for Q and P(x), a quadratic polynomial in x is obtained. For this purpose assume an I(x) of the form

$$I(x) = \left(\frac{m}{m_0}\right)^2 \frac{a_0^2}{4}\left[\frac{A}{(1+Cx)^2} + \frac{B}{(1+Cx)^3}\right] \tag{21}$$

which leads to

$$Q = \pi a_0^2 \left(\frac{m}{m_0}\right)^2 \frac{A+B + C(A+B/2)E_x}{(1 + CE_x)^2}. \tag{22}$$

To determine the constants, consider the following limits of Eqs. 16, 18, 21, and 22:

As $x \to 0$: Eq. 16 = Eq. 21 gives $A + B = 4$

As $x \to \infty$: Eq. 16 = Eq. 21 gives $A = C^2$ (23)

As $E_x \to \infty$: Eq. 18 = Eq. 22 gives $A + B/2 = 7C/3$

The solutions for A, B, and C are

$$A = (62 - 7\sqrt{52})/9,$$

$$B = (7\sqrt{52} - 26)/9, \tag{24}$$

$$C = (14 - \sqrt{52})/6.$$

The negative root was chosen to achieve better agreement. A detailed comparison of Eqs. 16 and 21 for I(x) and Eqs. 18 and 22 for Q would show that the approximation was excellent (less than 1 percent difference), provided that $E_X > 100$. For protons colliding with hydrogen molecules this implies that $E > 0.01E_0$, which is satisfied for all problems in this work.

The solution for P(x), in terms of the constant C, is

$$P(x) = [D - F(x)]/[D - F(E_X)], \tag{25}$$

where

$$D = \frac{16}{(4 - C^2)^2}, \qquad F(z) = \left[\frac{C^2}{4 - C^2} + \frac{1}{1 + Cz} \right]^2, \tag{26}$$

These results yield

$$x = \frac{1}{C} \left[\frac{1}{\sqrt{D - P(x)(D - F(E_X)} + 1 - \sqrt{D}} - 1 \right] \tag{27}$$

for

$$E_X = \frac{m\,E}{m_0 E_0} >> 1, \tag{28}$$

which is a good approximation for the present work, the approximation for θ from Eq. 27 becomes,

$$\theta = 2\,\text{Arcsin} \left[\frac{1}{E_X C} \left(\frac{1 - C^2/4}{\sqrt{1 - P(x)(1 - C^4/16)} - C^2/4} - 1 \right) \right]^{\frac{1}{2}}. \tag{29}$$

This distribution is shown in figure 4 for E = 5 MeV. As can be seen from the figure, the scattering angles considered are indeed very small. This is characteristic of screened Coulomb scattering of a heavy particle for which the scattering is very strongly forward. For this particular energy, it is seen that 90 percent of the individual collisions produce a scattering angle of 200 microradians or less, and the average angle can be computed by assigning the value of 0.5 to P(x) in Eq. 29. In order to calculate an angle θ for Monte Carlo simulations, a random number is picked from a uniform distribution in the interval zero to unity. That value is assigned to P(x), which then permits the scattering angle θ to be calculated by Eq. 29 [4].

The table on the next page shows the average scattering angle for various energies, as well as the Born approximation validity coefficient Z from Eq. 12.

E (eV)	(P{x}=0.5)	Z
10^7	5×10^{-5}	0.07
5×10^6	7×10^{-5}	0.10
10^6	1.6×10^{-4}	0.20
5×10^5	2.2×10^{-4}	0.30

As can be seen from the Z values in the above table and Eq. 12 the validity of using the Born approximation in the present work is borderline. That is, although the average values of the scattering angle are above the threshold for validity, some scattering angles obtained from Eq. 29 will be smaller than this threshold value. However, even though the smallest angles will be in error, according to the cutoff equation (Eq. 12), this is not very significant, because small angles do not contribute markedly to the dispersion of a high-energy proton beam in molecular hydrogen. Hence, Born's first approximation is reasonable for the present purpose.

References

1. Goldstein, H., "Classical Mechanics", second Ed., Addison-Wesley, 1980.

2. Cohen-Tannoudji, C., B. Diu & F. Laloe, "Quantum Mecanics", Vol. 2, John Wiley and Sons, 1977.

3. Mott, N. F. & H. S. W. Massey, "The Theory of Atomic Collisions", third Ed., Oxford, 1965.

4. Cashwell, E. D. & C. J. Everett, "The Monte Carlo Method for Random Walk Problems", Vol. 1, Pergamon Press, 1959.

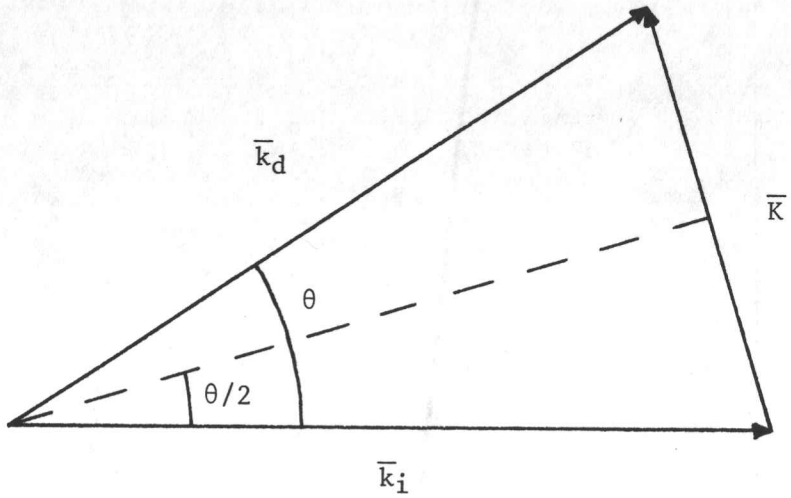

Figure 1. The geometrical relationship between the incident wave vector $\overline{k}_i$, deflected wave vector $\overline{k}_d$, deflecting wave vector $\overline{K}$, and the scattering angle θ.

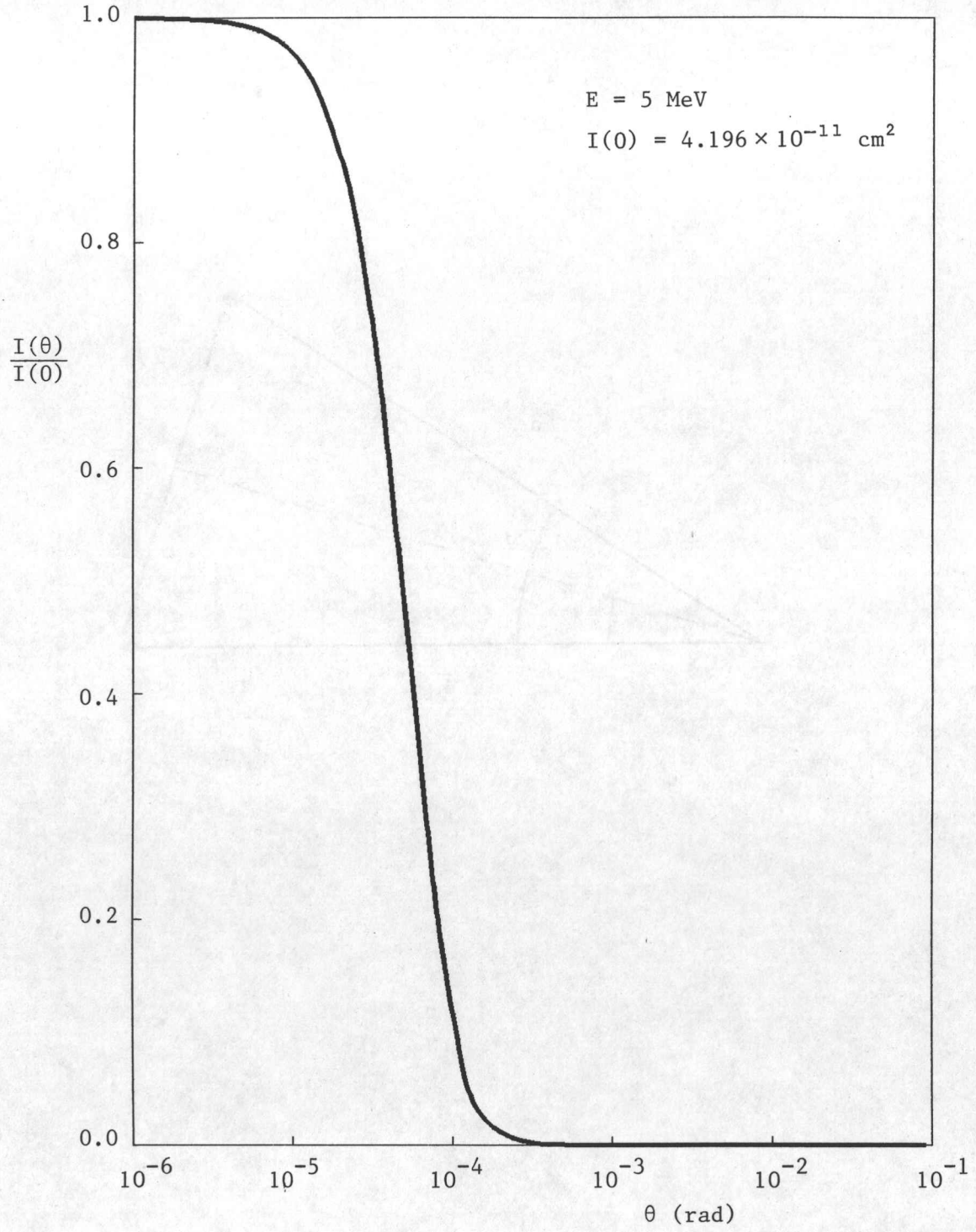

Figure 2. Normalized distribution of the differential scattering cross section for protons colliding with hydrogen molecules.

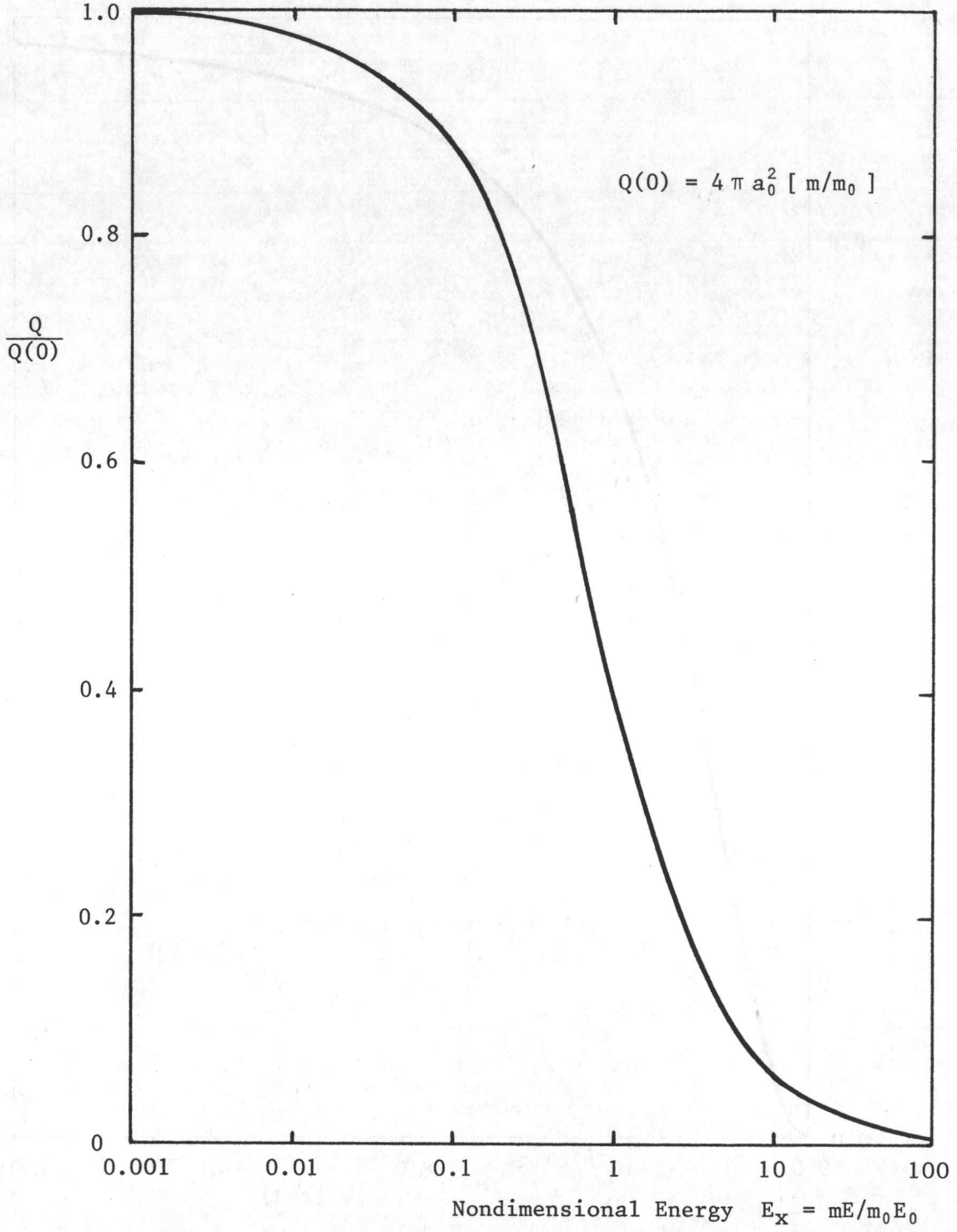

Figure 3. Normalized total scattering cross section Q as a function of the nondimensional energy E_x, for protons scattering in molecular hydrogen.

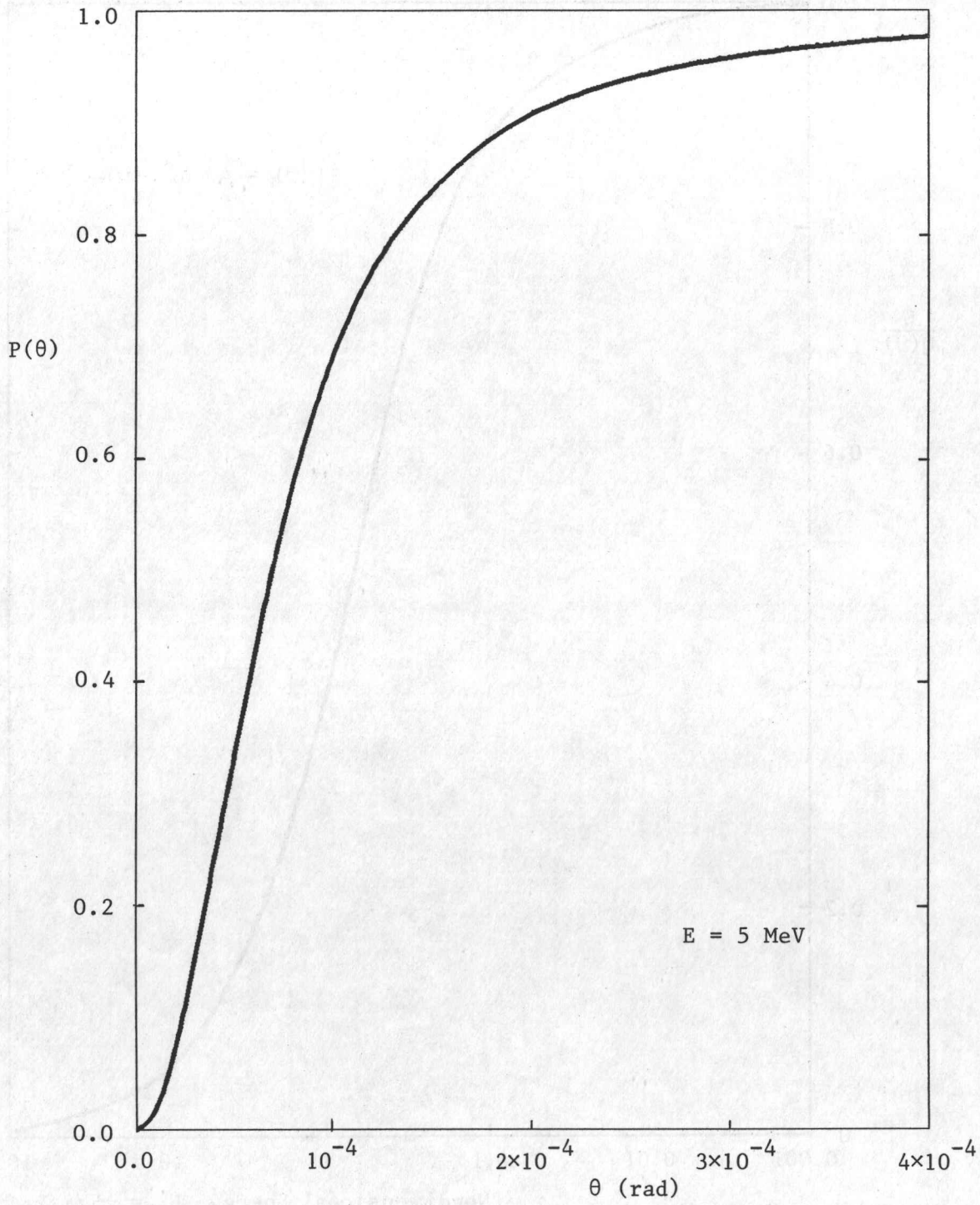

Figure 4. Cummulative probability function P(θ) as a function of θ for protons scattering in molecular hydrogen.

APPENDIX C

MONTE CARLO COMPUTER PROGRAM

```
C
C     BEAM DISPERSION PROGRAM BY T. W. CROUCH
C
C  PROGRAM COMPUTES BEAM DISPERSION FOR PROTONS IN MOLECULAR
C  HYDROGEN(H2)
C
C     CONTAINS : PROPER PHI AND THETA DISTRIBUTION
C              : CORRECT ENERGY LOSS ALONG PATH VIA STOPPING
C                 CROSS-SECTION
C              : CORRECT MEAN FREE PATH AS FUNCTION OF ENERGY
C
C    **********  LINEARLY DECREASING DENSITY GAS  **********
C
C    ***************** N = N0 (1 + B1*Y) ********************
C    ************* B1 = -1./(5000.*BARL1) *******************
C
C         CAPABLE OF TAKING DATA AT 10 Y VALUES
C
      IMPLICIT REAL (M-N)
      DOUBLE PRECISION SEED1,SEED2,SEED3
      DIMENSION XLCK(10),EAV(10)
      DATA XLCK/100.,200.,500.,1000.,2000.,3000.,
     .4000.,4500.,0000.,0000./
C
      LMAX=8
      ITOTP=500
C
C**** THE FOLLOWING MUST BE SATISFIED AS A MINIMUM
C                 XLCK(LMAX)...EAV(LMAX)
C
      PI=3.141592654
      SEED1=123456789.
      SEED2=6534721046.
      SEED3=9237750321.
C
      ME=1.
      MP=1836.11
      MH=2.*MP
      MR=(MP*MH)/(MP+MH)
C
C  ALL ENERGY VALUES ARE IN (EV)
C
      EP=1.E+07
      E0=EP
      ER=MP*EP/MR
      EX0=(MR*ER)/(ME*13.58)
```

```
C
C  COEFFICIENTS FOR CALCULATING THETA
C
      C=7./3.-SQRT(13.)/3.
      A=C*C
      B=4.-C*C
      C1=(1.+A/B)**2.
C
C  DENSITY DEFINITION (NO IS IN UNITS OF MOLECULES/CM**-3 FOR MOLEC-
C  ULAR HYDROGEN AND IN UNITS OF ATOMS/CM**-3 FOR ATOMIC HYDROGEN)
      NO=2.5473E19
      NO=NO*2.
      Q=PI*(5.29177E-9)**2.*(MR/ME)**2.*(4.+6.*EXO+7.*EXO**2/3.)
     ./(1.+EXO)**3.
      BARL1=1./(Q*NO)
      B1=-1./(5000.*BARL1)
C
      DO 20 I=1,LMAX
20    XLCK(I)=XLCK(I)*BARL1
      WRITE(6,*) EO,BARL1,ITOTP,LMAX,1.,B1,DUM1,' LINEAR'
      WRITE(6,*) (XLCK(LL),LL=1,LMAX)
      DO 7 I=1,ITOTP
C  *********  BEGIN NEW PARTICLE PATH  ************
      EX=EXO
      N=NO
      EP=EO
      L=1
      BARL=BARL1
      XO=0.
      ZO=0.
      YO=-BARL*ALOG(GGUBFS(SEED1))
C  GGUBFS IS AN IMSL SUBROUTINE THAT PRODUCES A UNIFORM
C  DISTRIBUTION OF RANDOM NUMBERS BETWEEN 0 AND 1.
      DY=YO
      NO1=0.
      NO2=1.
      NO3=0.
1        PH=PI*(1.-2.*GGUBFS(SEED2))
           R=GGUBFS(SEED3)
           C2=(A/B+1./(1.+C*EX))**2.
           XX=(1./(SQRT(C1*(1.-R)+R*C2)-A/B)-1.)/(C*EX)
           THCM=2.*ASIN(SQRT(XX))
         TH=ATAN(SIN(THCM)/(MP/MH+COS(THCM)))
      N11=SIN(TH)*COS(PH)
      N12=SIN(TH)*SIN(PH)
      N13=COS(TH)
C
C  CALCULATE NEW ENERGY
C
       E1=EP/1.E6
      IF(E1.LT.0.04) GOTO 2
         EIN=.512652E-1/E1**.5-.246743+.690572*E1**.5+.389733*E1
        GOTO 3
2        EIN=.294787E-2/E1**.5+.359963-1.84853*E1**.5+3.93144*E1
3      EPS=1./EIN*1.E-21
      N=NO*(1.+B1*YO)
```

```
      E1=E1-EPS*DY*N
      EP=E1*1.E6
      ER=MP*EP/MR
      EX=(MR*ER)/(ME*13.58)
C
C     CALCULATE NEW DIRECTION
C
      IF(N03.NE.1.) GOTO 4
      N1=N11
      N2=N12
      N3=N13
      GOTO 6
4        N1=(N11*N03*N01-N12*N02)/(1.-N03**2)**.5+N13*N01
         N2=(N11*N03*N02+N12*N01)/(1.-N03**2)**.5+N13*N02
         N3=-N11*(1.-N03**2)**.5+N03*N13
C
C    NEW POSITION
C
6     BARLC=-EP/E0*BARL1*ALOG(GGUBFS(SEED1))
      DY=1./B1*(1.+B1*Y0)*(SQRT(1.+2.*B1*BARLC/(1.+B1*Y0)**2.)-1.)
         X0=X0+DY*N1
         Y0=Y0+DY*N2
         Z0=Z0+DY*N3
      N01=N1
      N02=N2
      N03=N3
C
C DATA COLLECTION
C
      IF(Y0.LT.XLCK(L)) GOTO 1
       XP=X0-N1/N2*(Y0-XLCK(L))
       ZP=Z0-N3/N2*(Y0-XLCK(L))
       YP=XLCK(L)
      WRITE(6,*) (XP*XP+ZP*ZP)**.5,EP
      EAV(L)=EAV(L)+EP
      L=L+1
      IF(L.GT.LMAX) GOTO 7
      GOTO 1
7     CONTINUE
      DO 11 L=1,LMAX
11    EAV(L)=EAV(L)/ITOTP
      WRITE(6,*) (EAV(LL),LL=1,LMAX)
      STOP
      END
```

APPENDIX D

CALCULATION OF THE EXPECTED VALUES OF THE FREE PATH LENGTH AND ITS SQUARE

The root-mean-square value of the lateral dispersion R of a molecular beam, given by Eq. 3.19 of chapter 3, involves the expected value of the square of the scattering angle, the expected value of free path length between collisions, and the expected value of the square of the free path length. For high-energy protons colliding with molecular hydrogen, these expected values can be obtained as a function of the penetration distance y, the energy E of the collision, or some combination of both. In this appendix the expected values of the free path length and the square of the free path length will be obtained as functions of both the energy of the collision and the depth of penetration, leaving the calculation of the expected value of the square of the scattering angle for appendix E.

The expected value of the free path length is defined to be [1]

$$E\{\lambda\} = \int_0^\infty p(y)\, y\, dy\,, \tag{1}$$

where the origin of y is defined to be y_1 (the current position of the incident particle). The probability density function p(y) is defined in appendix A as

$$p(\lambda) = QN_0\, f(y_1+\lambda)\, \exp\left[-QN_0 \int_{y_1}^{y_1+\lambda} f(y')\, dy'\right], \tag{2}$$

where the total collision cross section is

$$Q = \frac{7\pi a_0^2}{3E_x}\left(\frac{m}{m_0}\right)^2 \tag{3}$$

and the number density is defined quite generally as

$$N(y) = N_0 f(y).$$

If the particle is at the position $y = y_1$ in the density field, then Eq. 1 becomes

$$E\{\lambda\} = QN_0 \int_0^\infty f(y_1+y)\, y \exp\left[-QN_0 \int_{y_1}^{y_1+y} f(y')\, dy'\right] dy\,. \tag{5}$$

It should be noted that Q is held constant during the integration, because the particle does not lose energy between collisions.

The expected value of the square of the free path length is defined,

similarly, to be

$$E\{\lambda^2\} = \int_0^\infty y^2\, p(y)\, dy\,, \tag{6}$$

which then becomes

$$E\{\lambda^2\} = QN_0 \int_0^\infty f(y+y_1)\, y^2 \exp\left[-QN_0 \int_{y_1}^{y_1+y} f(y')\, dy'\right] dy\,. \tag{7}$$

Equations 5 and 7 can be evaluated numerically to obtain solutions for $E\{\lambda\}$ and $E\{\lambda^2\}$. However, this technique is cumbersome when it is necessary to evaluate the two integrals for numerous positions and energies. It is beneficial, therefore, to develop fairly simple approximate analytical expressions for these integrals, which are still accurate and can be used more readily.

If the density N is assumed to be constant [i.e., f(y) = 1], the average or mean free path then reduces to the expression commonly found and used in the literature [1], that is,

$$E\{\lambda\} = \int_0^\infty QN_0\, y \exp(-QN_0 y)\, dy\,. \tag{8}$$

The expected value of the square of the free path length from Eq. 7 is

$$E\{\lambda^2\} = \int_0^\infty QN_0\, y^2 \exp(-QN_0 y)\, dy\,. \tag{9}$$

These two integrals can be evaluated analytically to give

$$E\{\lambda\} = 1/QN_0, \tag{10}$$

and

$$E\{\lambda^2\} = 2/(QN_0) = 2\, E^2\{\lambda\}. \tag{11}$$

For this simple case of constant density, no approximation is necessary. It is also seen from Eqs. 10 and 11 that the expected value of only the first power of the free path length needs to be determined because the second power (and any subsequent power) can be obtained from the first. Further, because the particle is losing energy after each collision as it traverses the medium, $E\{\lambda\}$ depends on the local value of the energy. This dependence on energy in Eqs. 10 and 11 is through Q, which is inversely proportional to E (see Eq. 3). By taking this into account, Eqs. 10 and 11 can be written more conveniently as

$$E\{\lambda\} = E_0\{\lambda\}\, E/E_0, \tag{12}$$

and

$$E\{\lambda^2\} = 2\, E^2\{\lambda\}, \tag{13}$$

where the subscript $_0$ denotes the initial values of E and $E\{\lambda\}$ when the particle is at the position y = 0.

Consider now a linear density distribution of the form

$$N(y) = N_0(1 + by). \tag{14}$$

Equations 5 and 7 then become

$$E\{\lambda\} = QN_0 \int_0^\infty \left[1 + b(y+y_1)\right] y \exp\left[-QN_0\left(by^2/2 + y[1+y_1]\right)\right] dy \tag{15}$$

and

$$E\{\lambda^2\} = QN_0 \int_0^\infty \left[1 + b(y+y_1)\right] y^2 \exp\left[-QN_0\left(by^2/2 + y[1+y_1]\right)\right] dy, \tag{16}$$

which are considerably more difficult to evaluate analytically. They can, however, be evaluated numerically for a wide range of y_1 and b to determine their behaviour, so that approximate expressions can be developed and checked. When this was done for the linear density distributions of this work, it was found that

$$E\{\lambda\} = E_0\{\lambda\} \frac{N(0)}{N(y_1)} \frac{E}{E_0} \tag{17}$$

and

$$E\{\lambda^2\} = 2\, E^2\{\lambda\} \tag{18}$$

were good approximations. These approximate expressions were found to be accurate (within 1%) for all linear density variations considered in this work. Equations 17 and 18 are also very accurate even for linear variations in which $b = 1/E_0\{\lambda\}$, provided that y_1 is greater than $10E_0\{\lambda\}$. This implies that the numerical integration can be dispensed with for the cases of all practical linear density variations, and the local values can be used in their place.

For an exponential density variation with

$$N(y) = N_0 \exp[a(y - y')], \tag{19}$$

the approximations for Eqs. 5 and 7 become somewhat more complicated. The full integral expressions are

$$E\{\lambda\} = QN_0 \int_0^\infty \exp[a(y-y')]\, y \exp\left[\frac{-QN_0}{a} \exp[a(y_1 - y')]\left[\exp(ay) - 1\right]\right] dy \tag{20}$$

and

$$E\{\lambda^2\} = QN_0 \int_0^\infty \exp[a(y-y')]\, y^2 \exp\left[\frac{-QN}{a} \exp[a(y_1 - y')]\left[\exp(ay) - 1\right]\right] dy, \tag{21}$$

which are not integrable analytically. Equation 20 was found to follow

$$E\{\lambda\} = E_0\{\lambda\} \exp(-2ay_1) \tag{22}$$

fairly accurately for a wide range of a and y′. However, the expression for $E\{\lambda^2\}$ deviates from the previously found behaviour (Eqs. 11 and 18), but this

can be remedied by inserting a simple multiplicative factor. It was found that $E\{\lambda^2\}$ can be given by

$$E\{\lambda^2\} = 2E^2\{\lambda\} \exp(ay_1) \qquad (23)$$

for all of the exponential density variations considered in this work.

The use of approximations for $E\{\lambda\}$ and $E\{\lambda^2\}$ of Eqs. 5 and 7 instead of numerical integrations is not, of course, necessary. However, when approximations are both simple and sufficiently adequate, as they are in this work, their use is highly beneficial in reducing computation time and cost.

Reference

1. Cashwell, E. D. & C. J. Everett, "The Monte Carlo Method for Random Walk Problems", Vol. 1, Pergamon Press, 1959.

APPENDIX E

CALCULATION OF THE EXPECTED VALUE OF THE SQUARE OF THE SCATTERING ANGLE

The root-mean-square value of the lateral dispersion R of a molecular beam, given by Eq. 3.19 of chapter 3, involves both the expected value of the square of the scattering angle and the expected value of the free path length between collisions. For high-energy protons colliding with molecular hydrogen, these expected values can be obtained as a function of the penetration distance y, the energy of the collision E, or some combination of both. In this appendix the expected value of the square of the scattering angle will be obtained as a function of the energy of the collision.

The expected value of the square of the scattering angle θ is defined to be [1]

$$E\{\theta^2\} = \frac{1}{Q} \int_0^{2\pi} \int_0^{\pi} \theta^2 \, I(\theta,\phi) \, \sin(\theta) \, d\theta \, d\phi \, , \tag{1}$$

which for a central potential reduces to

$$E\{\theta^2\} = \frac{2\pi}{Q} \int_0^{\pi} \theta^2 \, I(\theta) \, \sin(\theta) \, d\theta \, . \tag{2}$$

From appendix B the differential scattering cross section $I(\theta)$ for the collision of a high-energy proton with molecular hydrogen is

$$I(x) = \left(\frac{m}{m_0}\right)^2 \frac{a_0^2}{4} \left[\frac{1}{(1+x)^2} + \frac{2}{(1+x)^3} + \frac{1}{(1+x)^4} \right] , \tag{3}$$

where

$$x = \frac{m\,E}{m_0 E_0} \sin^2(\theta/2) = E_x \sin^2(\theta/2) \, , \tag{4}$$

and

$$Q = \frac{7\pi a_0^2}{3\,E_x} \left(\frac{m}{m_0}\right)^2 \tag{5}$$

for $E_x >> 1$. The substitution of Eqs. 3 and 4 into Eq. 2 yields

$$E\{\theta^2\} = \frac{4\pi}{Q}\left(\frac{m}{m_0}\right)^2 \frac{a_0^2}{E_x} \int_0^{E_x} \arcsin^2\left(\frac{x}{E_x}\right) \left[\frac{1}{(1+x)^2} + \frac{2}{(1+x)^3} + \frac{1}{(1+x)^4} \right] dx \tag{6}$$

which cannot be integrated analytically. This integral can be solved numerically to give $E\{\theta^2\}$ as a function of E . However, in the present work it was found preferable to evaluate this integral by an approximate but highly accurate method. The procedure and results are given below.

Let the integration be divided into two parts, one covering small angles of θ and the other covering large angles. Then the total integral will be the sum of the two parts, that is,

$$E\{\theta^2\} = E_s\{\theta^2\} + E_\ell\{\theta^2\}, \tag{7}$$

where

$$E_s\{\theta^2\} = \frac{4\pi}{Q}\left(\frac{m}{m_0}\right)^2 \frac{a_0^2}{E_x} \int_0^{x^*} \arcsin^2\left(\frac{x}{E_x}\right)\left[\frac{1}{(1+x)^2} + \frac{2}{(1+x)^3} + \frac{1}{(1+x)^4}\right] dx \tag{8}$$

for small angles of θ for which $x^*/E_x \ll 1$, and

$$E_\ell\{\theta^2\} = \frac{4\pi}{Q}\left(\frac{m}{m_0}\right)^2 \frac{a_0^2}{E_x} \int_{x^*}^{E_x} \arcsin^2\left(\frac{x}{E_x}\right)\left[\frac{1}{(1+x)^2} + \frac{2}{(1+x)^3} + \frac{1}{(1+x)^4}\right] dx \tag{9}$$

for large angles of θ for which $x^* \gg 1$.

Consider Eq. 8 first. For this case it is assumed that $x^*/E_x \ll 1$; therefore,

$$\arcsin\left(\frac{x}{E_x}\right) \cong \frac{x}{E_x} \tag{10}$$

is a good approximation. The integral equation then simplifies to

$$E_s\{\theta^2\} = \frac{4\pi}{Q}\left(\frac{m}{m_0}\right)^2 \frac{a_0^2}{E_x^2} \int_0^{x^*} x\left[\frac{1}{(1+x)^2} + \frac{2}{(1+x)^3} + \frac{1}{(1+x)^4}\right] dx, \tag{11}$$

which is now integrable. The final result is

$$E_s\{\theta^2\} = \frac{4\pi}{Q}\left(\frac{m\,a_0}{m_0 E_x}\right)^2 \left[\ell n(x^*) + \frac{1}{6}\right], \tag{12}$$

which is obtained quite readily.

Now consider Eq. 9. For this case it is assumed that $x^* \gg 1$ and $x^*/E_x < 1$. Therefore, the cubic and quartic terms in the sum can be neglected in comparison with the dominant quadratic term. Equation 9 is then

$$E_\ell\{\theta^2\} = \frac{4\pi}{Q}\left(\frac{m}{m_0}\right)^2 \frac{a_0^2}{E_x} \int_{x^*}^{E_x} \arcsin^2\left(\frac{x}{E_x}\right) \frac{1}{x^2}\, dx. \tag{13}$$

With the change of variable given by

$$x = E_x \sin^2(y), \tag{14}$$

Eq. 13 can be integrated to give

$$E_\ell\{\theta^2\} = \frac{4\pi}{Q}\left(\frac{m\,a_0}{m_0 E_x}\right)^2 \left[3 - \frac{\pi^2}{4} + \ell n(E_x/x^*)\right], \tag{15}$$

if one remembers that $x^* \gg 1$.

To obtain the expected value of the scattering angle, Eqs. 12 and 15 must be added. The final result is

$$E\{\theta^2\} = \frac{4\pi}{Q}\left(\frac{m\,a_0}{m_0 E_x}\right)^2\left[\ln(E_x) + 3 + \frac{1}{6} - \frac{\pi^2}{4}\right]. \tag{16}$$

The constants in the square bracket have not been omitted in Eq. 16 because, even though E_x is large, the logarithm of E_x is of the same magnitude as these constants. Hence, these constants are significant and must be retained. Equation 16 can be rewritten as

$$E\{\theta^2\} = \frac{4\pi}{Q}\left(\frac{m\,a_0}{m_0 E_x}\right)^2 \ln(2.01\,E_x)\,, \tag{17}$$

by including the constants in the logarithmic term. With the use of Eq. 5, the final expression for the expected value of the square of the scattering angle is then

$$E\{\theta^2\} = \frac{12}{7E_x}\ln(2.01\,E_x)\,. \tag{18}$$

The use of this simple approximate analytical expression, which is very accurate, is highly preferable to doing numerical integrations of the original integral expression.

It is also of interest to calculate the expected value of the first power of the scattering angle for the collision of a high-energy proton with molecular hydrogen. The expected value of the scattering angle is defined as

$$E\{\theta\} = \frac{1}{Q}\int_0^{2\pi}\int_0^{\pi}\theta\, I(\theta,\phi)\sin(\theta)\,d\theta\,d\phi\,, \tag{19}$$

which, on following a procedure similar to that used above, yields

$$E\{\theta\} = \frac{39\pi}{56}\frac{1}{\sqrt{E_x}}\,. \tag{20}$$

This is also a simple and accurate analytical result.

From Eqs. 18 and 20 it is seen that, for this particular scattering event, the expected value of the square of the scattering angle and the expected value of the scattering angle are both dependent only on the energy of the collision. These expected values should not depend directly on the depth of penetration y, because the medium is assumed to be composed of the same molecules throughout. These expected values, however, have an indirect dependence on the penetration depth through the range-energy relationship of chapter 2, which relates the energy of the collision to the penetration depth of the particle.

The integrals of Eqs. 6 and 19 were numerically integrated for typical energies used in this work, by using Chebychev's integration technique. It was found that the numerical values obtained were less than 0.05 percent different from the approximate analytical results obtained above.

Reference

1. Cashwell, E. D. & C. J. Everett, "The Monte Carlo Method for Random Walk Problems", Vol. 1, Pergamon Press, 1959.

APPENDIX F

COMPUTER PROGRAM TO NUMERICALLY INTEGRATE EQUATION 3.36

```
C
C  THIS PROGRAM INTEGRATES EQUATION 3.36 BY THE RECTANGULAR METHOD
C
C  ENERGY LIMITS ARE OBTAINED FROM THE MONTE CARLO DATA FILE
C
      IMPLICIT REAL (M-N)
      COMMON A0,A1,A2,A3,E0
      REAL IN1(10000),IN2(10000),IN3(10000),IN4(10000),EN(10),XL(10)
C
      A0=.0512652
      A1=-.246743
      A2=0.690572
      A3=0.389733
C
      PI=3.141592654
C
      WRITE(5,*)' DATA FILE FOR FINDING E(R) VALUES?'
      READ(7,*) E0,BARL,D3,LMAX,CASE,B,B2
      READ(7,*) (XL(I),I=1,LMAX)
      READ(7,*) (EN(I),I=1,LMAX)
      N0=27./28./PI/5.292E-9**2./1836.11/13.58*E0/BARL
      WRITE(5,*) ' N0=',N0,' E0=',E0
C
      E0=E0/1.E6
C
      N=10000.
      DE=E0/N
      NN=INT((E0-EN(LMAX)/1.E6)/E0*N)+1
C
      DO 1 I=1,NN
      E=E0-(FLOAT(I)-.5)*DE
      IN1(I)=(A0/E**.5+A1+A2*E**.5+A3*E)*ALOG(2.01E6*1836.11*E/13.58)
     ./E**2.*DE
      IF(I.NE.1) IN1(I)=IN1(I)+IN1(I-1)
1     CONTINUE
      WRITE(5,*) ' FINISHED 1'
C
      DO 2 I=1,NN
      E=E0-(FLOAT(I)-.5)*DE
      CALL CALY(Y,FY,E,N0,B,B2)
      IF(FY.LT.0.) GOTO 3
      IN2(I)=(A0/E**.5+A1+A2*E**.5+A3*E)/FY*IN1(I)*DE
      IF(I.NE.1) IN2(I)=IN2(I)+IN2(I-1)
2     CONTINUE
3     WRITE(5,*) ' FINISHED 2  Y=',Y
C
      DO 4,I=1,NN
      E=E0-(FLOAT(I)-.5)*DE
```

```
      CALL CALY(Y,FY,E,NO,B,B2)
      IF(FY.LT.0.) GOTO 5
      IN3(I)=(AO/E**.5+A1+A2*E**.5+A3*E)/FY*IN2(I)*DE
      IF(I.NE.1) IN3(I)=IN3(I)+IN3(I-1)
4     CONTINUE
5     WRITE(5,*) ' FINISHED 3'
C
      DO 6,I=1,NN
      E=EO-(FLOAT(I)-.5)*DE
      CALL CALY(Y,FY,E,NO,B,B2)
      IF(FY.LT.0.) GOTO 7
      IN4(I)=(AO/E**.5+A1+A2*E**.5+A3*E)/FY**2.*IN1(I)*E*DE
      IF(I.NE.1) IN4(I)=IN4(I)+IN4(I-1)
6     CONTINUE
7     WRITE(5,*) ' FINISHED 4'
C
      C1=-(128./81.*PI*5.29177E-9**2*13.58**2/NO**2*1.E51)
      C2=12./7./1836.11*13.58/NO**2*1.E36
      WRITE(5,*) C1,C2
C
      DO 9 I=1,LMAX
      EN(I)=EN(I)/1.E6
      IE=INT((EO-EN(I))/EO*N)
      EI=(EO-EN(I))/EO*N
      ER2=-(C1*IN3(IE)+C2*IN4(IE))
      WRITE(6,8) EN(I),SQRT(ER2),ER2,IE
      WRITE(5,*) -C1*IN3(IE),-C2*IN4(IE)
8     FORMAT(3E20.10,I6)
9     CONTINUE
10    FORMAT(20X,E20.10)
      STOP
      END
C
C
      SUBROUTINE CALY(Y,FY,E,NO,B,B2)
C
C  THIS SUBROUTINE CALCULATES Y FOR A GIVEN ENERGY USING EQ. 3.34
C
      COMMON AO,A1,A2,A3,EO
      REAL NO
      IF(B.EQ.0.) GOTO 1
      IF(B2.NE.0.) GOTO 2
      Y=1./B*(SQRT(1.+2.E21/NO*B*(2.*AO*(EO**.5-E**.5)+A1*(EO-E)+
     .2./3.*A2*(EO**1.5-E**1.5)+A3/2.*(EO*EO-E*E)))-1.)
      FY=1.+B*Y
      RETURN
1     X=0.
      FY=1.
      RETURN
2     Y=1.E21/NO*(2.*AO*(EO**.5-E**.5)+A1*(EO-E)+
     .2./3.*A2*(EO**1.5-E**1.5)+A3/2.*(EO*EO-E*E))
      Y=1./B2*ALOG(B2*Y+EXP(-B*B2))+B
      FY=EXP(B2*(Y-B))
      RETURN
      END
```

APPENDIX G

COMPUTER PROGRAM TO INTEGRATE EQUATIONS 4.22 AND 4.23

```
C
C  THIS PROGRAM USES CHEBYCHEV INTEGRATION TO SOLVE THE INTEGRAND
C  DEFINED IN FUNCTION F2
C
C     SUBROUTINE  FF32(F,T,XL,XU)  DOES THE INTEGRATION
C
C          F-  THE INTEGRAND
C          T-  VALUE OF THE INTEGRAL
C          XL- LOWER LIMIT OF SEGMENT INTEGRATION
C          XU- UPPER   "   "     "         "
C
C  THE PROGRAM BREAKS THE INTERVAL (XMIN-XMAX) INTO N DIVISIONS
C
      IMPLICIT REAL (M-N)
      DIMENSION XX(153),YY(153),Y1(153),Y2(153)
      COMMON RR,RO,R1
C
      YY(152)=0.
      YY(153)=1.
      XX(152)=0.
      XX(153)=1.
      Y1(153)=1.
      Y1(152)=0.
      Y2(153)=1.
      Y2(152)=0.
C*******************************************
C DIAMETER OF THE ORIFICE
      READ(3,*) RORF
C*******************************************
C DIAMETER OF THE PROTON BEAM
      READ(3,*) RO
C*******************************************
      CALL PLOTS(1,0,0)
      CALL NEWPEN(2)
      CALL PLOT(1.,1.,-3)
      CALL PLOT(5.,0.,2)
      CALL PLOT(5.,7.,2)
      CALL PLOT(0.,7.,2)
      CALL PLOT(0.,0.,2)
      DO 1 I=1,4
      CALL PLOT(0.,I/5.*7.,3)
1     CALL PLOT(0.05,I/5.*7.,2)
      CALL PLOT(0.,0.,3)
      CALL NEWPEN(4)
      CALL PLOT(5.*RO/RORF,7.,2)
      CALL PLOT(5.*RO/RORF,0.,2)
      CALL PLOT(5.,0.,2)
      CALL NEWPEN(2)
```

```
C*******************************************
C  GET THE R* VALUE FOR P(R)
2     READ(3,*) RR
      IF(RR.LT.0.) GOTO 18
      RR=6./10.*RR
C*******************************************
      DO 3 J=1,151
3     XX(J)=(J-1.)/50*RO/RORF*5.
      DO 6 J=1,151
      R1=(J-1.)/50.*RO
      IF(R1.EQ.0.) GOTO 5
C
C
C*******************************************
C              LOWER LIMIT
C*******************************************
C
      XMIN=R1-RO
      IF(R1.LT.RO) XMIN=-XMIN
C
C*******************************************
C              UPPER LIMIT
C*******************************************
C
      XMAX=RO+R1
C
C*******************************************
C               DIVISIONS
C*******************************************
C
      N=10
C
C*******************************************
C          PERFORM INTEGRATION
C*******************************************
      T=0.
      DX=(XMAX-XMIN)/N
      DO 4 I=1,N
      XL=XMIN+DX*(FLOAT(I)-1.)
      XU=XMIN+DX*FLOAT(I)
      IF(XU.GT.XMAX) XU=XMAX
C
      CALL FF32(S1,XL,XU)
C
      YN=1.
      T=T+S1
4     CONTINUE
      TEST=ALOG(2.)*((RO-R1)/RR)**2.
      IF(R1.LT.RO.AND.TEST.LT.23.) T=T+1./2.*(1.-EXP(-ALOG(2.)*
     .((RO-R1)/RR)**2.))
      IF(R1.LT.RO.AND.TEST.GT.23.) T=T+1./2.
      IF(R1.LT.RO) T=T+1./3.141592654*ATAN(((RO-R1)/RR)**2.)
      YY(J)=T*7.*XX(J)*RORF/5./RO
      WRITE(4,*) XX(J)*RORF/5.,YY(J)/7.
      IJK=J
      IF(YY(J).LT.0.005) GOTO 7
```

```
      GOTO 6
5     TEST=ALOG(2.)*(RO/RR)**2
      IF(TEST.LT.23.) T=3./4.*(1-EXP(-ALOG(2.)*(RO/RR)**2.))
      IF(TEST.GT.23.) T=T+3./4.
      T=T+1./3.141592654*ATAN((RO/RR)**2.)
      YY(J)=T*7.*XX(J)*RORF/5./RO
      WRITE(4,*) XX(J)*RORF/5.,YY(J)/7.
      T=0.
6     CONTINUE
7     DO 4 I=IJK,151
4     YY(I)=0.
C     CALL CURVE(XX,YY,151,.05)
      CALL LINE(XX,YY,151,1,0,0)
      CALL PLOT(7.,0.,3)
      CALL PLOT(12.,0.,2)
      CALL PLOT(12.,7.,2)
      CALL PLOT(7.,7.,2)
      CALL PLOT(7.,0.,2)
      DO 8 I=1,4
      CALL PLOT(7.,I/5.*7.,3)
8     CALL PLOT(7.05,I/5.*7.,2)
      CALL PLOT(7.,7.,3)
      CALL NEWPEN(4)
      CALL PLOT(7.+5.*RO/RORF,7.,2)
      CALL PLOT(7.+5.*RO/RORF,0.,2)
      CALL PLOT(12.,0.,2)
      CALL NEWPEN(2)
      DO 9 I=2,151
9     Y1(I)=YY(I)/XX(I)/RORF*5.*RO
      Y1(1)=Y1(2)
      DO 10 I=1,151
10    XX(I)=XX(I)+7.
      CALL LINE(XX,Y1,151,1,0,0)
      CALL PLOT(14.,0.,3)
      CALL PLOT(19.,0.,2)
      CALL PLOT(19.,7.,2)
      CALL PLOT(14.,7.,2)
      CALL PLOT(14.,0.,2)
      DO 11 I=1,4
      CALL PLOT(14.,I/5.*7.,3)
11    CALL PLOT(14.05,I/5.*7.,2)
      CALL PLOT(14.,7.,3)
      DO 12 I=1,151
12    XX(I)=XX(I)+7.
      DO 13 I=1,51
13    Y2(I)=(XX(I)-14.)**2.
      DO 14 I=1,51
14    Y2(I)=Y2(I)/Y2(51)*7.
      DO 15 I=52,151
15    Y2(I)=7.
      CALL NEWPEN(4)
      CALL LINE(XX,Y2,151,1,0,0)
      CALL NEWPEN(2)
      Y2(1)=0.
      DO 16 I=2,151
      Y2(I)=YY(I)+Y2(I-1)
```

```
16    CONTINUE
      DO 17 I=1,151
17    Y2(I)=Y2(I)/Y2(151)*7.
      CALL LINE(XX,Y2,151,1,0,0)
      GOTO 2
18    CALL PLOT(0.,0.,999)
      STOP
      END
```

```
C
C*********************************************
C                INTEGRAND
C*********************************************
C
      REAL FUNCTION F1(R)
      COMMON RR,R0,R1
C
      F2=0.
      TEST=ALOG(2.)*(R/RR)**2.
      IF(TEST.LT.23.)  F2=ALOG(2.)*R/RR*EXP(-ALOG(2.)*(R/RR)**2.)
      F2=F2+2./3.141592654*R/RR/(1.+(R/RR)**4.)
      F1=1./3.141592654*ACOS((R*R+R1*R1-R0*R0)/(2.*R*R1))*F2
C
      RETURN
      END
```

```
C
C*********************************************
C          CHEBYCHEV INTEGRATION
C*********************************************
C
      SUBROUTINE FF32(T,XL,XU)
C
      X=XU-XL
      C=.136806908E-2*X
      T=.350930500E-2*(F1(XL+C)+F1(XU-C))
      C=.719424423E-2*X
      T=T+.813719737E-2*(F1(XL+C)+F1(XU-C))
      C=.176188722E-1*X
      T=T+.126960327E-1*(F1(XL+C)+F1(XU-C))
      C=.325469620E-1*X
      T=T+.171369315E-1*(F1(XL+C)+F1(XU-C))
      C=.518394221E-1*X
      T=T+.214179490E-1*(F1(XL+C)+F1(XU-C))
      C=.753161931E-1*X
      T=T+.254990296E-1*(F1(XL+C)+F1(XU-C))
      C=.102758102*X
      T=T+.293420467E-1*(F1(XL+C)+F1(XU-C))
      C=.133908941*X
      T=T+.329111114E-1*(F1(XL+C)+F1(XU-C))
      C=.168477867*X
      T=T+.361728971E-1*(F1(XL+C)+F1(XU-C))
      C=.206142121*X
      T=T+.390969479E-1*(F1(XL+C)+F1(XU-C))
      C=.246550046*X
      T=T+.416559621E-1*(F1(XL+C)+F1(XU-C))
      C=.289324362*X
      T=T+.438260465E-1*(F1(XL+C)+F1(XU-C))
      C=.334065699*X
      T=T+.455869393E-1*(F1(XL+C)+F1(XU-C))
      C=.380356319*X
      T=T+.469221995E-1*(F1(XL+C)+F1(XU-C))
      C=.427764019*X
      T=T+.478193600E-1*(F1(XL+C)+F1(XU-C))
      C=.475846167*X
      T=T+.482700443E-1*(F1(XL+C)+F1(XU-C))
      T=T*X
      RETURN
      END
```

UTIAS Report No. 278

Institute for Aerospace Studies, University of Toronto
4925 Dufferin Street, Downsview, Ontario, Canada, M3H 5T6

LATERAL DISPERSION OF A HIGH-ENERGY ION BEAM IN A SCATTERING MEDIUM

Crouch, T. W., Gottlieb, J. J.

1. Ion-beam dispersion 2. Ion-beam scattering
3. High-energy ion scattering 4. Monte Carlo simulation

The problem of the lateral dispersion of a beam of high-energy ions by molecular collisions as it passes through a variable density medium is solved by using both a Monte Carlo simulation and a new approximate analytical method. Numerous Monte Carlo computer runs are completed for high-energy ions (protons) moving in a varying density gas (molecular hydrogen). These runs include aphysical cases for which the energy of the ion is unattenuated with distance and physical cases for which the ion energy is decreased in accordance with experimental measurements of its range. Such numerical results show clearly that the beam-dispersion profiles at increasing ion-beam penetration depths are essentially self similar and that the profiles from different cases were also essentially similar. Based on the idea of similarity, an approximate analytical method is developed for quick and easy scaling of the beam-dispersion profiles within each case and from one case to another, in order to dispense with the time consuming and costly Monte Carlo simulations. This method for predicting the change in the probability distribution (root-mean-square value) of the dispersed-beam profile is successful, and the Monte Carlo results are reproduced well. It should be noted that this work is done mainly for a unidirectional point source of monoenergetic ions in the absence of any external magnetic and electric fields. However, the analysis to extend the results from a point source to a finite-sized beam of variable intensity, cross-sectional area, and ion energy is presented and some results are given.

Available copies of this report are limited. Return this card to UTIAS, if you require a copy.

UTIAS Report No. 278

Institute for Aerospace Studies, University of Toronto
4925 Dufferin Street, Downsview, Ontario, Canada, M3H 5T6

LATERAL DISPERSION OF A HIGH-ENERGY ION BEAM IN A SCATTERING MEDIUM

Crouch, T. W., Gottlieb, J. J.

1. Ion-beam dispersion 2. Ion-beam scattering
3. High-energy ion scattering 4. Monte Carlo simulation

The problem of the lateral dispersion of a beam of high-energy ions by molecular collisions as it passes through a variable density medium is solved by using both a Monte Carlo simulation and a new approximate analytical method. Numerous Monte Carlo computer runs are completed for high-energy ions (protons) moving in a varying density gas (molecular hydrogen). These runs include aphysical cases for which the energy of the ion is unattenuated with distance and physical cases for which the ion energy is decreased in accordance with experimental measurements of its range. Such numerical results show clearly that the beam-dispersion profiles at increasing ion-beam penetration depths are essentially self similar and that the profiles from different cases were also essentially similar. Based on the idea of similarity, an approximate analytical method is developed for quick and easy scaling of the beam-dispersion profiles within each case and from one case to another, in order to dispense with the time consuming and costly Monte Carlo simulations. This method for predicting the change in the probability distribution (root-mean-square value) of the dispersed-beam profile is successful, and the Monte Carlo results are reproduced well. It should be noted that this work is done mainly for a unidirectional point source of monoenergetic ions in the absence of any external magnetic and electric fields. However, the analysis to extend the results from a point source to a finite-sized beam of variable intensity, cross-sectional area, and ion energy is presented and some results are given.

Available copies of this report are limited. Return this card to UTIAS, if you require a copy.

UTIAS Report No. 278

Institute for Aerospace Studies, University of Toronto
4925 Dufferin Street, Downsview, Ontario, Canada, M3H 5T6

LATERAL DISPERSION OF A HIGH-ENERGY ION BEAM IN A SCATTERING MEDIUM

Crouch, T. W., Gottlieb, J. J.

1. Ion-beam dispersion 2. Ion-beam scattering
3. High-energy ion scattering 4. Monte Carlo simulation

The problem of the lateral dispersion of a beam of high-energy ions by molecular collisions as it passes through a variable density medium is solved by using both a Monte Carlo simulation and a new approximate analytical method. Numerous Monte Carlo computer runs are completed for high-energy ions (protons) moving in a varying density gas (molecular hydrogen). These runs include aphysical cases for which the energy of the ion is unattenuated with distance and physical cases for which the ion energy is decreased in accordance with experimental measurements of its range. Such numerical results show clearly that the beam-dispersion profiles at increasing ion-beam penetration depths are essentially self similar and that the profiles from different cases were also essentially similar. Based on the idea of similarity, an approximate analytical method is developed for quick and easy scaling of the beam-dispersion profiles within each case and from one case to another, in order to dispense with the time consuming and costly Monte Carlo simulations. This method for predicting the change in the probability distribution (root-mean-square value) of the dispersed-beam profile is successful, and the Monte Carlo results are reproduced well. It should be noted that this work is done mainly for a unidirectional point source of monoenergetic ions in the absence of any external magnetic and electric fields. However, the analysis to extend the results from a point source to a finite-sized beam of variable intensity, cross-sectional area, and ion energy is presented and some results are given.

Available copies of this report are limited. Return this card to UTIAS, if you require a copy.

UTIAS Report No. 278

Institute for Aerospace Studies, University of Toronto
4925 Dufferin Street, Downsview, Ontario, Canada, M3H 5T6

LATERAL DISPERSION OF A HIGH-ENERGY ION BEAM IN A SCATTERING MEDIUM

Crouch, T. W., Gottlieb, J. J.

1. Ion-beam dispersion 2. Ion-beam scattering
3. High-energy ion scattering 4. Monte Carlo simulation

The problem of the lateral dispersion of a beam of high-energy ions by molecular collisions as it passes through a variable density medium is solved by using both a Monte Carlo simulation and a new approximate analytical method. Numerous Monte Carlo computer runs are completed for high-energy ions (protons) moving in a varying density gas (molecular hydrogen). These runs include aphysical cases for which the energy of the ion is unattenuated with distance and physical cases for which the ion energy is decreased in accordance with experimental measurements of its range. Such numerical results show clearly that the beam-dispersion profiles at increasing ion-beam penetration depths are essentially self similar and that the profiles from different cases were also essentially similar. Based on the idea of similarity, an approximate analytical method is developed for quick and easy scaling of the beam-dispersion profiles within each case and from one case to another, in order to dispense with the time consuming and costly Monte Carlo simulations. This method for predicting the change in the probability distribution (root-mean-square value) of the dispersed-beam profile is successful, and the Monte Carlo results are reproduced well. It should be noted that this work is done mainly for a unidirectional point source of monoenergetic ions in the absence of any external magnetic and electric fields. However, the analysis to extend the results from a point source to a finite-sized beam of variable intensity, cross-sectional area, and ion energy is presented and some results are given.

Available copies of this report are limited. Return this card to UTIAS, if you require a copy.